37
10-10-80 RR

UCRL-52994

Late time optical spectra from the Ni^{56} model for Type I Supernovae

Timothy Stephen Axelrod
(Ph.D. Thesis)

MASTER

July 1980

UCRL-52994

Late time optical spectra from the Ni^{56} model for Type I Supernovae

Timothy Stephen Axelrod
(Ph.D. Thesis)

Manuscript date: July 1980

DISCLAIMER

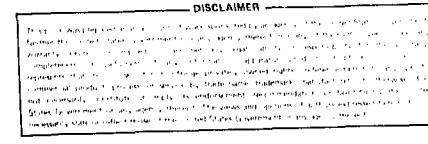

LAWRENCE LIVERMORE LABORATORY
University of California • Livermore, California • 94550

Available from: National Technical Information Service • U.S. Department of Commerce
5285 Port Royal Road • Springfield, VA 22161 • $15.00 per copy • (Microfiche $3.50)

UNIVERSITY OF CALIFORNIA

SANTA CRUZ

Late Time Optical Spectra From the Ni^{56} Model for Type I Supernovae

A Dissertation submitted in partial satisfaction of the requirements for the degree of

DOCTOR OF PHILOSOPHY

in

PHYSICS

by

Timothy Stephen Axelrod

July 1980

The dissertation of Timothy Stephen Axel is approved:

Joseph Ludwick

S E Woosley

Henry D Pasquier

George R. Blumenthal

ean of the Graduate Division

Late Time Optical Spectra From the Ni^{56} Model for Type I Supernovae

Timothy Stephen Axelrod

Abstract

The hypothesis that the optical luminosity of Type I supernovae results from the radioactive decay of Ni^{56} synthesized and ejected by the explosion has been investigated by numerical simulation of the optical spectrum resulting from a homologously expanding shell composed initially of pure Ni^{56}. This model, which neglects the effects of material external to the Ni^{56} core, is expected to provide a reasonable representation of the supernova at late times when the star is nearly transparent to optical photons. The numerical simulation determines the temperature, ionization state, and non-LTE level populations which result from energy deposition by the radioactive decay products of Ni^{56} and Co^{56}. The optical spectrum includes the effects of both allowed and forbidden lines.

The optical spectra resulting from the simulation are found to be sensitive to the mass and ejection velocity of the Ni^{56} shell. A range of these parameters has been found which results in good agreement with the observed spectra of SN1972e over a considerable range of time. In particular, evidence for the expected decaying abundance of Co^{56} has been found in the spectra of SN1972e. These results are used to assess the validity of the Ni^{56} model and set limits on the mass and explosion mechanism of the Type I progenitor. The possibilities for improvement of the numerical model are discussed and future atomic data requirements defined.

Table of Contents

I. Introduction

Type I supernovae (SNI), a class which contains approximately half of all observed supernovae, are currently quite poorly understood. The identity of the progenitors of SNI, the nature of their explosion, and the processes which result in the observed light curves are all highly uncertain. In contrast, Type II supernovae (SNII) are relatively well understood as resulting from the explosion of massive ($M \gtrsim 10\ M_\odot$) main sequence stars following gravitational core collapse. There are at least three characteristics of SNI that have made it difficult to find the proper place for them in the theory of stellar evolution.

Firstly, SNI are found in all types of galaxies, including ellipticals. Since star formation is generally assumed to be absent in elliptical galaxies, the occurrence of SNI seems to imply a presupernova lifetime of $\gtrsim 10^{10}$ yrs. For such a long lived star to explode requires either evolution in a binary system with special characteristics (Whelan and Iben 1973) or an unknown type of single star evolution. Recently, however, Oemler and Tinsley (1979) have argued that SNI have much shorter presupernova lifetimes and that their occurrence in ellipticals may be explained by star formation occurring at a rate which has escaped detection by a small margin. Better observations of elliptical galaxies may be able to settle this issue, which has long been a central one for the understanding of SNI.

The second important characteristic of SNI is the lack of hydrogen lines in the optical spectrum, as opposed to SNII which

have prominent hydrogen lines. Once again some special form of stellar evolution seems necessary to result in the lack of hydrogen in the presupernova object. There is no lack of possibilities, but at the same time, no compelling reason to choose one of them over the others. Explanations proposed for the lack of hydrogen include: explosion of HdC stars (Wheeler 1978); presupernova ejection of the hydrogen envelope by a stellar wind or a thermonuclear flash (Weaver, Axelrod, and Woosley 1980); and burning of accreted hydrogen to helium on the surface of a white dwarf (Taam 1980; Woosley, Weaver, and Taam 1980).

The third characteristic of SNI which has posed theoretical difficulties is the shape of the light curve (Fig. 1.1a). While it is possible to explain the light curve for times less than 30 days after maximum as the result of the diffusive release of energy deposited by a radiation dominated shock in an extended atmosphere (Lasher 1975), some additional source of energy is required to explain the exponential tail which follows the initial decline from peak luminosity. It is worth noting that the light curves for SNII (Fig. 1.1b) also exhibit an exponential tail, but it does not begin until about 150 days after maximum and contributes a much smaller fraction of the observed luminosity than is the case for SNI. The SNII light curve is on the whole well reproduced by a shock wave resulting from core collapse propagating through the mantle and atmosphere of a massive star (Weaver and Woosley 1980).

The nature of the energy source for the exponential tail of the SNI light curve has been the subject of much discussion. Recent proposals include the injection of energy from a central remnant (e.g., Bodenheimer and Ostriker 1974; Gordon 1975), and optical fluorescence from absorption of a pulse of ultraviolet photons in an extended atmosphere (Morrison and Sartori 1969). In many respects, however, the earliest explanation offered remains the most interesting - namely the suggestion by Borst (1950), and later by Burbidge et al (1956) that the late time light curve is powered by the radioactive decay of freshly synthesized material ejected in the explosion. Although Be^7 was proposed by Borst and Cf^{254} by Burbidge et al as the isotope responsible for the luminosity, it soon became clear that they were ruled out because the required amounts could not be synthesized and ejected without violating observed cosmic abundances by large factors. The rapid advancement of the theory of nucleosythesis soon resulted in a more consistent choice for the responsible isotope when Colgate and McKee (1969) proposed the beta decay chain $Ni^{56} \rightarrow Co^{56} \rightarrow Fe^{56}$. In the subsequent decade, as detailed numerical models of explosive nuceosynthesis were created (e.g., Arnett and Truran 1969; Bodansky, Clayton, and Fowler 1968; Woosley et al, 1973), it became clear that significant amounts of Ni^{56} should be synthesized in a wide variety of explosive events, making the investigation of its role in SNI luminosity more compelling.

In spite of this fact, a detailed investigation of the Ni^{56} model for SNI luminosity has been lacking. Previous investigations, beginning with Colgate and McKee (1969), and followed by Arnett (1979), and by Colgate, Petschek, and Kriese (1980), have largely been limited to modelling of light curves. The optical spectra of SNI have been discussed within the context of the Ni^{56} model by Meyerott (1978, 1979), but no complete calculation of synthetic spectra have been performed. The purpose of the present work is to test the Ni^{56} model for SNI luminosity by calculating self consistent synthetic spectra during the exponential tail phase of the light curve and comparing the synthetic spectra with observations of SN 1972e in NGC5253, currently the only SNI for which such a test is quantitatively possible. If detailed agreement can be achieved, one can hope not only to confirm the Ni^{56} model but to learn much about the progenitors of SNI.

In Section II an overview of the physics of stellar explosions is given and a model suitable for testing the Ni^{56} hypothesis defined. Section III discusses the atomic processes induced by the decay products of Ni^{56} and Co^{56}. The results of Section III are utilized in Section IV to determine the steady state temperature and ionization of the SNI. The validity of the steady state approximation is investigated and the implications of its breakdown at very late times determined. In Section V the formalism required to calculate the optical spectrum of the model SNI is developed. Particular attention is paid to the effects of optically thick allowed lines on

the spectrum. Results from the model are presented in Sections VI and VII and compared with observations of SN1972e, the light curve being discussed in Section VI and the optical spectrum in Section VII. It is shown that a range of model parameters exists which reproduces both the light curve and the optical spectra of SN1972e acceptably well. Evidence is presented for the expected decaying abundance of Co^{56} in the optical spectra. The effects of the simplified nature of the model and the uncertainties in the available atomic and astronomical data on these results are discussed in detail. The implications of the results are discussed in Section VIII and the prospects for further work outlined.

Figure Captions

Fig. 1.1 Composite B light curves for supernovae. Reproduced from Barbon, Ciatti, and Rosino (1973; 1979)

a) SNI

b) SNII

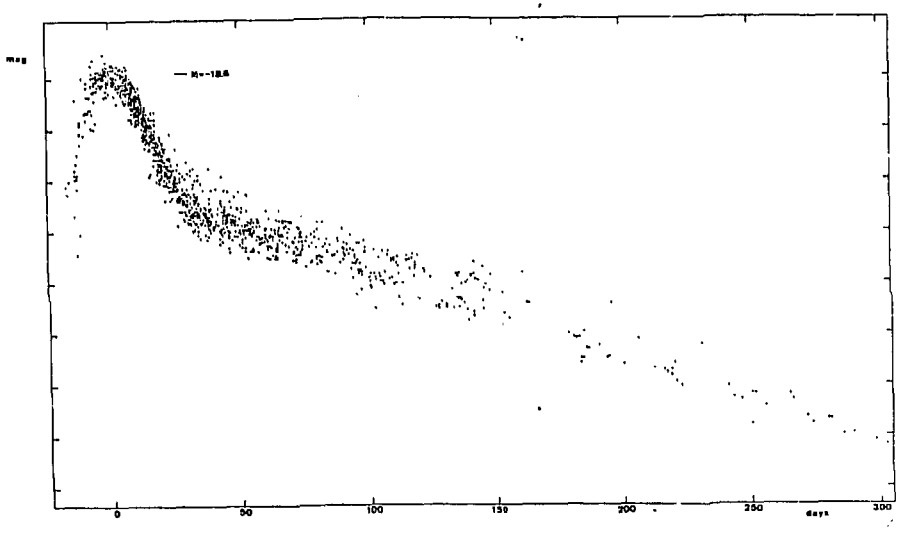

Fig. 1.1a

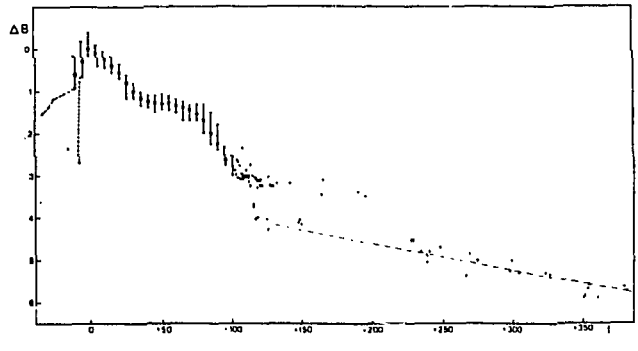

Fig. 1.1b

II. Numerical Modelling of the Nebular Phase of SNI

In view of the wide diversity of possible SNI progenitors it is useful to emphasize the phases of evolution which are common to all stellar explosions. For the purposes of the present discussion these may be identified as the nucleosynthetic phase, the photospheric phase, and the nebular phase.

The nucleosynthetic phase begins either with the gravitational collapse of the stellar core (Hoyle and Fowler 1960; Colgate and White 1966; Wilson (1971); Van Riper and Arnett 1978) or the initiation of a thermonuclear detonation or deflagration (cf Mazurek and Wheeler 1980; Sugimoto and Nomoto 1980; Woosley, Weaver, and Taam 1980). In either case a strong shock propagates through the star, with sufficiently high temperatures and densities being attained that substantial nuclear processing occurs. The amount of nuclear processing which a given mass element of the star undergoes is determined primarily by the peak temperature reached as the shock passes through it. For peak temperatures above roughly 4×10^9 °K a state of nuclear statistical equilibrium (NSE) is approached, in which all strong and electromagnetic processes are in detailed balance. In this state the nuclear abundances depend only on temperature, density, and the neutron-to-proton ratio (which is changed only by weak interactions), and are therefore nearly independent of the initial abundances. As detailed numerical calculations of explosive nucleosynthesis have shown (Woosley et al 1973; Hainebach et al 1974), after a stellar region driven into NSE cools below the "freezout

point" where significant nuclear reactions cease it will be composed principally of Ni^{56}, with a small mass fraction of He^4.(1) It is this fact which gives Ni^{56} importance for a broad range of stellar explosions.

The amount of Ni^{56} synthesized in a stellar explosion depends in a sensitive way on the density structure of the star and the mechanism of the explosion. We will not discuss this in any detail here. For our purposes we merely note that the ejected Ni^{56} mass, $\mathcal{M}$, falls in the general range $.05 \lesssim \mathcal{M} \lesssim 1.4$ $(M_\odot)$, with the lower range of masses ($\mathcal{M} \gtrsim 0.3$) resulting from core collapse models (Weaver and Woosley 1980), and the upper range ($\mathcal{M} \gtrsim 0.3$) resulting from detonations. The boundary between the Ni^{56} region and outer regions containing less completely processed material is typically quite sharp, leading to a natural distinction between the "core" and the "atmosphere", as we shall subsequently refer to these regions. Although the sharp boundary between the core and the atmosphere may subsequently be destroyed by processes such as convection and hydrodynamic instabilities we will ignore this complication.

The radiative output of the SNI begins when the shock, or its radiative precursor, reaches the surface of the star. After an

(1) This is true only for neutron-to-proton ratios close to the solar value. Highly neutronized material will have substantially different composition after freezout. However not much of this material can be ejected into the interstellar medium without violating the observed isotopic abundances to an unacceptable degree.

initial transient associated with shock breakout, during which X-rays or cosmic rays may be produced (cf Colgate 1974), the photospheric phase begins. During this phase of evolution the star remains optically thick over a wide wavelength range, and its radiative output may be approximated as blackbody emission from a photospheric surface. Nearly all observations and theoretical models of SNI radiative output have concentrated on this phase (e.g. Branch and Patchett 1973; Mustel and Chugai 1975). The observations, which are discussed in some detail in Section VI, indicate that the photosphere expands with a nearly constant velocity of $U_{ph} \approx 1 \times 10^9$ cm/sec and that the temperature is $T_{ph} \approx 1 \times 10^4$ °K near maximum light.

The role of Ni^{56} during the photospheric phase is at present unclear. Arnett (1979), Colgate et al (1980), and Chevalier (1980) have considered models in which the luminosity during the photospheric phase is generated entirely by Ni^{56} and its intermediate decay product, Co^{56}. These models are all initially compact, so that the internal energy from the passage of the shock during the nucleosynthetic phase is lost to adiabatic expansion before it can be radiated. Good fits to the SNI lightcurve are found for all of these models with Ni^{56} masses in the range $0.25 \lesssim \mathcal{M} \lesssim 1.0$, and total ejected masses, $\mathcal{M}_T$, in the range $0.5 \lesssim \mathcal{M}_T \lesssim 1.4$. On the other hand, an equally good fit to observations during the photospheric phase was obtained by Lasher (1975), who considered the effect of a point explosion at the center of an extended low density

atmosphere, with no Ni^{56} being present. The luminosity is produced entirely from the diffusive release of internal energy remaining from the shock, which suffers relatively small adiabatic losses due to the initially extended structure. The required atmosphere mass is $\mathcal{M}_T$ = 2.0 with an initial density of $\rho = 10^{-8}$ g cm^{-3} and an explosion energy of 10^{51} ergs. So far models which are intermediate between these two extremes, with significant luminosity coming both from Ni^{56} and from release of shock deposited internal energy, have not been considered.

The nebular phase begins when the expanding star becomes optically thin, so that a photosphere no longer exists. The time when this occurs is not known with any certainty. There is no sudden change in the optical luminosity or the optical spectra which marks the transition. It may, however, be estimated from the condition that

$$\kappa_c \rho R \approx 1 \tag{2.1}$$

where κ_c is the continuum opacity ($cm^2 g^{-1}$), ρ is the density (g cm^{-3}), and R the radius (cm). If we approximate the star as a uniform sphere expanding at velocity U_9 (10^9 cm sec^{-1}), this may be expressed as

$$t_N \approx 250 \frac{\sqrt{\kappa_c \mathcal{M}_T}}{U_9} \text{ days} \tag{2.2}$$

where t_N is the time when the nebular phase begins, as measured from the time of explosion. The value of κ_c is quite uncertain. It is probably on the order of 0.1 cm^2 g^{-1} (Chevalier 1980). Assuming that the observed photospheric velocity of $U_9 \approx 1$ is the characteristic expansion velocity, and that $\mathcal{M}_T \approx 1$, this results in

$$t_N \approx 80 \text{ days} \tag{2.3}$$

or roughly 60 days after maximum light.

During the nebular phase the uncertainty over how much of the luminosity is due to internal energy remaining from the shock is removed. It must all be due to radioactivity if the Ni^{56} explanation of late time SNI luminosity is correct. Additionally, in the absence of significant continuum opacity the spectrum will become increasingly nonthermal and may be expected to show the effects of its unusual energy source in a clear manner. The nebular phase evidently presents the best opportunity for a test of the Ni^{56} hypothesis through numerical modelling.

We expect that the most essential features of the nebular phase will be well represented by a model which ignores the presence of the atmosphere. As will be discussed in Section III, late in the nebular phase both core and atmosphere are highly transparent to the gamma rays resulting from the decay of Co^{56}, and only the positrons are capable of depositing their energy within the nebula. Due

to the existence of magnetic fields these positrons have no possibility of escaping from the core, and the atmosphere is therefore deprived of any significant energy source. The effect of the atmosphere should therefore be limited to interposing some absorption lines between the core and the observer. It is reasonable to hope that these absorption lines will be reasonably few in number so that the emission spectrum of the core will not be seriously distorted. As will be seen in Section VII, this in fact is correct.

We further simplify the model by taking the density of the core to be uniform. There is less justification for this, since real post-explosion density profiles may be quite non-uniform, and in fact this is the most serious limitation of the model. To at least partially compensate for the lack of a realistic density profile the form of the model core is taken to be a spherical shell with a thickness ratio h (see Figure 2.1). This allows the model density to be chosen equal to the mass-averaged density of a more realistic density profile, while maintaining the same mass and expansion velocity. Thus if the real density profile is $\rho(r)$ the mass-averaged density is

$$\bar{\rho} = \frac{1}{\mathcal{M}} \int_0^R \rho(r)\, 4\pi r^2 \rho(r) dr \qquad (2.4)$$

and h is chosen such that

$$\frac{1}{1 - (1-h)^3} = \frac{\bar{\rho}}{\rho_0} \tag{2.5}$$

where

$$\rho_0 = \frac{3\mathcal{M}}{4\pi R^3} \tag{2.6}$$

the density of a uniform sphere. The core is expanding homologously, since all pressure forces are negligible, so that

$$\vec{U}(\vec{r},t) = \frac{\vec{r}}{t} \tag{2.7}$$

The composition is assumed to be pure Ni^{56} at t = 0.

The model is thus completely specified by the mass $\mathcal{M}(M_\odot)$, the expansion velocity of the outer edge, U_9 (10^9 cm/sec), and the shell thickness ratio, h. The temperature and ionization state are not input parameters, but self-consistently determined within the model.

Figure Captions

Fig. 2.1 Assumed structure of the SNI nebula. The numerical calculations ignore the effect of the atmosphere.

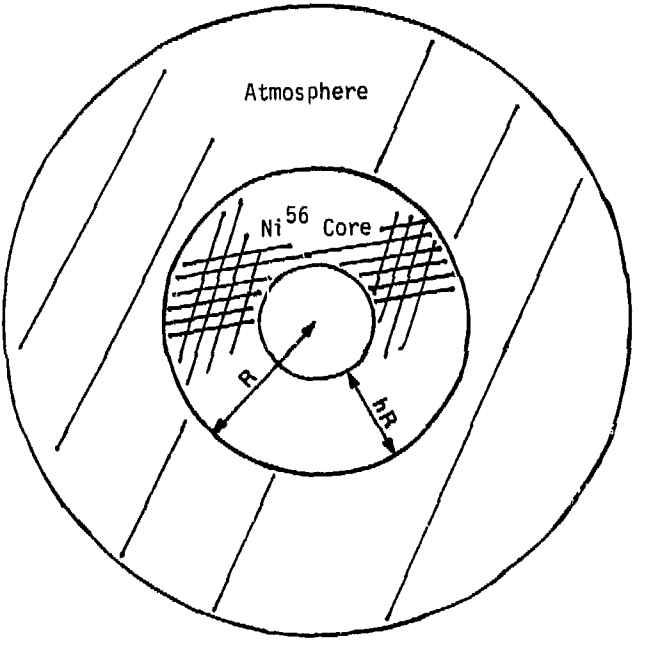

Fig. 2.1

III. Energy Deposition By Decay Products

A. The Deposition Rate

The two stage beta decay $Ni^{56} \rightarrow Co^{56} \rightarrow Fe^{56}$ results in time dependent fractional abundances given by

$$f_{Ni}(t) = e^{-t/\tau_{Ni}} \tag{3.1a}$$

$$f_{Co}(t) = \frac{e^{-t/\tau_{Co}} - e^{-t/\tau_{Ni}}}{1 - \tau_{Ni}/\tau_{Co}} \tag{3.1b}$$

$$f_{Fe}(t) = 1 - f_{Ni}(t) - f_{Co}(t) \tag{3.1c}$$

Here $\tau_{Ni} = 8.8$ d and $\tau_{Co} = 114$ d are the mean lives of Ni^{56} and Co^{56} (Lederer et al 1978) and it is assumed $f_{Ni}(0) = 1$. Since the nebular phase does not begin until $t \approx 80$ d, we may take $f_{Ni} = 0$ and consider the effects of Co^{56} decay only. As shown in Figure 3.1, the decay of Co^{56} generates a variety of monoenergetic gamma rays with typical energies of roughly 1 MeV, and a continuous spectrum of positrons with maximum energy of 1.46 MeV. The average gamma energy released per decay (including the annihilation gammas from the positrons) is

$$E_\gamma = 3.57 \text{ MeV} \tag{3.2}$$

The average energy of the positron spectrum, which has a highly linear Fermi-Kurie plot (Pettersson et al, 1964) is 0.66 MeV.

Accounting for the fact that the positron branch is taken by only 19% of the decays, the average positron energy per decay is

$$E_+ = .125 \text{ MeV} \tag{3.3}$$

The question of what fraction of the decay product energy deposits in the nebula has previously been considered by Arnett (1979) and Colgate et al (1980). Since thermal energies within the nebula ($KT \approx 1$ ev) and binding energies of outer shell electrons ($\lesssim 50$ev) are both negligibly small in comparison with the gamma energies, the interaction of the gammas with the nebula is nearly independent of the temperature and ionization state of the nebula. We are then free to use the crossections from neutral Fe, which are illustrated in Figure 3.2. The crossections for Co are not significantly different. Colgate et al (1980), utilizing a Monte Carlo transport code, determined that the energy deposition fraction for Co^{56} decay gammas emitted within a uniform sphere is well approximated as

$$D(\rho R) = G\left[1 + 2G(1 - G)(1. - .75G)\right]$$

where (3.4)

$$G = \frac{\rho R \kappa_\gamma}{1.6 + \rho R \kappa_\gamma}$$

The value determined for κ_γ, the effective gamma ray opacity, was .028 $cm^2 g^{-1}$. It is important to realize that κ_γ is dependent on the energy distribution of the Co^{56} gamma spectrum and also on the assumption that the source is a uniform sphere. Colgate et al state that the dependence of the deposition fraction on the source geometry is weak. To check this a calculation was performed for the density profile and source distribution resulting from a detonating white dwarf (Woosley, Weaver, and Taam 1980; Weaver, Axelrod, and Woosley 1980). The transport code used was a version of ANISN (Wilcox 1973) adapted by Axelrod (1978) for calculation of gamma line spectra from SNII. The results obtained were in good agreement with equation 3.4 if κ_γ was taken to be .033 $cm^2 g^{-1}$. The difference from the value chosen by Colgate et al is only about 20%, confirming the weak effect of the nonuniform density distribution. It is important to note, however, that even for a uniform sphere the energy deposition is quite nonuniform spatially, being strongly peaked at the center.

Taking R in equation 3.4 to be that of a uniform sphere of mass $\mathcal{M}(M_\odot)$ expanding with velocity U_9 (10^9 cm sec^{-1}) and κ_γ = .033 $cm^2 g^{-1}$, we find that at time t (days) after explosion

$$\rho R \kappa_\gamma = 2.1 \times 10^3 \frac{\mathcal{M}}{(U_9 t)^2} \qquad (3.5)$$

We note that if $\mathcal{M} \approx U_g \approx 1$ the gamma optical depth given above is only ≈ 0.3 at the beginning of the nebular phase (t = 80d). During the nebular phase we may then use a simpler form of equation 3.4:

$$D(\rho R) \approx 0.63\ \rho R \kappa_\gamma$$

$$\approx 1.3 \times 10^3 \frac{\mathcal{M}}{(U_g t)^2} \tag{3.6}$$

The transport problem for the positrons is less straightforward than that for gammas. In the absence of magnetic fields the positron deposition is approximately given by equation 3.4 with an appropriate value for κ. Colgate et al chose $\kappa_e = 10\ cm^2\ g^{-1}$ while I have found $\kappa_e \approx 7\ cm^2\ g^{-1}$ using SANDYL, a Monte Carlo electron transport code (Colbert 1974). The probability of in-flight annihilation is negligible (cf. Bussard et al 1979). The uncertainty arises from the fact that very weak magnetic fields have a strong effect on the deposition. The cyclotron radius for a 1 MeV positron is

$$r_c = \frac{4.7 \times 10^3}{B}\ cm \tag{3.7}$$

where B is the magnetic field (Gauss). On the other hand the nebular radius is

$$R = 8.64 \times 10^{13} U_9 t \tag{3.8}$$

so that $R \approx 10^{16}$ cm for $t \approx 100$ d. Even if B is as small as typical interstellar fields (10^{-6} - 10^{-5} gauss) we find that

$$\frac{r_c}{R} \lesssim 5 \times 10^{-7} \tag{3.9}$$

Colgate et al have assumed nonetheless that positron transport is uninhibited by magnetic fields, the explanation being that the field is "radially combed". Arnett (1979) has made the same assumption, although no explanation is proposed. The assumption made here, however, is that a disordered magnetic field of at least $B \approx 10^{-6}$ gauss will exist inside the expanding nebula. This appears reasonable for an expanding plasma generated by a violent explosion! In this case positrons are unable to escape from the nebula and in fact can not move a significant distance from their emission point.

The energy deposition rate in the nebula due to the decay of Co^{56} is then:

$$\mathbf{s}_{Co}(t) = \frac{f_{Co}(t)}{\tau_{Co}} (E_\gamma D(R) + E_+) \tag{3.10}$$

where the rate is expressed per atom. Substituting numerical values and assuming $t >> \tau_{Ni}$, we obtain

$$\mathcal{S}_{Co}(t) = 5.80 \times 10^{-13} e^{-t/114}(D(\rho R) + .035) \text{ (erg sec}^{-1}\text{atom}^{-1}\text{)} \quad (3.11)$$

We shall often approximate $\mathcal{S}_{Co}$ at late times by $\mathcal{S}^{+}_{Co}$, the value for positrons alone, which is

$$\mathcal{S}^{+}_{Co}(t) = 2.03 \times 10^{-14} e^{-t/114} \quad \text{(erg sec}^{-1}\text{atom}^{-1}\text{)} \quad (3.12)$$

To find the deposition rate for the entire nebula $\mathcal{S}_{Co}$ is simply multiplied by $\mathcal{N}$, the total number of atoms, which is

$$\mathcal{N} = 2.15 \times 10^{55} \mathcal{M} \quad (3.13)$$

It is of interest to calculate the time, T_{+}, when the gamma and positron depositions are equal. From equation 3.11 it is clear that this occurs when

$$D(\rho R) = .035 \quad (3.14)$$

or, utilizing the approximate form for D given by equation 3.6, at the time

$$T_+ = 192 \frac{\sqrt{\mathcal{M}}}{U_9} \text{ days} \qquad (3.15)$$

This is a significant event marker for the nebular phase. For $T < T_+$ the deposition is dominantly due to gammas, and is density dependent and spatially inhomogeneous. For $T > T_+$ the deposition is dominantly due to positrons, and is density independent and spatially homogeneous. The treatment of the numerical model is best suited to this latter situation, since the approximation of spatial homogeneity is utilized frequently.

B. Atomic Processes Induced By Decay Products

To calculate the optical luminosity of the SNI nebula it is not sufficient to know the deposition rate, $\mathbf{S}$. It is necessary to examine in detail the processes in the nebula which absorb the energy carried by the decay products. For the most part the distinction between iron and cobalt may be ignored when calculating the properties of the nebula, and a pure iron composition assumed. This approximation is justified due to the low cobalt abundance at the times of greatest interest and the fact that iron and cobalt differ only slightly in most atomic properties. The exception to this occurs for radiative transitions, where the distinction must be maintained to investigate the effects of cobalt on the spectrum.

As is clear from the crossections of Figure 3.2, Compton scattering is the dominant interaction for the gammas, and the average

energy transferred to the electron is a large fraction of the incident gamma energy. In effect, then, the power source for the nebula is a continuous spectrum of moderately relativistic electrons and positrons. Assuming for the moment that this source spectrum is known, the task is to determine the rates at which the source energy is dissipated in ionization and excitation of the ions present in the nebular plasma, and in heating of the free electron gas. This problem has previously been considered by Meyerott (1978). Let $S(E)dE$ be the primary electron source rate (sec^{-1} $atom^{-1}$) at energy E, in interval dE, and consider the rate $\gamma_{i\to j}$ (sec^{-1}) at which the primaries cause an atom in state i to undergo the transition $i \to j$. Here i and j are labels which contain all quantum numbers necessary to specify the states completely. In the case of an ionization process, for example, j must specify the momentum vector of the secondary electron as well as the final state of the atomic system. The initial state will be assumed to be the ground state configuration of an iron ion with charge between zero and roughly five.

If the slowing down of the primary electron occurs in a continuous manner (no large discrete changes in energy), as is expected at high energies, then

$$\gamma_{ij} = \frac{1}{N_i} \int_{E_0}^{\infty} dE\, N\, S(E) \int_{0}^{X(E)} N_i \sigma_{ij}(E(X))\, dX \qquad (3.16)$$

where $\sigma_{ij}(E)$ is the crossection of process $i \rightarrow j$ at electron energy E (cm^2), N_i is the number density of atoms in state i (cm^{-3}), N is the total atomic number density (cm^{-3}), and X(E) is the range (cm) of the primary electrons. $E_0 \approx 500$ ev is the energy below which the continuous slowing down approximation fails. Since primaries are born with energies $>> E_0$, γ_{ij} is insensitive to the choice of E_0. Using the fact that for continuous slowing down

$$dX = \frac{dE}{\left(\frac{dE}{dX}\right)} \tag{3.17}$$

and defining a loss function,

$$L(E) = -\frac{1}{N}\frac{dE}{dX} \tag{3.18}$$

equation (3.16) may be rewritten

$$\gamma_{ij} = \int_{E_0}^{\infty} dE\, S(E) \int_{E_0}^{E} dE' \, \frac{\sigma_{ij}(E')}{L(E')} \tag{3.19}$$

Now, in principle, knowing σ_{ij} for all i and j, the loss function could be calculated as

$$L(E) = \sum_i f_i \sum_j E_{ij}\, \sigma_{ij}(E) + L_{elec}(E) \qquad (3.20)$$

where $f_i = \frac{N_i}{N}$ is the fractional population of state i, E_{ij} is the energy of the transition $i \rightarrow j$, and $\sum_j$ includes integration over the continuous states. The loss function L(E) has been split into a part which results from atomic processes, which will be referred to as $L_{atom}(E)$, and a part which arises from the interaction of the primary with the free electron plasma $L_{elec}(E)$. Unfortunately, none of the σ_{ij} for iron are known with sufficient accuracy, and a different approach is necessary.

Since the energies at which primary electrons are born (0.5 - 1 MeV) are large compared with average excitation energies in the plasma ($I \approx 300$ ev), all significant energy deposition occurs while the ratio $E/I \gg 1$. This being so, it is appropriate to use the asymptotic Bethe form (Fano 1963, Inokuti 1971, Inokuti et al 1978) for the crossections σ_{ij} and the loss function L_{atom}, so that

$$L_{atom} = \frac{4\pi e^4}{mv^2} Z_b \left[\ln \frac{2mv^2}{I} + \ln \frac{1}{1-\beta^2} - \beta^2 \right] \qquad (3.21)$$

where $\beta = v/c$ for the primary, Z_b is the number of bound electrons per atom, and

$$\ell nI = \sum_j f_{ij} \ell n E_{ij} \tag{3.22}$$

where f_{ij} is the optical oscillator strength for the transition i→j and, as previously, $\sum_j$ involves an integration over continuum states (for which f_{ij} is more properly $\frac{df_{ij}}{dE}$). Similarily,

$$\sigma_{ij} = \frac{2\pi e^4}{mv^2} \frac{f_{ij}}{E_{ij}} \left[\ell n \frac{2mv^2}{C_{ij} E_{ij}} + \ell n \frac{1}{1 - \beta^2} - \beta^2 \right] \tag{3.23}$$

where C_{ij} are constants which depend on the details of the atomic wave functions. Forbidden excitations ($f_{ij} = 0$) play a negligible role when $E/I >> 1$, and have been neglected.

The loss function for the thermal electrons can be expressed in similar form as (Gould 1972, Inokuti et al 1978)

$$L_{elec} = \frac{4\pi e^4}{mv^2} \chi \left[\ell n \frac{2mv^2}{\hbar\omega_p} + \frac{1}{2} \ell n \frac{1}{1 - \beta^2} - \frac{1}{2} \beta^2 \right] \tag{3.24}$$

where $\chi = \frac{N_e}{N}$ and $\omega_p = 5.6 \times 10^4 \sqrt{N_e}$ sec^{-1} is the plasma frequency. The above expressions assume the incident particle is an electron. The expressions are different for positrons (Rohrlich and Carlson 1954), but the differences are small enough to be ignored in the present application.

The fact that σ_{ij}, L_{atom}, and L_{elec} possess nearly identical asymptotic high energy forms allows considerable simplification of equation (3.19). If we define

$$W_{ij}(E) = E \Big/ \left[\int_{E_0}^{E} dE' \, \frac{\sigma_{ij}(E')}{L(E')} \right] \tag{3.25}$$

then (3.19) may be rewritten as

$$\gamma_{ij} = \int_{E_0}^{\infty} dE \, \frac{ES(E)}{W_{ij}(E)} \tag{3.26}$$

We expect $W_{ij}(E)$ to be nearly independent of E at energies $E/I \gg 1$, so that picking a typical primary energy E_p and setting $W_{ij} = W_{ij}(E_p)$ equation (3.19) becomes

$$\gamma_{ij} = \frac{1}{W_{ij}} \int_{E_0}^{\infty} E \, S(E) \, dE \equiv \frac{\mathbf{S}}{W_{ij}} \tag{3.27}$$

The rate γ_{ij} thus depends on the primary source spectrum only through $\mathbf{S}$, the total rate at which energy is supplied by the primaries (erg $sec^{-1} atom^{-1}$), and not on the shape of the spectrum S(E). The quantity W_{ij} is the energy which must be expended by the primary for each $i \rightarrow j$ transition. To evaluate the expression

(3.21) for L_{atom}, the value of I, the "average excitation potential" is required. As shown by eqn. (3.22), I is a function of the oscillator strength distribution of the atomic system in question, and theoretical calculations of I are rare. Fortunately, I is well known experimentally (Anderson et al 1969) for neutral atoms. No data are available for ions, and the approximation is made that I is independent of ionization state, and given by the experimental value for FeI of I = 280 ev. This is reasonable, since the electronic configurations of FeI - III, the most abudant ions in the nebula, have ionization potentials $\ll$ I. Additionally, since L depends on I logarithmically, errors in I affect L only weakly. In this case, Z_b in equation (3.21) may be replaced by Z-x.

At this point considerable simplification has been achieved. To calculate a rate γ_{ij} by eqn (3.27), it is now necessary to know only the total rate of energy deposition **S**, and the crossection σ_{ij} for that rate. There is still the difficulty that the quantities C_{ij} needed to evaluate (3.23) for σ_{ij} are not known, and are difficult to calculate for a complex atom such as iron. Fortunately, for the SNI nebula, the only rates which need to be explicitly known are the total ionization rates

$$\gamma_i = \sum_{j \in c} \gamma_{ij} \qquad (3.28)$$

where the "sum" extends over all final states of the secondary electron. These rates are still given by equation (3.27) except that W_{ij} must be replaced by

$$W_i = E_p \Big/ \left[\int_{E_0}^{E_p} dE' \, \frac{\sigma_i(E')}{L(E')} \right] \tag{3.29}$$

where $\sigma_i(E)$ is the total ionization crossection, given by

$$\sigma_i = \sum_{j \epsilon c} \sigma_{ij} \tag{3.30}$$

These crossections are much better known than the differential crossections σ_{ij}, with both calculations for neutral iron (Jacobs et al 1979; McGuire 1977) and a variety of semi emperical forms (e.g. Lotz 1967; Drawin 1961) being available. W_i is now the familiar "work per ion pair" which has been investigated experimentally and theoretically since the 1930's (e.g. Platzman 1961), although mostly under quite different conditions than prevail in the SNI nebula. At high primary energies, W is found to be energy independent to high accuracy, as we expected.

Why is this simplification possible? Consider the fate of the secondary electrons resulting from ionization by the primaries. The

energy distribution of secondary electrons resulting from electron ionization have been measured by Opal et al (1971, 1972) for a number of gases. They found that $\sigma(E_p,E_s)$, the crossection for producing a secondary with energy E_s from a primary of energy E_p, is well approximated by

$$\sigma(E_p,E_s) \approx \frac{\sigma_i(E_p)}{\bar{E}\tan^{-1}\left[(E_p - P)/2\bar{E}\right]} \frac{1}{1 + (E_s/\bar{E})^2} \qquad (3.31)$$

where P is the ionization potential, $\sigma_i(E_p)$ is the total ionization crossection, and $\bar{E}$ is a characteristic secondary energy, found experimentally to be $0.5P \lesssim \bar{E} \lesssim P$, and a weak function of E_p. The expression is valid for $E_s < (E_p - P)/2$, the maximum secondary energy. To determine the effects of this spectrum of secondary electrons, it is in principle necessary to perform a calculation similar to that for the primary electrons. The expressions derived for the primaries cannot be applied to the secondaries however, since two assumptions made in the derivation are violated at the lower energies of the secondaries:

(a) The continuous slowing down approximation is no longer valid, since a secondary electron is likely to lose a large fraction of its energy if it has an ionizing collision.

(b) The Born approximation used for $\sigma_{i\to j}$, L_{atom} and L_{elec} is no longer valid, particularly for L_{atom}.

There are, however, approximations appropriate to the secondaries which allow the problem to be dealt with simply. Let us first compare the values of L_{atom} and L_{elec} for a primary energy of 500 ev, roughly the lowest energy for which the continuous slowing down theory and the Born expression both remain valid. From equations (3.21) and (3.24) we obtain

$$\frac{L_{elec}}{L_{atom}} = \frac{\chi}{Z - \chi} \frac{\ell n\left(\frac{4E}{\hbar\omega p}\right)}{\ell n\left(\frac{4E}{I}\right)} \tag{3.32}$$

At $t \approx 200d$, when $N_e \approx 10^6$ cm^{-3} and $\chi \approx 2$ (cf Section VII) $\hbar\omega_p \approx 4 \times 10^{-8}$ ev, and

$$\frac{L_{elec}}{L_{atom}} \approx 1 \quad \text{at} \quad E = 500 \text{ ev} \quad . \tag{3.33}$$

At lower electron energies, no accurate values for L_{atom} exist for Fe. It is clear, however, that the ratio L_{elec}/L_{atom} will increase rapidly as the electron energy is lowered toward the threshold energies of the atomic processes contributing to L_{atom}. The probability, Φ_1, that a secondary electron produces a further ionization is thus quite small, the most probable fate being to give up its energy in a continuous fashion ($E >> \hbar\omega_p$) to the thermal electrons until it reaches the edge of the "thermal sea" at $E \approx 4$ KT $\approx$ 2-4ev and is absorbed. A small number of secondaries will undergo

an ionizing collision during the slowing down process, giving up a major fraction of their energy. When $\phi_1 << 1$, so that $L \approx L_{elec}$

$$\phi_1 \approx \int_{P_1}^{E_0} dE_s \frac{\sigma(E_p,E_s)}{\sigma_i(E_p)} \left[1-e^{-\int_{P_1}^{E_s} dE'_s \frac{\sigma_i(E'_s)}{L_{elec}(E'_s)} \frac{N}{N_e}}\right] \tag{3.34}$$

where P_1 is the ionization potential. The integral extends only to E_0, since above E_0 the secondaries may be considered to be primaries in the continuous slowing down regime. As such they effectively cause a perturbation in the primary source spectrum S(E) without affecting the total primary energy source **S**. The ionization due to them has already been included in γ_i.

The energy of most secondaries is such that $v/c \leq \alpha$, where $\alpha = 1/137$ is the fine structure constant, an awkward region for the calculation of L_{elec}, where neither the Born nor the classical approximations are valid (Gould 1972). These two expressions are not greatly different, however, and a sufficiently accurate calculation of ϕ_1 is obtained by using the classical value of L_{elec}

$$L_{elec}(V) = \frac{4\pi e^4}{mv^2} \ln\left[\frac{mv^3}{2^{\frac{1}{2}}\pi e^2 \omega_p}\right] \tag{3.35}$$

or,

$$L_{elec}(E) = 1.95 \times 10^{-13} \frac{\ell n(3.2 \times 10^4 E)}{E} \text{ ev cm}^2 \qquad (3.36)$$

with E in ev. With Opal's (1972) expression for (E_p, E_s) (eqn. 3.31), Equation (3.34) becomes

$$O_1 \neq \int_{P_1}^{E_0} dE_s \frac{2}{\pi \bar{E}} \frac{1}{1 + (E_s/\bar{E})^2} \left[1 - e^{-\int_{P_1}^{E_s} dE'_s \frac{\sigma_i(E'_s)\, E'_s}{1.95 \times 10^{-13} \chi \ell n(3.2 \times 10^4 E'_s)}} \right] \qquad (3.37)$$

This expression has been evaluated using McGuire's (1977) calculation of σ_i for FeI. For $\chi = 2$ it is found that $\phi_1 \lesssim .05$, and is only weakly sensitive to variations in E and E_0 within the expected range. This result is in agreement with calculations of ϕ_1 for partially ionized hydrogen (Bergeron and Collin - Souffrin 1973) and helium (Meyerott 1978) for comparable values of χ.

The fact that ϕ_1 is so small implies that ϕ, the total expected ionizations by all generations of secondaries, which is roughly $O_1(1+O_1(1+....))$ is $\approx \phi_1$ and can be set to zero without causing significant error. In this approximation the total ionization rate is that due to primaries, given by equations 3.27 and 3.29.

To evaluate these expressions the semi-empirical form of Lotz (1967) is used for the total ionization crossection σ_i. At

energies large compared to the outer shell binding energies, and corrected for relativistic effects (e.g. Mott and Massey 1965), it takes the form

$$\sigma_i = \frac{2A}{\beta^2 mc^2} \sum_{j=1}^{N} \frac{q_j}{P_j} \left[\ell n \left(\frac{\beta^2 mc^2}{2P_j} \right) - \log (1 - \beta^2) - \beta^2 \right] \qquad (3.38)$$

Here the sum is over the subshells of the atom, each of which has q_j electrons with binding energy P_j(ev). The binding energies are taken from Lotz (1968). The sum is restricted to shells for which $\frac{1}{2}\beta^2 mc^2 > P_j$, where $\beta = v/c$. The constant A has been determined by normalizing to the average of the values given by Jacobs et al (1979) and McGuire (1977) at 10^4ev (1.1×10^{-17} cm^2 and 8.5×10^{-18} cm^2 respectively). This results in

$$A \approx 1.33 \times 10^{-14} \text{ (ev)}^2 \text{ cm}^2 \qquad (3.39)$$

We must now consider the effects of transitions to discrete states. From the expression 3.23 for the crossection we see that

$$\sigma_{ij} \propto \frac{f_{ij}}{E_{ij}} \qquad (3.40)$$

so that the contribution to the loss function from a transition is roughly

$$L_{ij} \approx E_{ij}\, \eta_{ij} \propto f_{ij} \tag{3.41}$$

In this approximation (the "optical" approximation (e.g. Seaton 1962)), the importance of a transition, discrete or continuous, in absorbing energy from the primaries is directly proportional to the oscillator strength of the transition. The oscillator strength distribution of Fe II (Phillips 1979; Rozsnyai 1980) is compared in Table 1 with that of HI and HeI. Iron differs qualitatively from hydrogen and helium in having a significant fraction of its oscillator strength in transitions to autoionizing states. These transitions are the origin of the large number of strong resonances which are observed in the iron photoionization crossection (J. E. Hansen et al 1977, Kelly and Ron 1972). Since fluorescence yields for iron are negligible for the L and M shells, these states decay by emitting electrons at discrete energies $\lesssim$ 50 ev. As previously discussed, electrons in this energy range deposit their energy in the thermal electron gas without interacting again with atoms. Table 1 shows, then, that while about 20% of the primary energy excites radiative states for helium, this fraction is about 4% for FeII. All remaining energy is expended in raising the ionization potential of the plasma and in heating the electron gas. In the numerical

calculations described in succeeding sections, the radiative fraction is assumed to be zero. This is doubly justified, since, as will be shown in section IV, the most likely fate for the UV photons emitted by radiative decay is to be absorbed in a photoionization process elsewhere in the plasma.

The results of this section may be summarized in the following expressions for S_{ion}, the rate at which energy flows into increasing ionization potential, and S_{elec}, the rate at which the thermal electrons are heated. Defining γ_i to be the total ionization rate of Fe^{+i} while P_i and W_i are the ionization potential and work per ion pair respectively, we have

$$S_{ion} = \sum_i f_i \gamma_i P_i \tag{3.42}$$

By using equation 3.27 we obtain

$$S_{ion} = S \sum_i f_i \frac{P_i}{W_i} \tag{3.43}$$

while

$$S_{elec} = S - S_{ion}$$

$$= S \sum_i f_i \left(1 - \frac{P_i}{W_i}\right) \tag{3.44}$$

The heating efficiency, η, is defined as

$$\eta = \frac{\mathcal{S}_{elec}}{\mathcal{S}} = \sum_i f_i \left(1 - \frac{P_i}{W_i}\right) \tag{3.45}$$

Numerical evaluation of expression 3.29 for SNI nebular conditions shows that

$$\frac{W_i}{P_i} \approx 30 \tag{3.46}$$

with less than a 10% difference for FeI - VI. This results in

$$\eta \approx 0.97 \tag{3.47}$$

so that the heating efficiency is very close to unity. Meyerott (1978, 1979) reached a similar conclusion. It is interesting to note that when the work per ion pair, W, is measured in gases it is found that $W/P \approx 2$ (Fano 1963). A much higher value occurs for the SNI nebula because the secondary electrons are inhibited from causing further ionizations by the presence of the free electron gas.

TABLE 1

Oscillator Strength Distributions

	FeII	HeI	HI
radiative	1.04	.42	.56
autoionizing	1.88	≈ 0	0
continuum	22.1	1.58	.44

Figure Captions

Fig. 3.1 The decay scheme of the $Ni^{56} \rightarrow Co^{56} \rightarrow Fe^{56}$ chain. From Lederer et al (1967). Revised data from Lederer et al (1978) have been incorporated in the figure.

Fig. 3.2 Photon crossections (a) and energy deposition (b) for Fe^{56}. From Plechaty et al (1978).

Fig. 3.3 Energy flow in the SNI nebula. The relative intensities of photons escaping in the ultraviolet and visible - infrared bands are shown in terms of the heating efficiency, η. The processes of recombination, absorption of UV radiation, and collisional excitation by thermal electrons are discussed in IV.

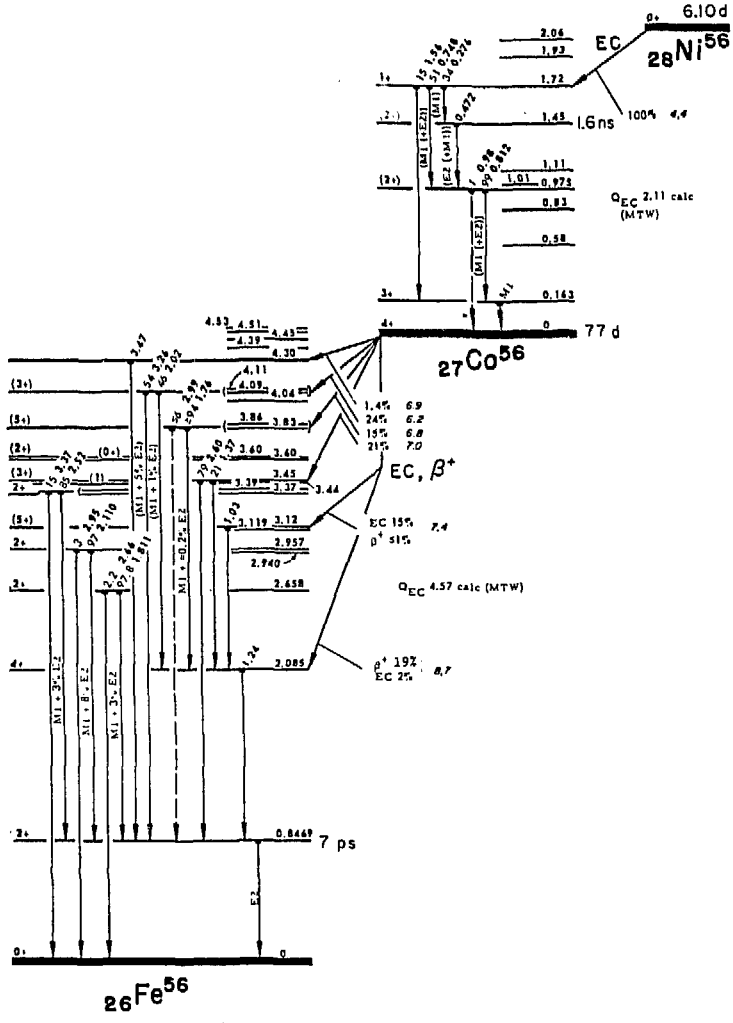
6.10d
EC
28Ni56
1.6ns
100%
77 d
27Co56
EC, β+
EC 15%
β+ 51%
β+ 19%
EC 2%
7 ps
26Fe56

Fig. 3.1

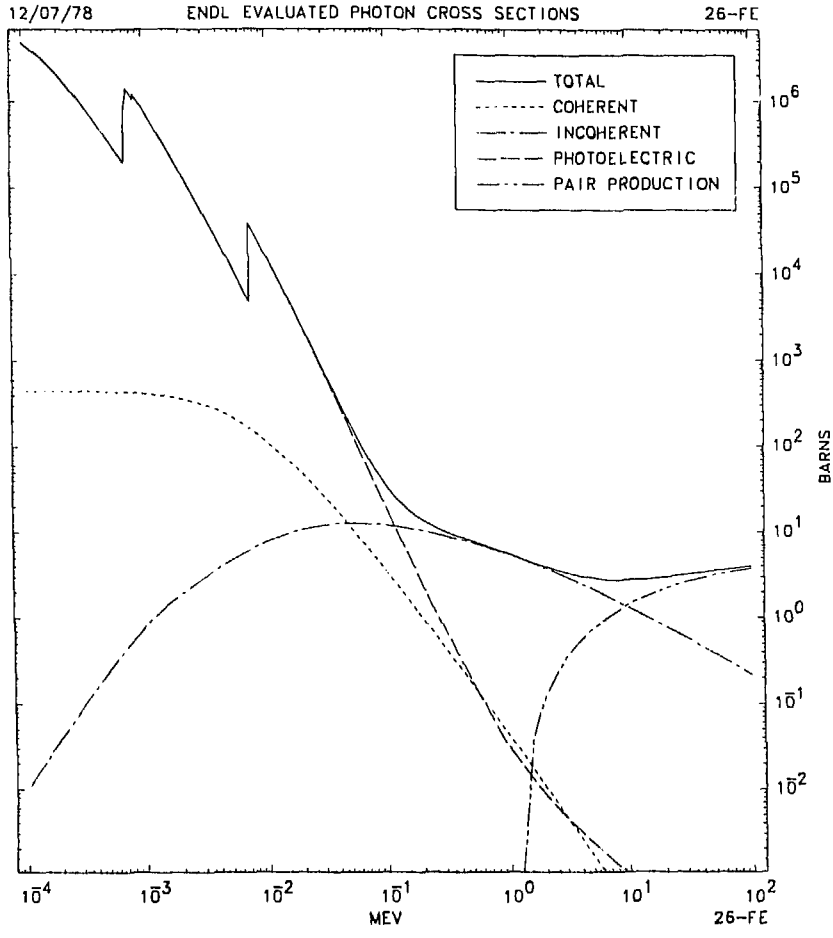
12/07/78
ENDL EVALUATED PHOTON CROSS SECTIONS
26-FE
TOTAL
COHERENT
INCOHERENT
PHOTOELECTRIC
PAIR PRODUCTION
BARNS
MEV
26-FE

Fig. 3.2a

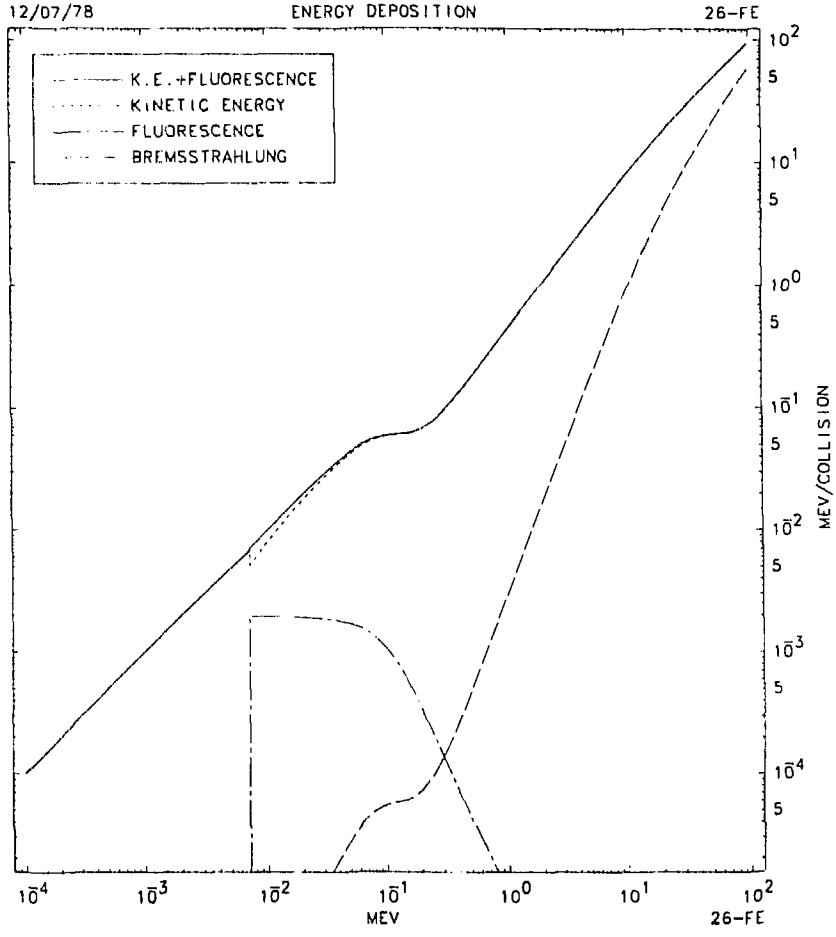
12/07/78
ENERGY DEPOSITION
26-FE
K.E.+FLUORESCENCE
KINETIC ENERGY
FLUORESCENCE
BREMSSTRAHLUNG
MEV/COLLISION
MEV
26-FE

Fig. 3.2b

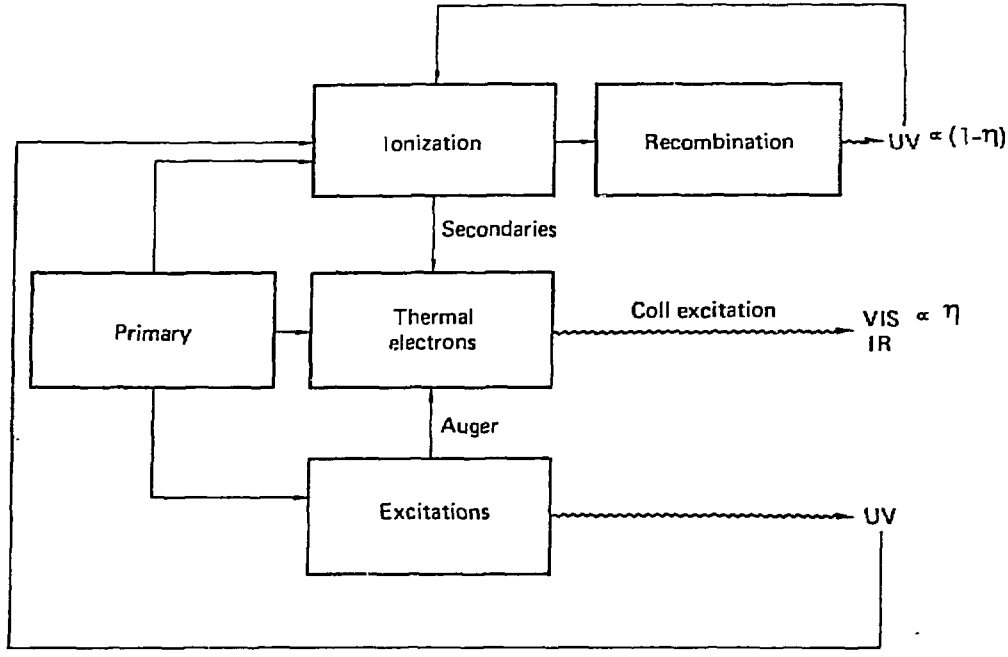
Ionization
Recombination
UV ∝ (1-η)
Secondaries
Primary
Thermal electrons
Coll excitation
VIS IR ∝ η
Auger
Excitations
UV

Fig. 3.3

IV. The Ionization and Thermal Balances in Steady State

A. The Ionization Balance

In the presence of the ionizing and heating sources due to primaries described in III, we expect that the nebula will come to a steady state, in which ionization is balanced by recombination, and heating by radiative cooling. In this section the ionization state and temperature of the nebula will be determined for steady state conditions, utilizing the results of Section III. Before proceeding, it is necessary to inquire into the nature and validity of the steady state approximation for the SNI nebula. There are three characteristic timescales which affect the dynamics of the ionization state of the nebula:

(1) The decay time of the energy source rate, $\tau_S \equiv |S/\dot{S}|$.

(2) The time for the density to decrease by a factor of $\approx e$, $\tau_N = |N/\dot{N}|$.

(3) The lifetime of an ion in the presence of ionizing electrons, $\tau_i = \frac{1}{\gamma_i}$ (eqn. 3.27).

The first two of these times, τ_S and τ_N are the characteristic timescales for the principal processes which cause the ionization balance to change with time, while τ_i is the measure of how fast the balance is able to shift in response. We expect that the steady state approximation will be valid for the ionization balance when τ_i is much smaller than both τ_S and τ_N.

The decay time of the energy deposition rate, τ_S, is itself determined by two more fundamental timescales: τ_{Co}, the decay

time of Co^{56}; and τ_{es}, the slowing down time for a typical primary electron. This latter time may be estimated as follows:

$$\tau_{es} = \int_0^{X(E_p)} \frac{dx}{V(x)} \approx \int_{E_0}^{E_p} \frac{dE}{NL(E)V(E)} \tag{4.1}$$

An error of less than a factor of two is made by taking the nonrelativistic form of equation 3.21 for L(E) and setting $\chi = 0$. In this case we obtain

$$\tau_{es} \approx \frac{\sqrt{2m}}{4\pi e^4 NZ} \int_{E_0}^{E_p} \frac{E^{\frac{1}{2}}dE}{\ell n(E/I)} \approx \frac{8.6 \times 10^4}{Z\ell n(E_p/I)} \frac{E_p^{3/2}}{N} \text{ sec} \tag{4.2}$$

where E_p is in ev. For $E_p = 5 \times 10^5$ ev, and $I = 280$ ev, we find that at 200 days, when $N \approx 10^6$ cm^{-3}

$$\tau_{es} \approx 1.6 \times 10^5 \text{ sec} = 1.9 \text{ d}$$

The fact that $\tau_{es} << \tau_{Co}$ implies that the primaries "instantaneously" deposit the energy released by Co^{56} decay, so that $S = S_{Co}$, and $\tau_S = \tau_{Co}$. This was implicitly assumed to be the case in III.

The time scale for density change, τ_N, is set by the assumed homologous spherical expansion, for which $N \propto 1/t^3$ and $\tau_N = t/3 \approx 65d$. Radiative recombination rates depend linearly on N for $X \approx$ constant, so that τ_N is a characteristic time for the ionization balance to shift significantly due to expansion.

The nebular ionization state is able to respond to changes in N and $\mathbf{S}$ on a timescale τ_i, which is the ionization lifetime for a typical plasma ion. We note that in steady state, where ionization is balanced by recombination, τ_i is also a measure of recombination lifetime. From equation 3.27 we have that

$$\tau_i = 1/\gamma_i = \frac{W_i}{\mathbf{S}} \tag{4.3}$$

For an estimate of τ_i, it is sufficient to set $W_i \approx 30\ P_i$, where P_i is the ionization potential (cf. equation 3.46). We may take $\mathbf{S}$ to be that due to the Co^{56} positrons (equation 3.12), so that, using ev as the energy unit

$$\tau_i \approx \frac{30P_i}{1.3\times10^{-2}e^{-t/114d}}\ \text{sec} \approx 3.9 \times 10^5\ \text{sec} \approx 4.5\ \text{d} \tag{4.4}$$

where the second equality results from assuming that FeIII (I = 30 ev) is the typical ion, and that t = 200 d.

Clearly at t = 200 d, the conditions $\tau_i << \tau_S$ and $\tau_i << \tau_N$ are satisfied , so that the ionization state is well approximated by the steady state solution. At sufficiently late times, τ_i, which grows as $e^{(t/\tau_{Co})}$, becomes comparable with τ_{Co}, and the steady state approximation is no longer valid. For the parameters assumed, $\tau_i \approx \tau_{Co}$ when t ≈ 600 d. It is important to note that the condition $\tau_{es} << \tau_{Co}$, which permitted the primary deposition to be treated as instantaneous, fails at about the same time, and the consequences of this will be briefly considered. We see from equation 4.2 that $\tau_{es} \propto \frac{1}{N} \propto t^3$, so that for the assumed parameters,

$$\tau_{es} \approx 1.9 \left(\frac{t}{200}\right)^3 \quad d \tag{4.5}$$

and $\tau_{es} \approx \tau_{CO}$ when t ≈ 800 d. When $\tau_{es} \approx \tau_{CO}$, the primary electron spectrum shows the effect of primaries that were emitted at earlier times when the source rate S_{CO} was significantly different. Additionally, $\tau_{es} \approx \tau_N$ when t ≈ 1200 d, so that a primary electron slows down in a plasma that changes its density significantly during the primary lifetime. These effects all result in a departure of S from S_{Co}, but do not alter the conclusions of III with regard to the deposition pathways, since these depend only on the high energy behavior of atomic crossections.

These results may be summarized in the conclusion that the SNI nebula remains in approximate steady state ionization balance with

$\mathbf{S} \approx \mathbf{S}_{Co}$ until $t \approx 600$ d for the nebular parameters we have used. At later times $\mathbf{S}$ may depart significantly from $\mathbf{S}_{Co}$, and the ionization state be far from the steady state solution. With these restrictions in mind we proceed to formulate the equation of ionization balance in steady state, assuming for the moment that the temperature T is known.

Let $\alpha_i(T)$ be the rate coefficient for the radiative recombination process $Fe^{+i} + e^- \Rightarrow Fe^{i-1} + h\nu$. Then we expect the ionization balance to take the form

$$\dot{n}_i = -\gamma_i n_i + \alpha_{i+1}(T)\, n_e n_{i+1} + \gamma_{i-1} n_{i-1} - \alpha_i(T)\, n_e n_i = 0 \qquad (4.6)$$

for all ions $0 \le i \le Z$, where n_i is the density of Fe^{+i}, and n_e is the electron density, given by

$$n_e = \sum_{i=0}^{Z} i n_i \qquad (4.7)$$

The quantities n_{-1}, n_{z+1}, α_0, and γ_{z+1}, which appear formally in equations 4.6 are without physical meaning and are defined to be zero.

$$n_{-1} = n_{z+1} = \alpha_0 = \gamma_{z+1} = 0 \qquad (4.8a)$$

the n_i must satisfy the additional constraint that

$$\sum_{i=0}^{Z} n_i = N \tag{4.8b}$$

Under the constraint (4.8a) the set of equations (4.4) obeys the conservation law

$$\sum_{i=0}^{Z} \dot{n}_i \equiv 0 \tag{4.9}$$

so that they are linearly dependent. The most convenient way of removing this linear dependence is to form a new set of equations from partial sums of (4.6), so that we obtain

$$\frac{1}{N} \sum_{j=0}^{i} \dot{n}_j = -\gamma_i f_i + \alpha_{i+1}(T)\, n_e f_{i+1} = 0 \tag{4.10}$$

for $0 \le i \le z-1$, and from equation (4.8b)

$$\sum_{i=0}^{Z} f_i = 1 \tag{4.11}$$

where, as before, $f_i = n_i/N$. We note that the set (4.10) expresses a form of detailed balance, in which ionization by primaries is balanced by radiative recombination for each ion.

The ion fractions f_i depend on the state of the nebula only through the parameters.

$$z_i = \frac{\gamma_i}{\alpha_{i+1}(T)n_e} \tag{4.12}$$

as is evident from 4.10,(1) and these may be rewritten using equation 3.27, as

---

(1) The fact that $f_{i+1} = z_i f_i$ for $i = 0,\ldots,z-1$ combined with equation 4.9 allows the f_i and χ to be expressed in terms of the z_i as

$$f_i = \frac{\prod_{j=0}^{i-1} z_j}{1 + \sum_{i=1}^{z} \prod_{j=0}^{i-1} z_j}$$

$$\chi = \sum_{i=0}^{Z} i\, f_i$$

$$z_i = \left(\frac{1}{w_i \alpha_{i+1}(T_e)}\right)\left(\frac{s_{CO}}{N_e}\right) \propto \left(\frac{t^3 e^{-t/\tau_{CO}}}{\chi}\right) \qquad (4.13)$$

The strongest time dependence of the z_i is contained in the term s_{Co}/N_e, which is the same for all i. If χ were roughly constant, and $s_{elec} \simeq s^+_{Co}$ all z_i would be maximum at the time

$$t_* = 3\tau_{CO} = 342 \text{ d} \qquad (4.14)$$

This reflects the fact that when $t << t_*$, the rapidly falling n_e dominates the decaying source, so that the degree of ionization increases. The reverse is the case when $t >> t_*$. This result, while not useful for quantitative results, illustrates some important properties of the ionization balance. The quantities within the left hand brackets of equation 4.13 depend mainly on atomic and nuclear quantities, which are in principle well known, along with a weak dependence on χ and T_e.

Since $\alpha_i \propto i^2$ and $W \propto P$, which increases rapidly with i, z_i decreases rapidly and monotonically with i. This permits us to neglect z_i above some cutoff i, or, equivalently, to truncate the set of equations 4.10. In the numerical calculations described in this and succeeding sections it was found sufficient to include terms through i = 5, so that the species FeI - VI are included. It

is evident that the sensitivity of the ionization balance to errors in atomic data is determined by the sensitivity of the balance to the parameters $w_i\alpha_{i+1}$, or equivalently α_{i+1}/σ_i. This will be addressed in section VII.

A fact of astrophysical interest demonstrated by equation 4.13 is that the value of z, and therefore the degree of ionization, is determined by the density of the nebula, N. This can most usefully be expressed in terms of the nebular density parameter,

$$\Delta = \frac{1 \times 10^6}{N_{200}} \approx \frac{U_9^3(1 - (1-h)^3)}{\mathscr{M}} \qquad (4.15)$$

where N_{200} is the atomic density (cm^{-3}) at t = 200 d. The fact that $z \propto \Delta$ is a useful result since z, being the ratio of abundances of two adjacent ions, may be estimated from the observed spectra. Meyerott (1979), in fact, has found that $z_2 \approx 4$ in the JD2441684 spectrum of SN1972e, $\approx$ 264 days after explosion. This allows an estimate of Δ through equation 4.13, and thereby places constraints on U_9, $\mathscr{M}$, and h, the quantities of most direct astrophysical interest.

This approach is effectively the one taken in section VII. It is now necessary to return to the basic ionization balance equations 4.6, which must be modified to include the effect of reabsorption within the nebula of photons emitted by radiative recombination

processes. If σ_{uv} is the absorption crossection for these photons (10^{-18} cm^2) then the optical depth of the nebula is roughly

$$\tau_{uv} \approx \sigma_{uv} N R h$$

$$\approx 6.9 \times 10^8 \sigma_{uv} \frac{\mathcal{M}}{(U_9 t)^2} \frac{h}{1 - (1-h)^3} \qquad (4.16)$$

Since σ_{uv} is typically $\gtrsim 5$ near the 3d edge for FeI-VI (Reilman and Manson 1978), τ_{uv} is quite large at t = 200, being roughly

$$\tau_{uv} \approx 1 \times 10^5 \frac{}{U_9^2} \qquad (4.17)$$

This is a familiar situation in astrophysics, for example in planetary nebulae (Osterbrock 1974), where the optical depth for photons emitted by recombination to the ground state of hydrogen is very large. In the planetary nebula case, the effect on the ionization balance equations, which have the same form as (4.6), is simply to replace $\alpha_i(T)$ with $\alpha_i^{(2)}(T)$, where $\alpha_i^{(2)}$ is the rate coefficient for recombination to excited states only. The justification for this procedure comes from the fact that $(KT/P) << 1$, where P is the ionization potential, which implies both that recombination photons are emitted very near the photoionization edge and

that the population of excited states is small. In this case a photon emitted by recombination to the ground state is immediately reabsorbed if $\tau_{uv} >> 1$, so that these processes have no net effect. On the other hand, since excited state populations are negligible, a photon emitted by recombination to an excited state will escape from the nebula, resulting in a "real" recombination.

The situation in the SNI nebula is similar, but altered in important ways due to the fact that several species of charged ion are present, as compared with only one for hydrogen. New processes now become possible in which a recombination photon is absorbed by a different ionic species than that which emitted it, so that, for example, a recombination $Fe^{+5} + e^- \rightarrow Fe^{+4} + h\nu$ may result in the ionization $Fe^{+0} + h\nu \rightarrow Fe^{+1} + e^-$. If all ions present are in the ground state (or states with $E/P << 1$), then this process can function only in one direction - to transfer ionization from a highly ionized species to one of lower ionization. In this manner recombination photons are "recycled" through the most neutral species, whose abundances may be drastically reduced as a result. Additionally, the recycling process increases slightly the already efficient heating of the electron gas implied by equation (3.47).

An accurate calculation of the recycling process requires a large amount of atomic data. In particular, the photoionization cross sections must be known as a function of photon energy for a large number of excited states of each ion. These are neither easy to calculate or measure (H. P. Kelly 1980), and are not known for

iron. These crossections are relatively well known for the ground states, however (Reilman and Manson 1978; Lombardi 1978; Hansen et al 1977; Kelly and Ron 1972). Given this situation, the recycling process has been evaluated in terms of the ground state crossections and an adjustable parameter Φ_R, the equivalent ground state recombination fraction, or "recycling fraction".

In this picture a recombination photon has a probability (1 - Φ_R) of escaping the nebula, and a probability Φ_R of behaving as if it resulted from recombination to the ground state, so that, if $\tau_{UV} >> 1$, it will be reabsorbed. Thus Φ_R includes the effects not only of real recombination to the ground state but also recombination to excited states which generate photons with significant reabsortion probability. In general, this will include all photons with hv > 7.87ev, the ionization potential of neutral iron. This allows the recycling process to be expressed in terms of the small set of ground state photoionization crossections

$$\sigma_{ij}^{Ph} = \sigma_i^{Ph}(hv_j) \tag{4.18}$$

where $\sigma_i^{Ph}(hv)$ is the ground state photo ionization crossection of Fe^{+i}, and hv_j is the photon energy resulting from recombination to the ground state of Fe^{+j}. As noted earlier $\sigma_{ij}^{Ph} = 0$ if $j < i$. The crossection of Kelly and Ron (1972) have been used

for neutral iron, and those of Reilman and Manson (1978) for positive ions, and the values adopted are listed in Table 2. If we now define

$$\sigma_{Tj}^{Ph} = \sum_{k=j}^{Z} f_k \, \sigma_{kj}^{Ph} \tag{4.19}$$

and

$$\tau_j = \sigma_{Tj}^{Ph} \, NRh \tag{4.20}$$

then the probability that a photon from recombination to Fe^{+j} will be reabsorbed is

$$P_{Tj} = \phi_R \, (1 - e^{-\tau_j}) \tag{4.21}$$

while the probability that it results in ionization of Fe^{+i} is

$$P_{ij} = \frac{f_i \, \sigma_{ij}^{Ph}}{\sigma_{Tj}^{Ph}} \, P_{Tj} \quad . \tag{4.22}$$

Thus the ionization balance equations 4.6 become

$$\dot{f}_i = -\left(\gamma_i f_i + \sum_{j>i} P_{ij}\,\alpha_{j+1}(T)\,n_e f_{j+1}\right)$$

$$+ (1 - P_{ii})\,\alpha_{i+1}(T)\,n_e f_{i+1}$$

$$+\left(\gamma_{i-1} f_{i-1} + \sum_{j>i-1} P_{i-1,j}\,\alpha_{j+1}(T)\,n_e f_{j+1}\right)$$

$$- (1 - P_{i-1,i-1})\,\alpha_i(T)\,n_e f_i = 0 \qquad (4.23)$$

As may readily be verified, the identity 4.9 is still satisfied, and the same reduction procedure may be followed to yield the analog of equation 4.10.

$$-\gamma_i f_i - \sum_{j>i} P_{ij}\alpha_{j+1}(T)n_e f_{j+1} + (1 - P_{ii})\alpha_{i+1}(T)n_e f_{i+1} = 0 \qquad (4.24)$$

Few calculations of $\alpha(T)$ for Fe^{+0} - Fe^{+5} have been performed, and no measurements are available. The available calculations (Tarter 1979, 1971) agree with the generalized form given by Allen (1973) to better than 30% and it has been adopted for all numerical calculations, so that

$$\alpha_i(T) = 3.0 \times 10^{-13}\ i^2\ T_4^{-3/4}\ \ cm^3 sec^{-1} \tag{4.25}$$

where $T_4 = T/10^4$ °K, while the rate to the ground state only is

$$\alpha_i^g(T) = 1.0 \times 10^{-13}\ i^2 T_4^{-\frac{1}{2}}\ \ cm^3 sec^{-1} \tag{4.26}$$

It is difficult to estimate ϕ_R other than to require

$$\phi_R \geq \frac{\alpha_i^g(T)}{\alpha_i(T)} = 0.33\ T_4^{0.25} \approx 0.3 \tag{4.27}$$

As will be discussed in section VII, numerical studies show that $\phi_R \approx 0.5$ is a probable value.

The magnitude of the effect of the recycling process on the abundance of neutral iron is large, as consideration of the following example shows. Let us suppose that $\phi_R = 0.5$, $f_0 = 0.2$, $f_1 = .27$ and $f_2 = .48$ (actual steady state values from a numerical calculation with $\phi_R = 0$), and compare the rate at which neutral iron is ionized by $Fe^{+2} \rightarrow Fe^{+1}$ recombinations with its recombination rate when $\phi_R = 0$. This ratio is

$$\beta = \frac{P_{01}\alpha_2 f_2}{\alpha_1 f_1} \tag{4.28}$$

With nebular parameters from Table 5 at t ≈ 200d, and crossections from Table 2, we find that

$$P_{01} = .79\ \phi_R = .40 \tag{4.29}$$

and, since $\alpha_2/\alpha_1 = 4$, that

$$\beta = 5.6\ \phi_R = 2.8 \tag{4.30}$$

In this example, ionization of neutral iron is dominantly due to recombination photons from higher ionization stages. In part this is due to the unusually small value of σ_{11} that results from the single 4s electron for Fe^{+1}. Numerical calculations show that when $\phi_R = 0.5$, the ionization balance of the example shifts to $f_0 = .001$, $f_1 = .20$, and $f_2 = .51$, confirming the large decrease in neutral iron. As will be seen in Section VII, this has a appreciable effect on the optical spectrum.

B. The Thermal Balance

In the calculation of the ionization balance above, the electron temperature T has been treated as a known quantity. In fact, however, the temperature must be determined from the equation of thermal balance which expresses the equality of the heating rate $\mathcal{S}_{elec}$ and the cooling rate $\mathscr{L}$. This problem has been quite completely treated for interstellar HI regions (Dalgarno and McCray 1972), and once again the SNI nebula is qualitatively quite similar. In particular, in both cases radiative losses are entirely due to collisionally excited atomic lines, with a negligible contribution from free-free transitions. That this must be so for the SNI nebula is clear from the fact that the loss, $\mathscr{L}_{ff}$, from free-free transitions in a thermal plasma is (Allen 1973)

$$\mathscr{L}_{ff} \approx 1.4 \times 10^{-27} \bar{z}^2 T^{\frac{1}{2}} N_e \quad \text{(erg/sec/atom)} \tag{4.31}$$

so that for $\bar{z} \approx 2$, $T \approx 7000$ °K, and $N_e \approx 10^6$ cm^{-3},

$$\mathscr{L}_{ff} \approx 4.7 \times 10^{-19} \tag{4.32}$$

On the other hand, since the thermal efficiency $\eta \approx 1$,

$$\mathcal{L}_{elec} \approx \mathcal{L}^{+}_{CO} = 2.03 \times 10^{-14} e^{-t/114} \quad \text{erg/sec/atom} \tag{4.33}$$

$$\approx 4 \times 10^{-15} \tag{4.34}$$

at 200 days, so that $\mathcal{L}_{ff}/\mathcal{L}^{+}_{CO} \approx 1 \times 10^{-4}$. Near neutral iron cools far more efficiently than would the interstellar medium at the same density and temperature, which would have $\mathcal{L}_{ISM} \lesssim 10^{-18}$ erg/sec/atom. This results from the dense array of forbidden transitions with $E \lesssim 3$ev and transition rates $10^{-3} \lesssim A \lesssim 1$ sec^{-1} that exist in Fe^{+0} - Fe^{+3} making it possible to achieve $\mathcal{L} \approx \mathcal{L}_{CO} \approx 10^{-14}$ erg/sec/atom with $T \approx 7000$ °K and $N_e = 1 \times 10^{6}$.

Once again the validity of the steady state approximation must be considered. Two new timescales must be introduced:

1) $\tau_{cool} \approx \dfrac{\frac{3}{2} \chi KT}{\mathcal{L}}$ - The dynamical cooling time

2) $\tau_{rad} \approx \dfrac{h\nu}{\mathcal{L}}$ - The average time between photon emissions for the atom, where $h\nu$ is the average photon energy.

These are readily found to be $\tau_{cool} \approx 200$ sec and $\tau_{rad} \approx 300$ sec for $h\nu \approx 2$ ev, and give a clear idea of the rate at which the thermal balance can respond to disturbances. In comparison, as discussed earlier, the nebular state changes on timescales of τ_{Co} and

τ_N which are $\gtrsim 10^6$ sec. The steady state approximation is clearly much better for the thermal balance than was the case for the ionization balance, and is adopted without further discussion.

A calculation of $\mathscr{L}$ requires that the fractional population of all excited states, along with the radiative rates of all transitions originating from them, be known, since

$$\mathscr{L}_i(T,N_e) = \sum_j q_j(T,N_e) \sum_k A_{jk}\Delta E_{jk} \tag{4.35}$$

where $\mathscr{L}_i$ is the cooling rate of Fe^{+i}, q_j is th fractional population of state j, A_{jk} is the radiative rate for the transition $j \rightarrow k$, and ΔE_{jk} the transition energy. The dependence of $\mathscr{L}_i$ on T, N_e, and the level structure of the ion is made clearer by considering for a two level system. In this case

$$\mathscr{L}(T,N_e) = q_1(T,N_e)\, A_{10}\, E_1 \tag{4.36}$$

while

$$q_1(T,N_e) = q_0(T,N_e)\left(\frac{C_{01}}{C_{10} + A_{10}}\right) \tag{4.37}$$

where the subscripts 0 and 1 designate the ground and excited states, respectively, and C_{jk} is the rate of $j \rightarrow k$ transitions due to collisions with thermal electrons. If the transition $j \rightarrow k$ is

dipole forbidden, as is the case for most important transitions in iron, then (Allen 1973)

$$C_{kj} \approx 8.6 \times 10^{-6} \frac{\Omega_{Jk}}{g_k} \frac{N_e}{T^{\frac{1}{2}}} \tag{4.38}$$

$$C_{jk} = \frac{g_k}{g_j} e^{-E_{kJ}/kT} C_{kJ} \tag{4.39}$$

where $E_{kJ} = E_k - E_J > 0$, Ω_{jk} is the collision strength or the transition, and g_i is the degeneracy of state i. This allows equation 4.36 to be rewritten as

$$\mathscr{L}(T,N_e) = q_0 \left(\frac{g_1}{g_2}\right) A_{10} E_1 e^{-E_1/KT} \left(\frac{\epsilon}{1+\epsilon}\right) \tag{4.40}$$

where

$$\epsilon(T,N_e) = \frac{C_{10}}{A_{10}}$$

$$\approx \frac{8.63 \times 10^{-6}}{A_{10}} \frac{\Omega_{10}}{g_1} \frac{N_e}{T^{\frac{1}{2}}} \tag{4.41}$$

Garstang, Robb, and Rountree (1978), hereafter GRR, have calculated collision strengths for FeIII, and these may be roughly approximated as (cf Fig. 4.1)

$$\Omega_{ij} \approx 4 \times 10^{-3}\, g_i g_j \tag{4.42}$$

If we utilize this result in equation 4.41, along with the SNI nebular parameters of Table 5 for $t \approx 200d$,

$$\varepsilon \approx 4 \times 10^{-4}\, \frac{g_0}{A_{10}} \tag{4.43}$$

The radiative transition rates from levels with $E \lesssim 3$ ev vary from roughly 10^{-3} to 1, so that

$$1 \times 10^{-3} \lesssim \varepsilon \lesssim 1 \tag{4.44}$$

The value of ε determines the density dependence of $\mathscr{L}$ in equation 4.40, since if $\varepsilon << 1$, (as is the case in an interstellar HI region), $\mathscr{L}$ is proportional to N_e while if $\varepsilon >> 1$, $\mathscr{L}$ is independent of N_e. The latter case is that of LTE, and it is clear from 4.44, that level populations in the SNI nebula will be far from LTE for $t \gtrsim 200d$. Equation 4.40 also illustrates that $\mathscr{L}$ considered as a function of the upper state energy falls off exponentially when $E/KT >> 1$, so that even if A increases rapidly with E, levels with $E/KT \gg 10$ may be left out of the calculation of $\mathscr{L}$.

Near neutral iron is far more complex than the two level system just considered. Typically fifty levels must be included for each ion to achieve sufficiently accurate results for $\mathscr{L}$ in the SNI nebula. All of these levels are collisionally coupled, and typically 100-300 radiative transitions exist between them. In this case the q_j must be obtained by solving a system of rate equations in steady state. These equations take the form

$$\dot{q}_j = - q_j \sum_k (A_{jk} + C_{jk}) + \sum_k q_k (A_{kJ} + C_{kJ}) = 0 \qquad (4.45)$$

$$\sum_j q_j = 1 \qquad (4.46)$$

where the sums are over all levels, with quantities A_{jj} and C_{jj} defined to be zero. This is a linear system which is best solved numerically using a direct inversion technique.

Although radiative rates for near neutral iron are relatively well known (cf Appendix I), few collision strengths are available, the calculations of GRR for Fe^{+2} and Fe^{+5} being the only existent data. An approximate form for the Ω_{ij} is therefore adopted

$$\Omega_{ij} = \frac{\omega g_i g_j}{8} \qquad (4.47)$$

where ω is an adjustable parameter chosen to match the GRR calculations of $\mathscr{L}_2(t,N_e)$, and found to be $\omega \approx .03$. It was found to be necessary to treat infrared transitions ($\lambda \gtrsim 10\mu$) separately, since they are anomalously strong, and the form

$$\Omega_{ij}^{IR} = 6\omega \frac{g_i g_j}{8} \tag{4.48}$$

was adopted. A comparison of the approximate Ω_{ij} and the calculation of GRR for FeIII is shown in Figure 4.1. A large scatter is evident but the values of $\mathscr{L}_2$ calculated with equations 4.35 and 4.45 matches the GRR values within 10% over their entire density and temperature range. This is due to the fact that $\mathscr{L}$, being a sum over many transitions is weakly affected by "noise" in the Ω_{ij}.

Equation 4.38 is correct only for transitions which are dipole forbidden. For allowed transitions, particularly important for FeI and II, the approximate form due to Van Regemorter (1962) has been adopted:

$$C_{jK} = 20.6\, \lambda_{kj}^3 \frac{N_e}{T^{\frac{1}{2}}} A_{kj} F\left(\frac{E_{kj}}{kT}\right) (sec^{-1}) \tag{4.49}$$

where $E_{kj} = E_j - E_k > 0$, and λ_{kj} is the wavelength of the transition in cm. For neutrals

$$F(X) \approx .066/X^{1/2} \tag{4.50}$$

while for ions

$$F(X) \approx 0.2 \tag{4.51}$$

The excitation rate C_{kj} is still given in terms of the de-excitation rate C_{jk} by relation 4.39.

Since ε tends to be small (equation 4.44) we expect $\mathscr{L}_i$ to be nearly proportional to N_e, making it convenient to work with the quantity

$$\Lambda_i(T,N_e) = \frac{1}{N_e}\mathscr{L}_i(T,N_e) \tag{4.52}$$

which will be a function of T only when ε is small. The thermal balance equation is then

$$\Lambda(T,N_e) = \sum_i f_i \Lambda_i(T,N_e) = \frac{S_{elec}}{N_e} \tag{4.53}$$

When $\varepsilon << 1$ so that $\Lambda(T,N_e) = \Lambda(T)$, equation 4.53 may be inverted for T in the form

$$T = \Lambda^{-1}\left(\frac{\mathcal{S}_{elec}}{N_e}\right)$$

$$\approx \Lambda^{-1}\left(\frac{\mathcal{S}_{Co}}{N_e}\right) \qquad (4.53)$$

where the second equality results from $\mathcal{N} \approx 1$. As was the case with the ionization balance (cf Eqn. 4.13) the temperature is determined primarily by the ratio $\mathcal{S}_{Co}/N_e$, and therefore by the nebular density parameter Δ (equation 4.15).

The calculated values of $\Lambda_i(T,N_e)$ for $i = 0 - 5$ are plotted in Figures 4.2. The data from GRR for Λ_2 are shown for comparison. Due to the fact that the first excited state of Fe^{+3} is 4 ev above the ground state, so that $E/KT \approx 7$, its cooling rate is negligible in comparison with the other ions, which typically have $E/KT \approx .05$ for the first excited state. The curves $\Lambda_i(T)$ all display a similar "double humped" shape that is a reflection of their energy level distributions (Figure 5.2). The fine structure transitions of the ground term, with wavelengths $\lambda \gtrsim 10\mu$, provide most of the cooling below $T \approx 3000$ °K. These transitions cool efficiently down to temperatures $KT \approx .05$ ev or $T \approx 500$ °K, and result in the nearly flat "plateau" in the region $500 \leq T \leq 2000$ °K. In the context of equation 4.53, the existence of the plateau implies that $T(\mathcal{S}_{Co}/N_e)$ has a near discontinuity, which when encountered from above results in a sudden drop in temperature, accompanied by a shift of

the radiated luminosity from the optical region to the infrared. This behavior will be referred to as the "infrared catastrophe" (IRC).

It is useful to define the transition temperature, T_c, for the IRC as the temperature where the optical and infrared cooling losses are equal. Looking at $\Lambda(T,N_e)$ for several different densities (Figure 4.2), it is clear that T_c increases as the density decreases, varying from $T_c \approx 2000$ °K when $N_e = 10^9$ to $T_c \approx 6000$°K when $N_e = 10^3$. This fact suggests that the IRC may occur in an SNI nebula at lates times when the falling nebular temperature meets the rising critical temperature.

It is evident from the above discussion that the ionization balance and thermal balance are coupled together in a number of ways, most importantly by the role of the average ionization, x, in the quantity $\mathcal{S}/N_e$. To obtain an accurate numerical solution it is important to use a method which ensures the simultaneous satisfaction of the ionization balance and thermal balance relations. Furthermore, these equations possess strong nonlinearities, particularly in the case of the ionization balance (equation 4.24), which require careful treatment numerically. A two level iterative scheme has been adopted for this task, which begins from an initial guess at the nebular state and iterates until self-consistency conditions are satisfied.

As a conclusion to this discussion it is useful to examine the results of a representative numerical calculation. Results from a

calculation with $\mathbf{S} = \mathbf{S}^{+}_{Co}$, $U_9 = 0.7$, $m = 0.7$, $h = 1.0$, and $\Phi_R = 0.6$ are shown in Figures 4.3. The nebular density parameter is $\Delta = .5$. Although results are shown for $50d \leq t \leq 800d$ it must be reemphasized that the solutions are not a valid representation of the nebula over this entire time span. The pictured range of t and the case $\mathbf{S} = \mathbf{S}^{+}_{Co}$ is shown solely to make the nature of the steady state solution clearer. The results are largely in accord with the simplified pictures developed earlier. Both X and T reach their maxima very near the predicted time of 342d (cf equation 4.14). The heating efficiency is very close to unity, as expected. The IRC shows up in the rapid increase of $\mathscr{L}_{IR}$ beginning near 450 d. Comparison with results from a calculation with $\Phi_R = 0$, also shown in Figures 4.3, illustrates the effect of the reabsorption of recombination radiation on the abundance of neutral iron.

TABLE 2

Values of σ_{ij}^{Ph} (10^{-18} cm^2)

	j = 1	2	3	4	5
i = 1	5.	5.	7.	8.	8.
2	0	.1	9.	9.	7.
3		0	8.5	9.	7.2
4			0	7.5	6.
5				0	5.5

Figure Captions

Fig. 4.1 The FeIII collision strengths calculated by Garstang, Robb, and Roundtree (1978) are shown, and compared with the approximation used in the numerical calculations (equation 4.47).

Fig. 4.2 Cooling curves for FeI, II, and III are shown for electron densities of 10^3, 10^5, and 10^7 (cm^{-3}). The cooling due to infrared ($\lambda > 1\mu$) and optical ($\lambda < 1\mu$) transitions are shown as separate curves. The critical temperature, T_c, is determined by their crossing point. Fig. 4.2h shows data points from Garstang, Robb, and Rountree (1978).

Fig. 4.3 Results from numerical run with $\mathcal{M} = 0.7$, $U_9 = 0.7$, $h = 1$, and $\mathbf{S} = \mathbf{S}^{+}_{Co}$ are plotted versus time in days. In c-f results are shown for $\Phi_R = 0.6$ on the left hand frame and for $\Phi_R = 0$ on the right.

a) Source rate, $\mathbf{S}$ (erg/atom/sec)

b) Atomic density, N (cm^{-3})

c) Average ionization, x

d) Temperature, T (°K)

e) Fractional ion abundances, f. The label 1 designates FeI, etc.

f) Fraction of luminosity radiated in the infrared ($\lambda > 1\mu$).

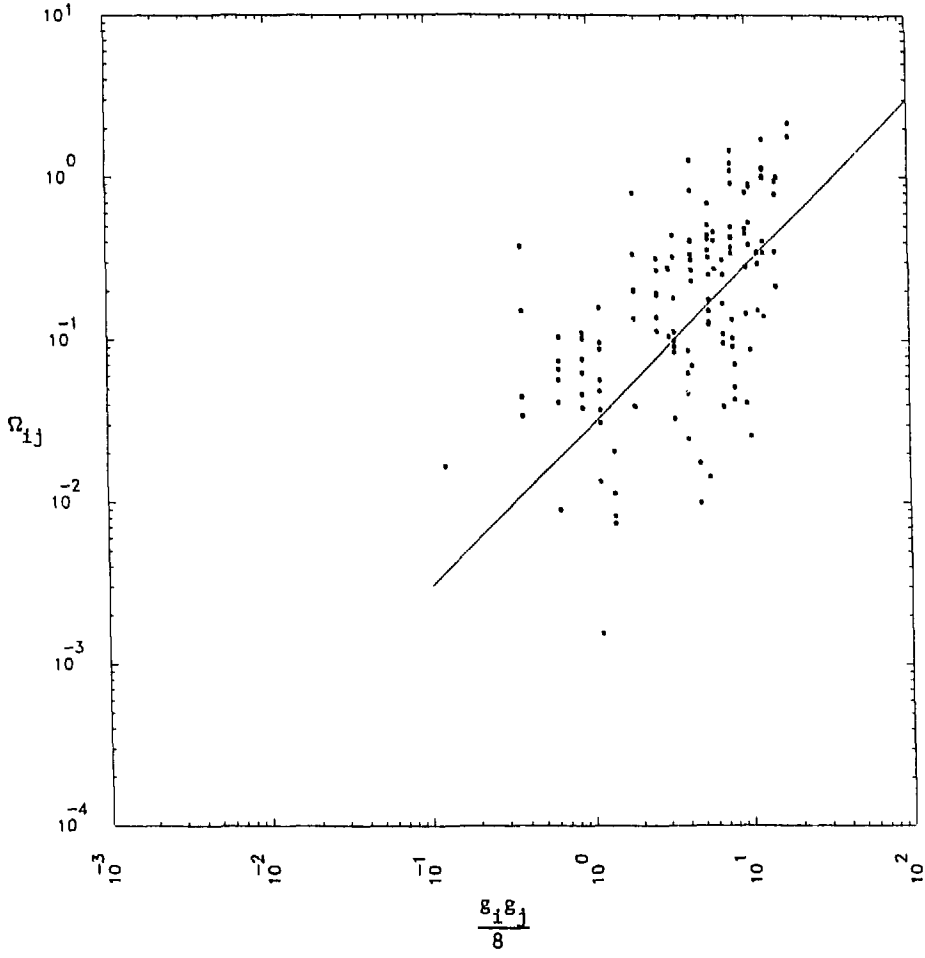
10^{1}
10^{0}
10^{-1}
10^{-2}
10^{-3}
10^{-4}
Ω_{ij}
10^{-3}
10^{-2}
10^{-1}
10^{0}
10^{1}
10^{2}
$\frac{g_i g_j}{8}$

Fig. 4.1

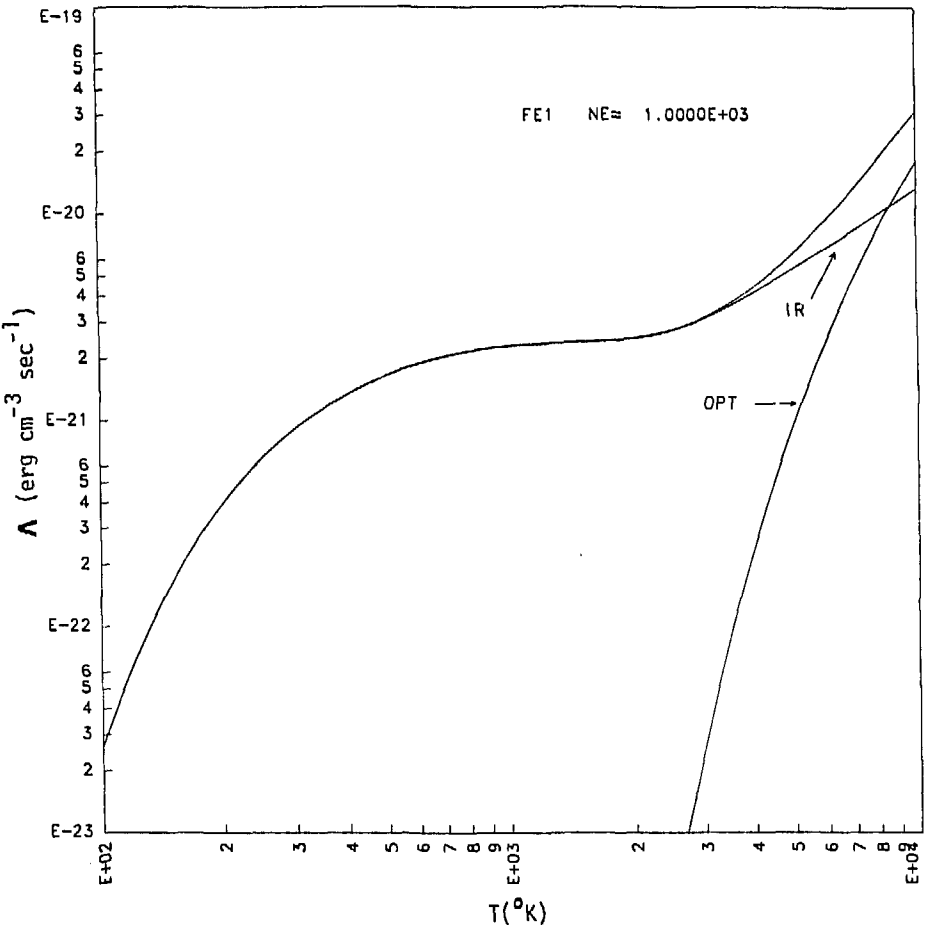
FE1 NE= 1.0000E+03
IR
OPT
Λ (erg cm^{-3} sec^{-1})
T(°K)
E-19
E-20
E-21
E-22
E-23
E+02
E+03
E+04

Fig. 4.2a

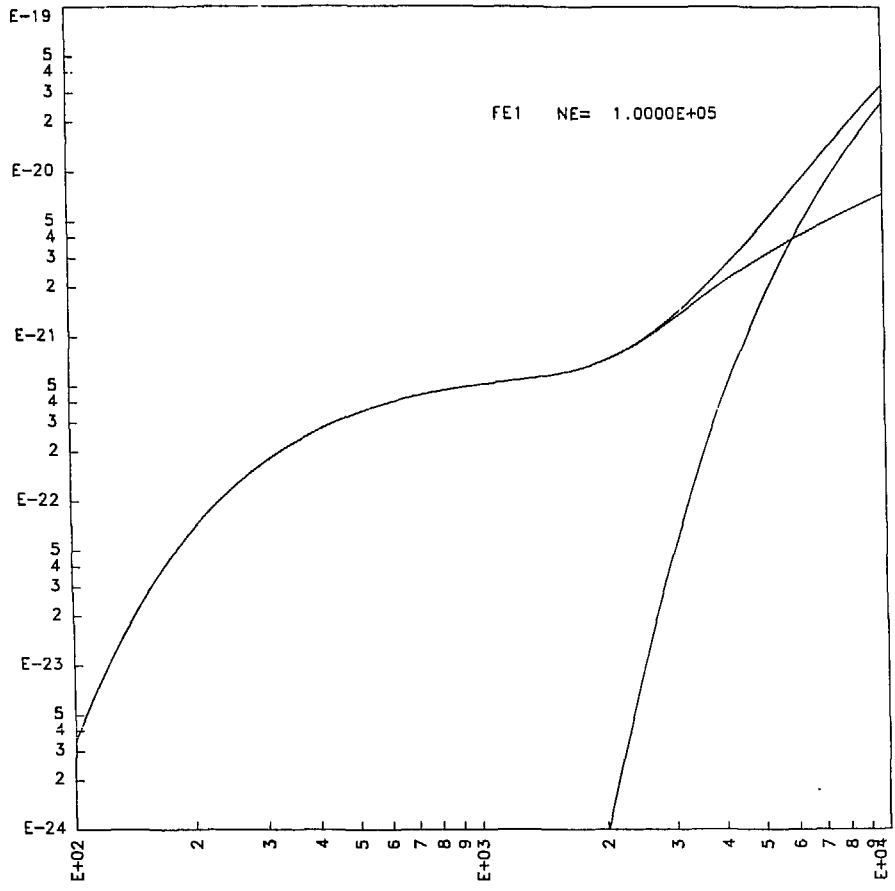

Fig. 4.2b

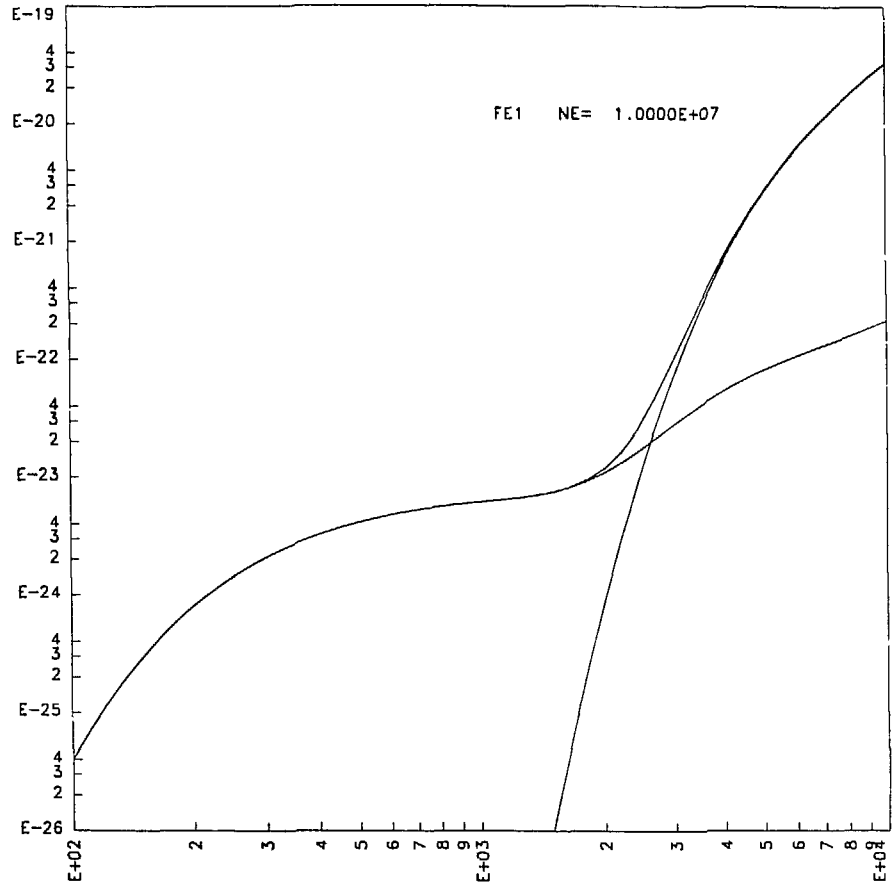

Fig. 4.2c

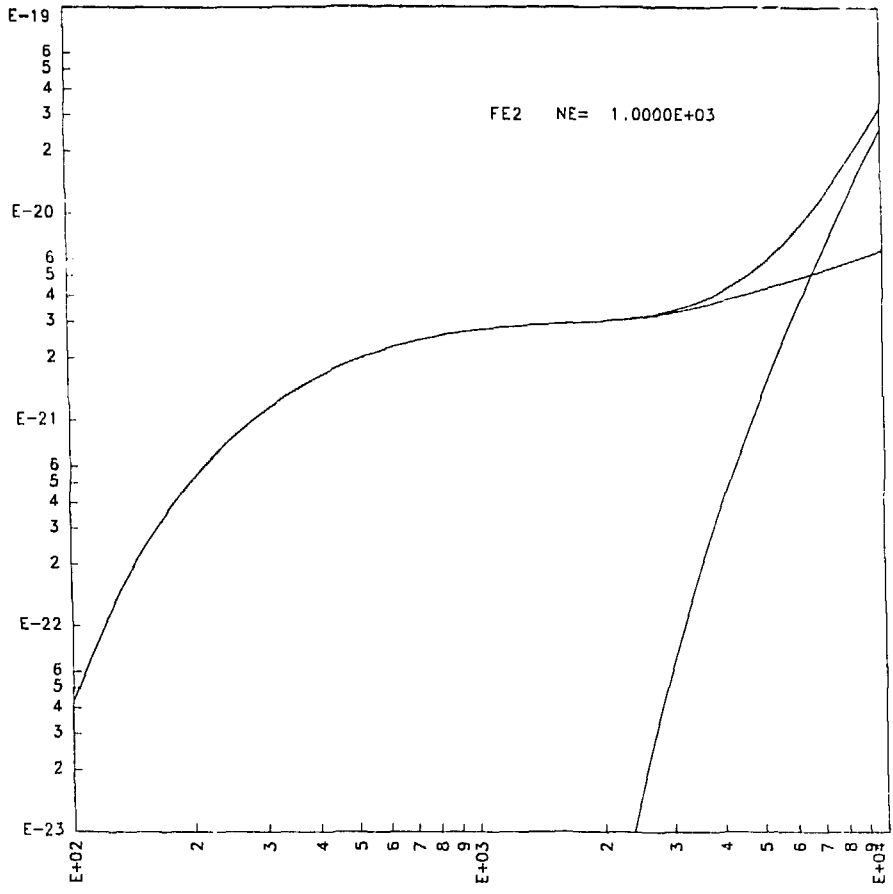

Fig. 4.2d

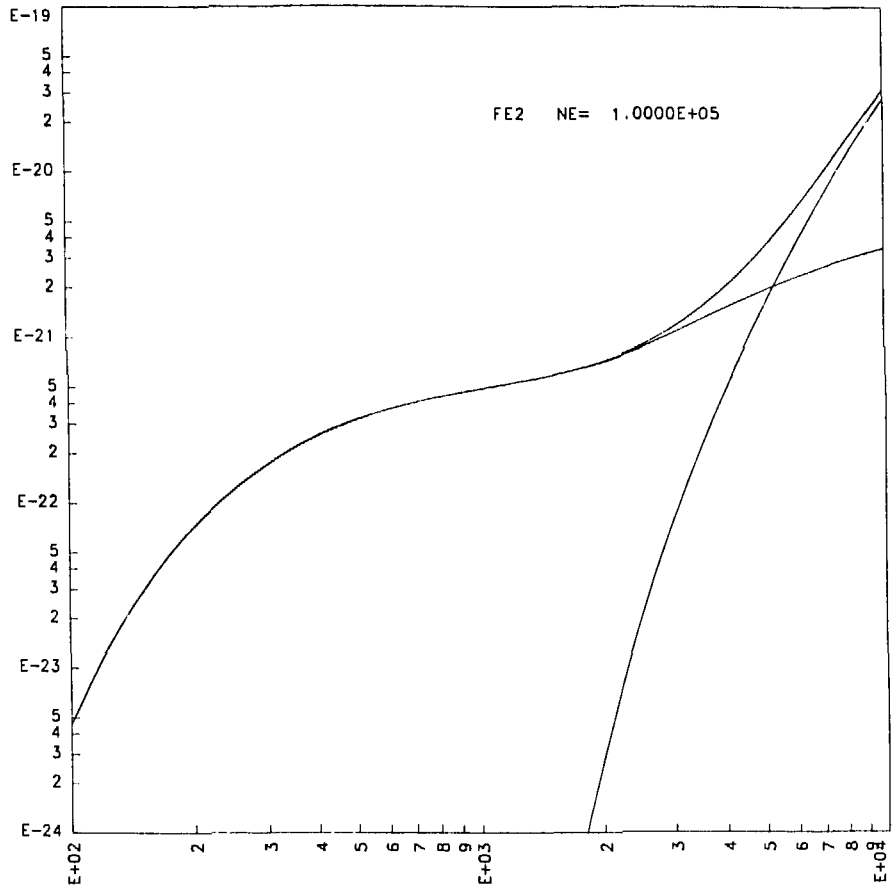

Fig. 4.2e

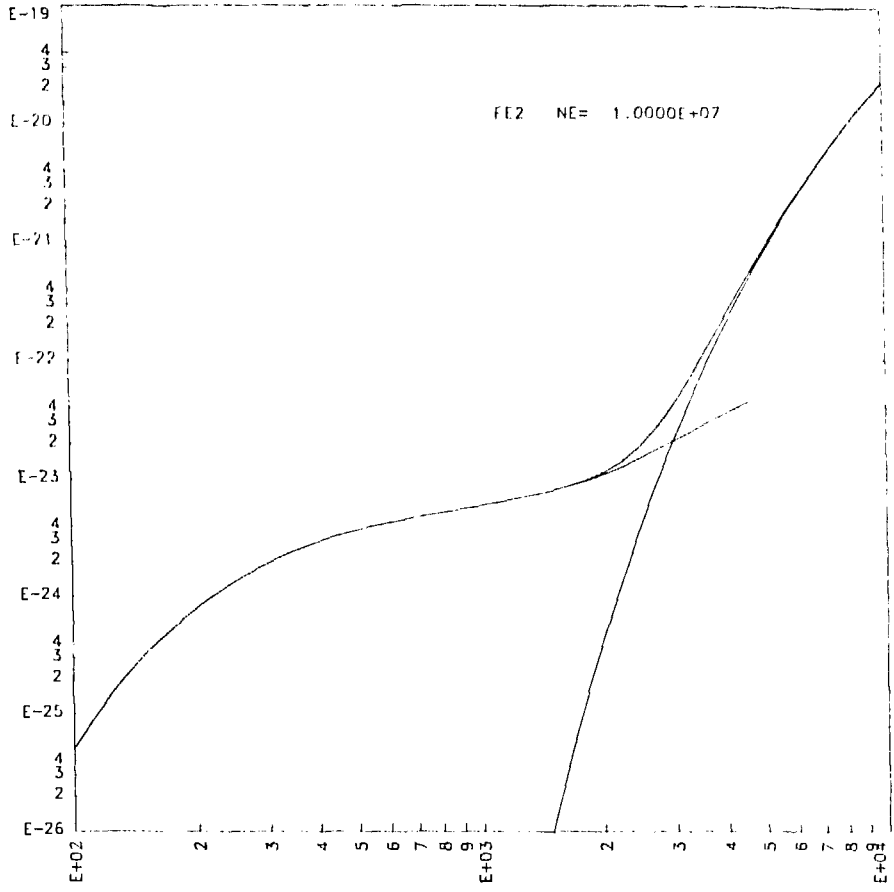

Fig. 4.2f

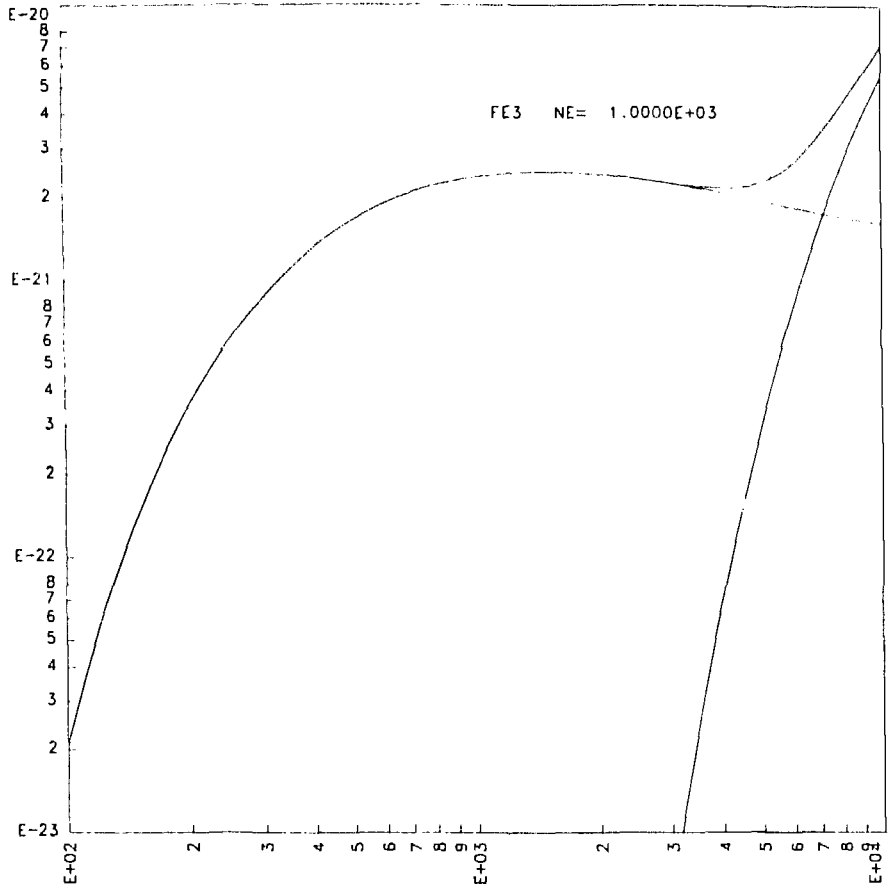

Fig. 4.2g

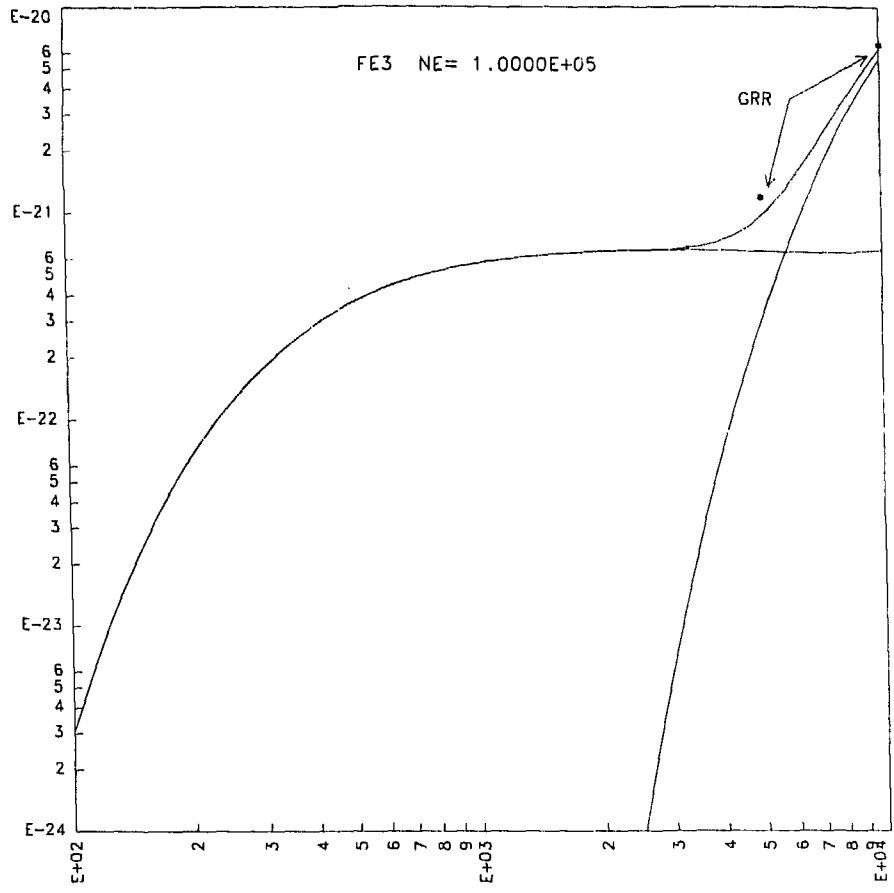

Fig. 4.2h

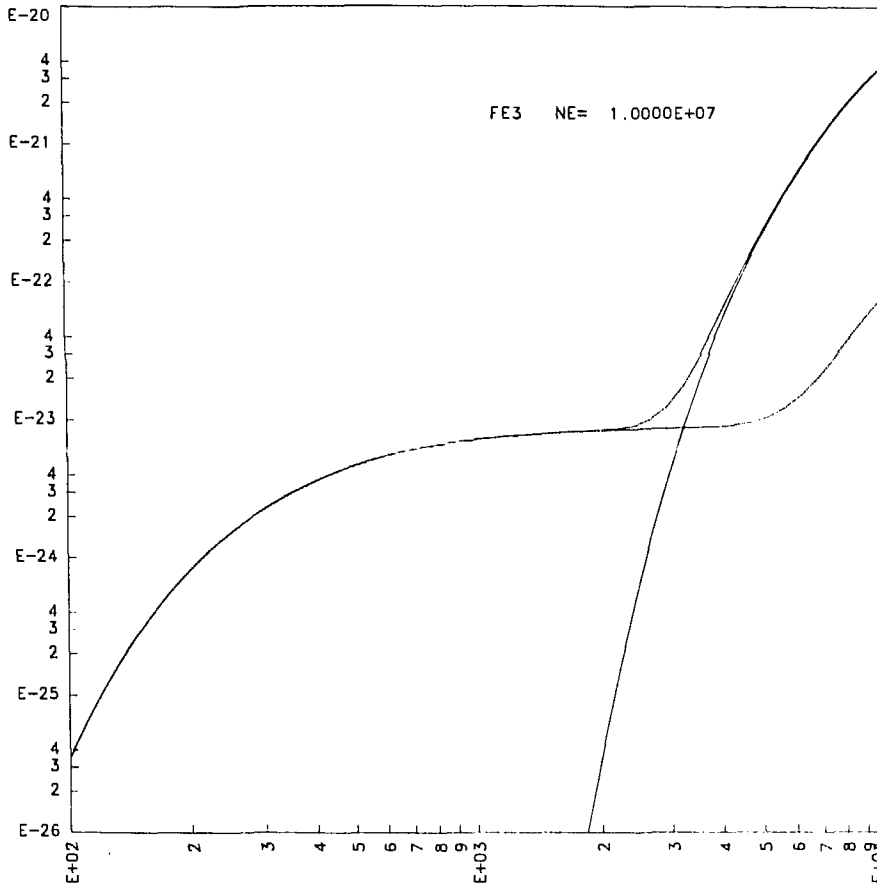

Fig. 4.2i

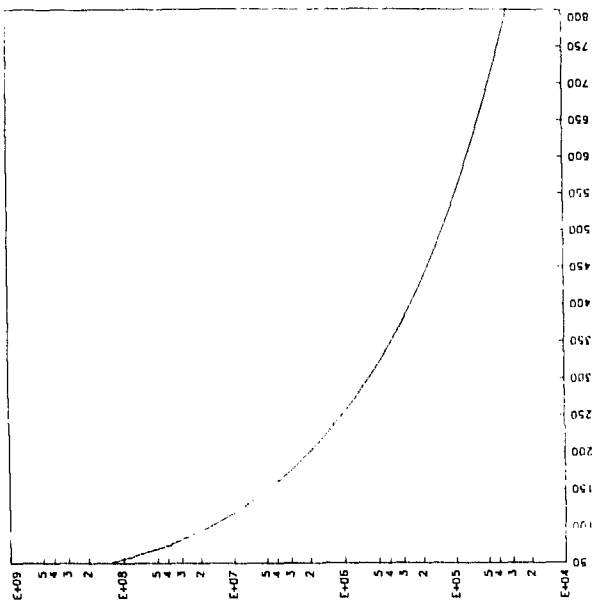

Fig. 4.3b

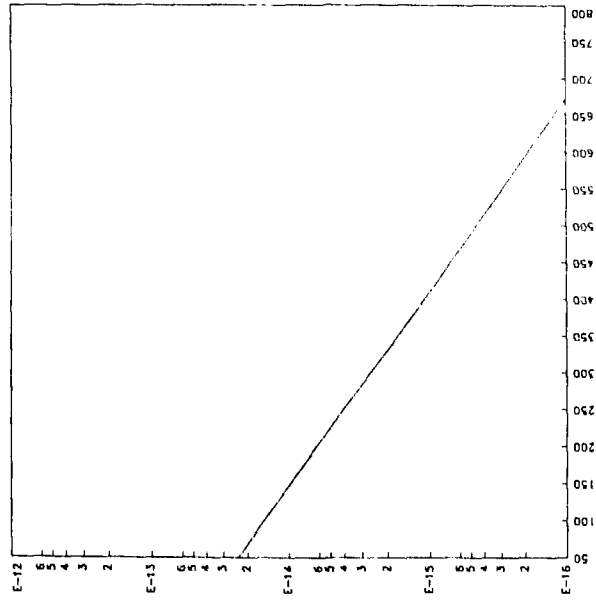

Fig. 4.3a

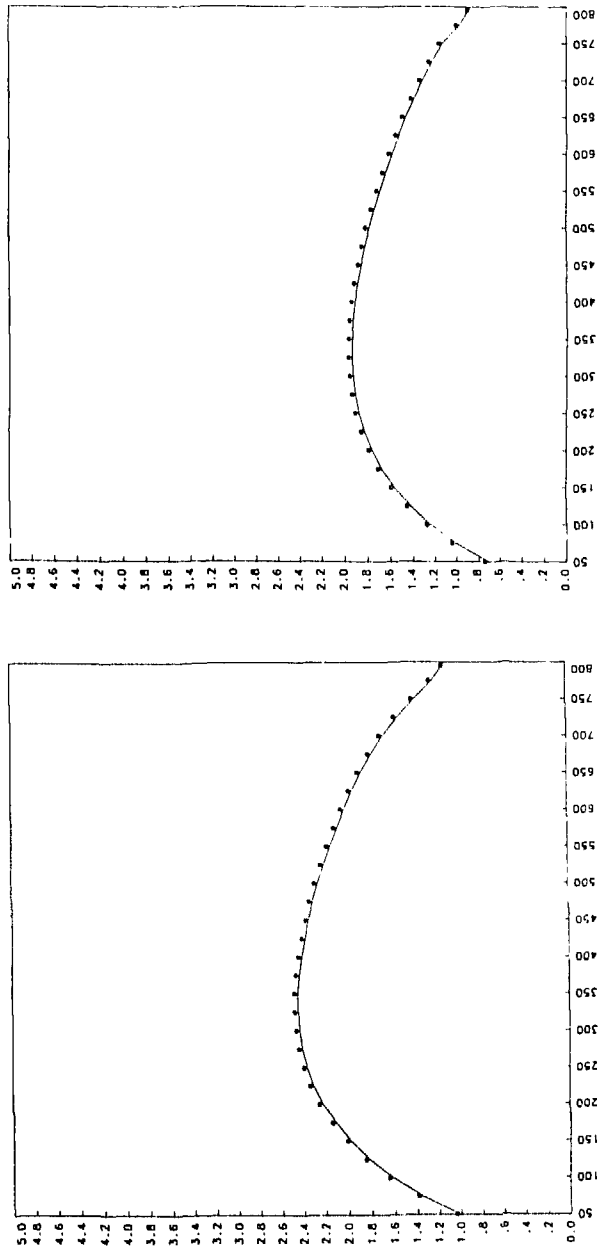
0.0
.2
.4
.6
.8
1.0
1.2
1.4
1.6
1.8
2.0
2.2
2.4
2.6
2.8
3.0
3.2
3.4
3.6
3.8
4.0
4.2
4.4
4.6
4.8
5.0
50
100
150
200
250
300
350
400
450
500
550
600
650
700
750
800

Fig. 4.3c

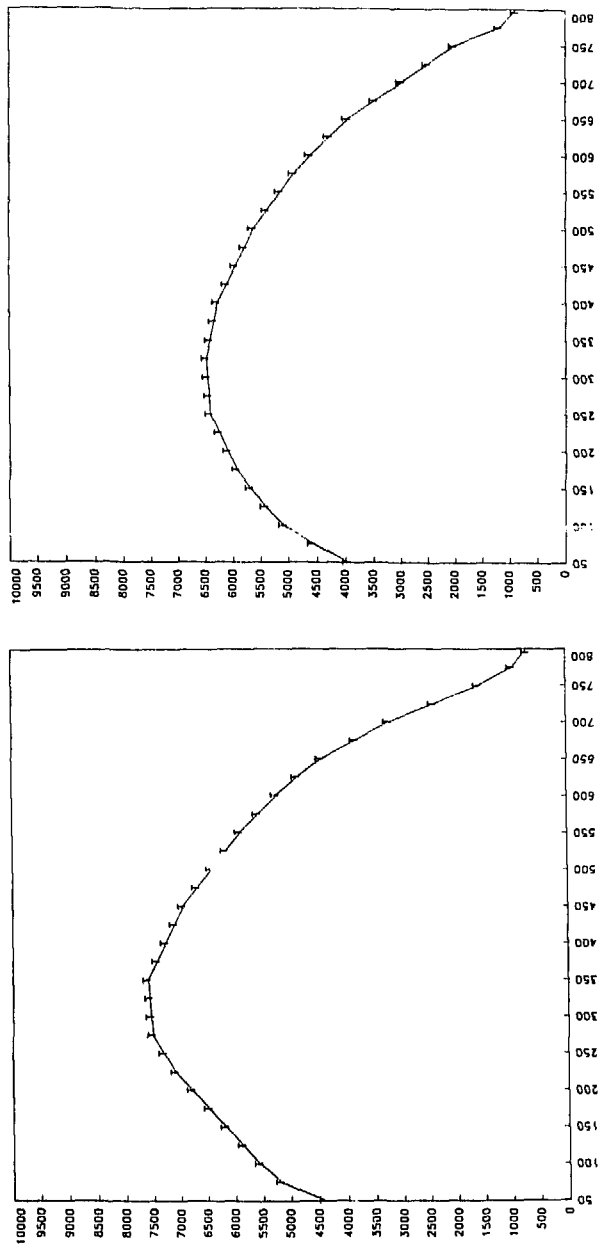
10000
9500
9000
8500
8000
7500
7000
6500
6000
5500
5000
4500
4000
3500
3000
2500
2000
1500
1000
500
0
50
100
150
200
250
300
350
400
450
500
550
600
650
700
750
800

Fig. 4.3d

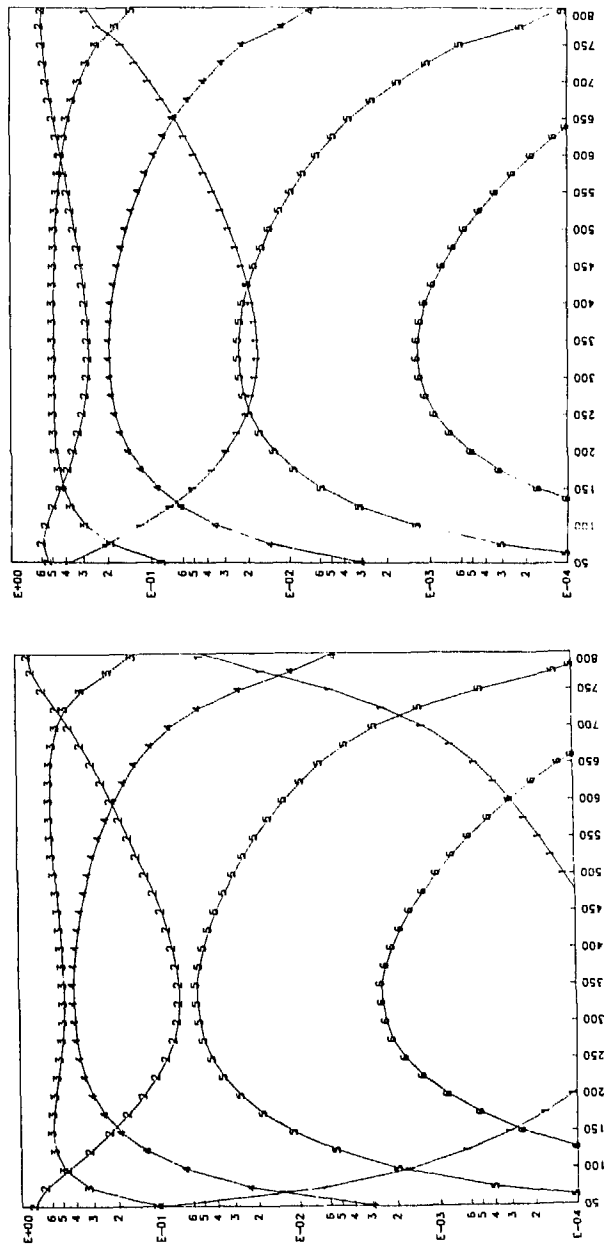
E+00
E-01
E-02
E-03
E-04
50
100
150
200
250
300
350
400
450
500
550
600
650
700
750
800

Fig. 4.3e

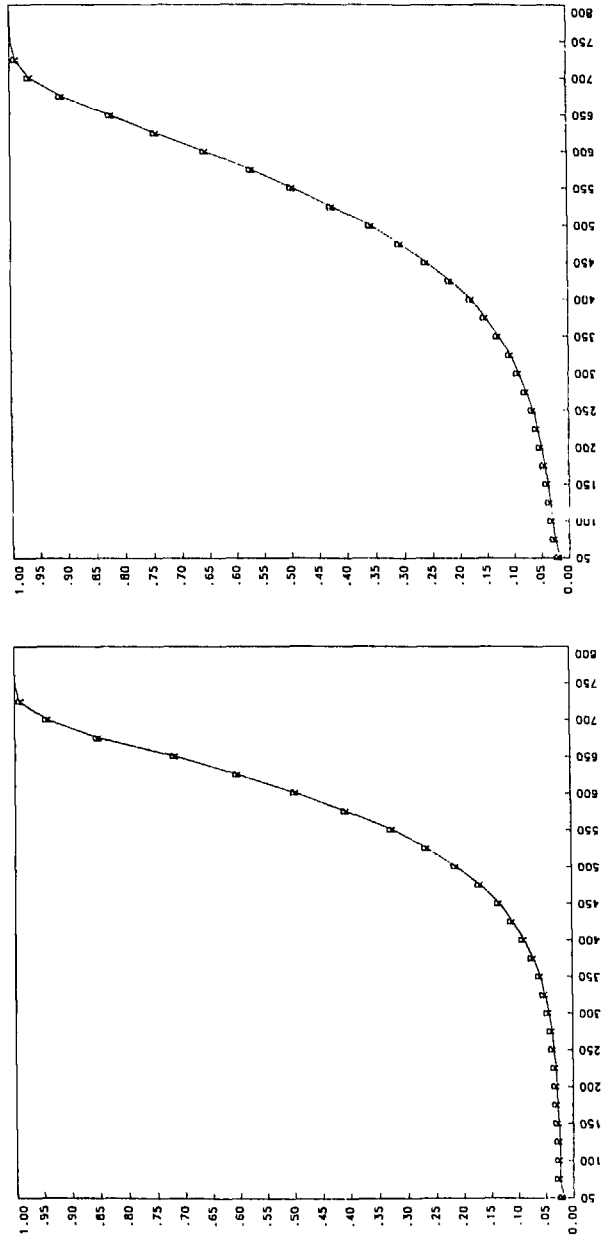
1.00
.95
.90
.85
.80
.75
.70
.65
.60
.55
.50
.45
.40
.35
.30
.25
.20
.15
.10
.05
0.00
50
100
150
200
250
300
350
400
450
500
550
600
650
700
750
800

Fig. 4.3f

V. The Emergent Spectrum

If the SNI nebula were transparent at all optical wavelengths, the emergent spectrum could be calculated immediately from the level populations, q_i, determined in IV, as

$$F(\nu) = \sum_n f_n \sum_j q_i^n \sum_K A_{jk}^n \Delta E_{jk}^n \Phi_{jk}^n(\nu) \qquad (5.1)$$

Here $F(\nu)$ is the monochromatic flux (erg/sec/Hz/atom), q_j is the fractional population of level j, A_{jk} is the radiative transition rate from level j to level k (sec^{-1}), ΔE is the transition energy (erg), and Φ is the emergent lineshape (Hz^{-1}). As before, f_n is the fractional abundance of ion n, and the superscript n on A, ΔE, and Φ refers to ion n. The only unknown quantity in this expression is the emergent lineshape, $\Phi(\nu)$. In practice, it is convenient to work in a notation in which each transition is specified by a single unique index, i, and each level by an index ℓ. Then $F(\nu)$ may be expressed as

$$F(\nu) = \sum_\ell \overset{\curvearrowleft}{q}_\ell \sum_{i\epsilon\ell} A_i \Delta E_i \Phi_i(\nu) \qquad (5.1a)$$

where

$$\hat{q}_{\ell} = f_n q_{\ell}^n \tag{5.1b}$$

so that

$$\sum_{\ell \varepsilon n} \hat{q}_{\ell} = f_n \tag{5.1c}$$

The notation $i\varepsilon\ell$ signifies summation over all transitions i which have ℓ as their upper level, and $\ell\varepsilon n$ signifies summation over all levels of ion n.

This simple picture in which the emergent spectrum is formed by the super-position of emission lines, while qualitatively correct, must be modified to account for the presence of numerous strongly absorbing lines, predominantly originating from low levels of FeI. The optical depths of these lines are not determined by the spatial extent of the nebula, as would be appropriate for a static medium, but rather by its velocity gradient. This arises from the fact that as a photon traverses the expanding nebula it is progressively redshifted as viewed in inertial frames in which the nebular material is at rest. If the redshift across the nebula is large compared with the linewidth of the absorbing line, absorption can occur only

over a small fraction of the pathlength where the photon is redshifted into resonance with the absorbing line, so that the optical depth remains finite even if the nebula is of infinite extent.

This condition is well satisfied by the SNI nebula. The maximum redshift across the nebula is

$$Z = \frac{\Delta\nu}{\nu} \approx \frac{2U}{c} = 6.7 \times 10^{-2}\ U_9 \tag{5.2}$$

On the other hand, a strong FeI line has a transition rate $A \approx 10^8$ sec^{-1} and $\nu \approx 10^{15}$ sec^{-1} so that

$$\frac{\Delta\nu_{nat}}{\nu} \approx 10^{-7} \tag{5.3}$$

where $\Delta\nu_{nat}$ is the natural linewidth. The thermal doppler width is only slightly larger, being

$$\frac{\Delta\nu_{dop}}{\nu} \approx \frac{U_{th}}{c} \approx \frac{\sqrt{\frac{2KT}{m}}}{c} \approx 4 \times 10^{-6} \tag{5.4}$$

where T has been taken as 6000 °K. For $U_9 \approx 1$ the linewidth is smaller than the expansion redshift by a factor of about 10^4.

Consider now a photon emitted within the nebula at a frequency ν_e, and let s be the distance coordinate along its path, so that s = 0 at the point of emission. The optical depth of an allowed transition with absorption crossection $\sigma(\nu)$ is then simply

$$\tau(\nu_e) = \int_0^{s_{esc}} N_\ell \, \sigma(\nu(s;\nu_e)) \, ds \tag{5.5}$$

where $\nu(s;\nu_e)$ is the frequency of the photon as measured in the rest frame of nebular material located at s, N_ℓ is the number density of atoms in the lower state of the absorbing transition, and s_{esc} is the distance to the edge of the nebula along the photon's path. The frequency $\nu(s)$ is given by the Lorentz transform

$$\nu(s;\nu_e) = \frac{\nu_e \left(1 - \frac{\hat{e}}{c} \cdot (\vec{U}_s - \vec{U}_e)\right)}{\sqrt{1 - \frac{|\vec{U}_s - \vec{U}_e|^2}{c^2}}} \tag{5.6}$$

where $\hat{e}$ is the unit vector along the photon's path, while $\vec{U}_e$ and $\vec{U}_s$ are the nebular velocities at the emission and absorption points. The fact that the nebula is expanding homologously, so that the velocity at any point $\vec{r}$ is

$$\vec{U} = \left(\frac{1}{t}\right)\vec{r} \tag{5.7}$$

allows the expression (5.6) to be simplified considerably, since then

$$\vec{U}_s - \vec{U}_e = \left(\frac{1}{t}\right)(\vec{r}_s - \vec{r}_e) = \frac{s}{t}\,\hat{e} \tag{5.8}$$

Additionally, from (5.2) it is clear that the denominator of 5.6 may be replaced by unity to an accuracy of better than 1 percent, so that we obtain

$$\nu(s;\nu_e) = \nu_e\left(1 - \frac{s}{ct}\right) \tag{5.9}$$

The expression (5.5) for τ can then be rewritten as

$$\tau(\nu_e) = N_\ell \frac{Ct}{\nu_e} \int_{\nu_{esc}}^{\nu_e} \sigma(\nu)d\nu \tag{5.10}$$

where

$$\nu_{esc} = \nu_e(1 - \frac{S_{esc}}{ct}) \tag{5.11}$$

If ν_e satisfies

$$\nu_e > \nu_a + \Delta\nu_a$$

and (5.12)

$$\nu_{esc} < \nu_a - \nu_a$$

where ν_a is the center frequency of the absorbing transition and $\Delta\nu_a$ is its intrinsic linewidth (cf equations 5.3 and 5.4), then the integral of 5.10 extends over the entire line profile and we obtain

$$\tau(\nu_e) = N_\ell \frac{ct}{\nu_\ell} \frac{\pi e^2}{mc} f \tag{5.13}$$

where f is the oscillator strength of the transition. On the other hand, if

$$\nu_e < \nu_a - \Delta\nu_a \tag{5.14}$$

or

$$\nu_{esc} > \nu_a + \Delta\nu_a \tag{5.15}$$

then $\tau = 0$. Bearing in mind the fact that the intrinsic linewidth is completely negligible in comparison with the redshift across the nebula, we see that one of the conditions 5.12, 5.14, or 5.15 will be satisfied for any emitted photon, unless it has been emitted by the same transition which does the absorbing, in which case $\nu_e \approx \nu_a$. It is convenient to replace ν_e in (5.13) by ν_a, which may be done with negligible error due to the smallness of the maximum redshift given by (5.2). The final result for τ when 5.12 is satisfied is then independent of ν_e and given by

$$\tau = .28\, N_\ell \frac{ft}{\Delta E_{ev}} \tag{5.16}$$

where t is the time in days and ΔE_{ev} the transition energy in ev.

In spite of the fact that the abundance of neutral iron is extremely small, the optical depth of allowed lines given by (5.13) are typically large. Making use of the example of section IV for $t \approx 200d$ (cf Figures 4.3), we find that

$$N_\ell = f_0 q^\circ_\ell N \approx 100\, q^\circ_\ell \ (cm^{-3}) \tag{5.17}$$

At a temperature of 6000°K, the fractional population of the ground state (ℓ=0), q°_o, is of the order unity, so that for absorptions from the ground state

$$\tau \approx 5600 \frac{f}{\Delta E_{ev}} \tag{5.18}$$

For a strong transition of neutral iron with $f \approx 0.1$ and $\Delta E_{ev} \approx 4$, we see that

$$\tau \approx 140 \tag{5.19}$$

Figure 5.1 shows the optical depths of all allowed lines present in a typical numerical run at times of 87 and 264 days. Although most lines originate from FeI, some lines from FeII and CoI are also present. A significant fraction of the wavelength region shortward of 4500 Å is blocked by allowed lines with $\tau > 1$. Clearly for choices of nebular parameters which result in higher density and/or higher FeI abundance than the example chosen, this blocking will be virtually complete. The importance of spectral lines from metals in the distortion of the blue end of the SNI spectrum has previously been emphasized by Mustel (1975). This distortion is the principle reason that attempts to fit SNI spectra with black-bodies (cf. VI) are not very successful.

What is the fate of a photon absorbed by an allowed transition in the SNI nebula? For a two level atom, the answer is simple: the photon will be repeatedly emitted and reabsorbed by the same transition until it either escapes or is thermalized. As discussed by Sobolev (1957), who was the first to treat the problem of radiative transfer in an expanding medium in this form, the photon escapes

from a strong line through emission near the redward limit of the line profile, where the probability of further interaction with the line is small. The escape probability, β, is simply

$$\beta = \int_0^\infty \phi(\nu)\, e^{-\tau(\nu)} d\nu \qquad (5.20)$$

with $\tau(\nu)$ from equation 5.10. It is important to realize that the only significant contribution to the integral comes for frequencies where the conditions 5.12 - 5.15 are <u>not</u> satisfied, so that equation 5.16 is not valid. Under the assumption of complete redistribution, so that emission and absorption lineshapes are identical (cf Mihalas 1978), this expression is readily evaluated to give

$$\beta = (1 - e^{-\tau})/\tau \qquad (5.21)$$

where τ is given by equation 5.16.

The thermalization probability is completely negligible for the SNI nebula, as may readily be determined. The thermalization probability per absorption is simply the ratio of the collisional de-excitation rate for the upper level to the radiative decay rate, already introduced in Section IV as ε (cf equations 4.41 - 4.43).

The transitions under consideration there, however, were dipole forbidden, with correspondingly small radiative decay rates. For allowed transitions, while the collisional rates are roughly comparable, the radiative rates are larger by many orders of magnitude. Utilizing equation 4.49 for the collisional rate, as appropriate for allowed transitions, we obtain

$$\varepsilon \approx 4 \times 10^{-16} N_e \tag{5.22}$$

where values of $\lambda = 4000$ Å and $T = 6000$ °K have been used to evaluate 4.49. We are expecting $N_e \approx 10^6$ so that $\varepsilon \approx 4 \times 10^{-10}$. The number of scatterings required to escape, N_{esc}, is determined approximately as

$$(1 - \beta)^{N_{esc}} \approx 1/e \tag{5.23}$$

If $\tau >> 1$, then we find from equation 5.21 that $\beta \approx 1/\tau$ and this results in

$$N_{esc} \approx \tau \tag{5.24}$$

The probability that the photon thermalizes before it escapes, P_{th}, is then roughly

$$P_{th} \approx \epsilon N_{esc} \approx 10^{-7} \tag{5.25}$$

for $\tau \approx 200$, which can be neglected.

For a two level atom then, we have answered the question posed above. A photon absorbed by an allowed transition is scattered within the line approximately N_{esc} times and then escapes the nebula. Almost no change results to the emergent spectrum by equation 5.1. The effect of the allowed lines is solely to modify the emergent line profiles, $\phi(\nu)$, and, as will become clear in Section VII, the resulting change in $F(\nu)$ is difficult to observe. For a multilevel atom, the situation is fundamentally different. The upper level of an allowed transition may now have several possible radiative decays, which may have radically differing optical depths, and thus, escape prababilities. Processes now become possible in which a photon absorbed at a frequency ν_a may escape from the nebula as one or more photons at lower frequencies. For many transitions of FeI a down-conversion process of this type is overwhelmingly likely when optical depths are large.

As a simple example, consider the λ 3896 transition from the z^5D level of FeI at 26550 cm^{-1} (cf Appendix I). One other transition originates from this level: the λ 5434, which has as a lower state the a^5F level at 8154 cm^{-1}. Let us calculate the probability, P_{12}, that a photon absorbed as λ 3896 (transition 1) escapes as λ 5434 (transition 2). Utilizing the data of Appendix I and supposing $\tau_1 = 100$ while $\tau_2 << 1$, we obtain the following:

$$A_1 = 9.40 \times 10^6 \qquad A_2 = 1.71 \times 10^6$$

$$\beta_1 = .01 \qquad \beta_2 = 1$$

It is simplest to first determine the probability P_{11}. Let

$$C = \frac{A_2}{A_1 + A_2} = .15 \tag{5.26}$$

Then P_{11} can be expressed as

$$P_{11} = (1 - c)\beta_1 + (1 - \beta_1)(1 - c)P_{11} \tag{5.27}$$

or

$$P_{11} = \frac{(1 - c)\beta_1}{1 - (1 - \beta_1)(1 - c)} = .05 \tag{5.28}$$

so that

$$P_{12} = 1 - P_{11} = .95$$

The downconversion efficiency is thus close to unity, and we expect that the distribution of allowed lines shown in Figure 5.1 will

result in considerable transformation of the spectrum given by equation 5.1.

A general formalism must now be developed to determine this transformation for the SNI nebula. We begin by collecting all radiative transitions, forbidden and allowed, from all ions, and forming an ordered set containing all of them, addressed by a single index, i. The transitions are ordered by decreasing frequency, so that i=1 corresponds to the transition with the highest frequency. Each transition has the following quantities associated with it:

ν_i - frequency of the transition (sec^{-1})

A_i - radiative transition rate (sec^{-1})

τ_i - optical depth from equation 5.16

β_i - escape probability from equation 5.21

τ_i is defined to be zero for forbidden transitions, so that $\beta_i = 1$.

Consider photons being emitted isotropically by the i'th transition at radial position r within the nebula (see Figure 5.2). In general this photon has a possibility of being absorbed by any of a large number of allowed lines as it travels toward the boundary of the nebula. Due to the fact that the intrinsic linewidths are all negligible in comparison with the redshift across the nebula, absorptions by a transition j may be conceived to occur on a geometrical surface within the nebula determined by the satisfaction of the resonance condition. The fact that the velocity gradient in the nebula is isotropic gives these surfaces a simple form: they are

spheres of radius s_{ij} centered on the emission point and intersected with the nebular shell. Figure 5.3 shows the form of these surfaces. The radius s_{ij} is determined by utilizing equation 5.9 and requiring

$$\nu(s_{ij};\ \nu_i) = \nu_j \tag{5.30}$$

This leads to

$$s_{ij} = \left(\frac{\nu_i - \nu_j}{\nu_i}\right) ct \tag{5.31}$$

which may be rewritten utilizing equation 5.2 and the fact that $t = U/R$ as

$$s_{ij} = 2R\,\frac{z_{ij}}{z} \tag{5.32}$$

where $$z_{ij} = \frac{\nu_i - \nu_j}{\nu_i}$$

The first quantity we need to calculate is α_{ij}, the probability that a photon emitted by i is absorbed by j. It is important to realize that α_{ij} is well defined where $i = j$ and is simply

$$\alpha_{ii} = 1 - \beta_i \tag{5.34}$$

Recalling the way in which the set of transitions is ordered, we also know that

$$\alpha_{ij} = 0 \qquad (j > i) \tag{5.35}$$

Looking once again at Figure 5.3, it is clear that for $j > i$, α_{ij} depends on both r and $\mu = \cos\theta$. Futhermore, a simple method for calculating $\alpha_{ij}(r,\mu)$ is evident: one sums up the optical depths of all absorption surfaces crossed in the propagation between i and j (but not including either i or j) to form the quantity $T_{ij}(r,\mu)$, and then

$$\alpha_{ij}(r,\mu) = \beta_i e^{-T_{ij}(r,\mu)} (1 - e^{-\tau_j}) \qquad (j > i) \tag{5.36}$$

If the propagation path exits the nebula before reaching the absorption surface of j, we define $T_{ij}(r,\mu) = \infty$ so that $\alpha_{ij}(r,\mu) = 0$. It is useful to define a quantity $B_i(r,\mu)$ as the probability that the emitted photon is not absorbed by any transition (including its parent, transition i) and thus escapes the nebula. Clearly this is given by

$$B_i(r,\mu) = 1 - \sum_j \alpha_{ij}(r,\mu) \tag{5.37}$$

where the sum over j includes all transitions (in view of equation 5.35 the sum can be restricted to $j \geq i$).

Except for the calculation of the emergent line profile, Φ, we are interested not in $\alpha_{ij}(r,\mu)$ but rather its average value for the entire nebula, which will be denoted as α_{ij}. In keeping with the assumptions made throughout this paper we will content ourselves with the simplest possible approximation in forming this average: all level populations (and therefore emission rates and escape probabilities) are independent of radius within the nebula. In this case,

$$\alpha_{ij} = \frac{1}{2V} \int_{(1-h)R}^{R} dr\, 4\pi r^2 \int_{-1}^{1} d\mu\, \alpha_{ij}(r,\mu) \tag{5.38}$$

where V, the the volume of the nebula is

$$V = \frac{4\pi}{3} R^3 \left[1 - (1-h)^3\right] \tag{5.39}$$

Substitution of equation 5.36 into 5.38 leads to

$$\alpha_{ij} = \beta_i(1 - e^{-\tau_j}) \frac{2\pi}{V} \int_{(1-h)R}^{R} dr\, r^2 \int_{-1}^{1} d\mu e^{-T_{ij}(r,\mu)} \tag{5.40}$$

Even the simplest possible case, where only two transitions exist, leads to a tedious calculation if this expression is evaluated analytically, and the result is useful principally as a check on the accuracy of the numerical calculation. If h = 1, however, the calculation is simple and the result is

$$\alpha_{12} = \beta_1(1 - e^{-\tau_2})\ (1 - \frac{3}{2}\,\zeta_{12} + \frac{1}{2}\,\zeta_{12}^3) \tag{5.41}$$

$$\text{where} \quad \zeta_{12} = \frac{z_{12}}{z} \leq 1 \tag{5.42}$$

As one would expect, α_{12} has its maximum value for $\zeta_{12} \to 0$, and $\alpha_{12} \to 0$ as $\zeta_{12} \to 1$. This reflects the fact that for $\zeta_{12} \to 1$ only photons emitted near the edge of the nebula with $\mu \approx -1$ have any possibility of being absorbed by transition 2.

The numerical evaluation of α_{ij} by equation 5.40 is straightforward, although care must be taken to achieve efficiency, since many thousands of double integrals must be evaluated. As is clear from Figure 5.3, considered as a function of μ, $T_{ij}(r,\mu)$ is piecewise constant. This fact, along with the frequency ordering of the linelist, allows the angular integral in equation 5.40 to be evaluated rapidly and exactly as a discrete sum. The r-integral is performed by an adaptive Romberg method. Having evaluated α_{ij} for all transitions, the average nebular escape probability, B_i, is calculated for each i from equation 5.37 integrated over r and μ, so that

$$\beta_i = 1 - \sum_j \alpha_{ij} \tag{5.43}$$

We note that the B_i will play a direct role in the calculation of the emergent flux $F(\nu)$. The emergent flux from a single transition i is simply

$$F_i(\nu) = \bar{q}_\ell A_i B_i \Delta E_i \Phi_i(\nu) \tag{5.44}$$

where ℓ is the upper level of transition i. The only change from equation 5.1a is that A_i has been replaced by $A_i B_i$. However, we must recognize that the level populations $\bar{q}_\ell$ are no longer known, at least for levels which are involved in allowed transitions, since each is in part determined by absorption of photons emitted by other levels. Thus, while it is correct to express the emergent flux as

$$F(\nu) = \sum_\ell \bar{q}_\ell \sum_{i \epsilon \ell} A_i B_i \Delta E_i \Phi_i(\nu) \tag{5.45}$$

the apparent linear superposition of the emission lines from different levels is illusory since the $\bar{q}_\ell$ are coupled together by radiative processes.

In general this coupling can be highly nonlinear since the τ_i, the basic quantities used to calculate the B_i and α_{ij}, themselves depend on level populations (cf equation 5.16). This poses formidable numerical difficulties since the nonlinear system is of high dimensionality. Although such a direct treatment is certainly workable, the situation in the SNI nebula permits a simpler linear treatment to be used. To understand why this is so, it is helpful to examine Figure 5.4a, which shows the result from the standard run at 264d for the level populations of FeI, and compare it with Figure 5.4b, which shows the total radiative decay rates of these levels. The population of levels with significant radiative decay rates are strikingly small in comparison with the "core levels", which have $E \lesssim 1.5$ ev and negligible radiative decay rates. This is largely due to the small values of the temperature, $T \approx 0.5$ ev, relative to the upper energy levels of the allowed lines, which have $E \gtrsim 2.5$ ev. The effect is enhanced by the small values of ϵ for the allowed levels (cf equation 5.22), which causes the core levels to have populations significantly above their LTE values. In this case the allowed level populations in the absence of radiative absorption effects (all $\alpha_{ij} = 0$), which will be denoted as $\tilde{q}^{(0)}$, are accurately determined by

$$A_{T\ell}\, \tilde{q}_\ell^{(0)} = \sum_{j\varepsilon \text{core}} C_{j\ell} \tilde{q}_j^{(0)} \equiv \gamma_\ell \qquad (5.46)$$

where $A_{T\ell}$ is the total radiative decay rate of the allowed level ℓ. The sum on j extends only over the core levels to give γ_ℓ, the total rate of collisional excitation of level ℓ.

Although it is a difficult assumption to justify a priori, we expect that the radiation field will be weak in the sense that the presence of radiative coupling will have an insignificant effect on the population of the core levels. The radiation field may still be strong in the sense that the allowed level populations undergo a large relative change, however. In this case the level populations are determined by linear equations, since the τ_i, and therefore the α_{ij} and B_i, depend only on core level populations which are insignificantly changed from the known values $\tilde{q}_j^{(0)}$. Similarly, the rate of collisional excitation of the allowed levels, γ_ℓ, given by equation 5.46 is unchanged. The linear equations satisfied by the $\tilde{\gamma}_\ell$ are then

$$\tilde{q}_\ell \, A_{T\ell} \quad \ell + \sum_{\ell'} \tilde{q}_{\ell'} \sum_{j\epsilon\ell'} A_j \sum_{i\epsilon\ell} \alpha_{ji} \tag{5.47}$$

where, as previously, the notation $i\epsilon\ell$ indicates summation over all transitions i which have ℓ as their upper level. Defining the quantity

$$C_i = \frac{A_i}{A_{Ti}} \tag{5.48}$$

and making use of equation 5.46, we arrive at

$$\tilde{q}_\ell - \sum_{\ell'} \frac{A_{T\ell'}}{A_{T\ell}} \sum_{j\epsilon\ell'} C_j \sum_{i\epsilon\ell} \alpha_{ji} = \tilde{q}_\ell^{(0)} \tag{5.49}$$

The sum over ℓ' in equations 5.47 and 5.49 includes ℓ, and extends over forbidden as well as allowed levels. For forbidden levels, however, there is no absorption, so that $\tilde{q}_\ell = \tilde{q}_\ell^{(0)}$. The set of equations 5.49 thus need be solved only for the allowed levels, and may be rewritten in the form

$$\tilde{q}_\ell - \sum_{\ell'} \tilde{q}_{\ell'} R_{\ell'\ell} = \tilde{q}_\ell^{(0)} + \sum_{k} \tilde{q}_k^{(0)} R_{k\ell} \tag{5.50}$$

where $$R_{\ell'\ell} = \frac{A_{T\ell'}}{A_{T\ell}} \sum_{j\epsilon\ell'} C_j \sum_{i\epsilon\ell} \alpha_{ji} \tag{5.51}$$

and the summation on the LHS of equation 5.50 extends over allowed levels only, while that on the RHS over forbidden levels only. This system is readily solved with a standard linear solver, and the resulting populations may be used in equation 5.45 to calculate the emergent flux F(v).

At this point it is necessary to inquire whether the assumption that the core level populations are not significantly changed by radiative coupling is valid. We note that while a direct check on the change in these populations can not be made from the solution to equation 5.50, since they remain equal to $\tilde{q}_j^{(0)}$, a breakdown in the assumption will manifest as a failure to conserve population. This arises because upward radiative transitions from core levels increase the populations of the upper levels through equation 5.50, while there is no compensating decrease in the population of the core levels. In fact, the degree of population nonconservation sets an upper limit in the change of any core level population:

$$(\tilde{q}_K^{(0)} - \tilde{q}_K) < \sum_{\ell \epsilon n} (\tilde{q}_\ell - \tilde{q}_\ell^{(0)}) \tag{5.52}$$

Here k denotes any core level of an ion and the sum over ℓ extends over all levels of the ion n. Recalling that the normalization of the $\tilde{q}$ is such that

$$\sum_{\ell \epsilon n} \tilde{q}_\ell^{(0)} = f_n \tag{5.53}$$

we see that the measure of population conservation for the ion n should be

$$\delta = \frac{1}{f_n} \sum_{\ell} (\tilde{q}_\ell - \tilde{q}_\ell^{(0)}) \tag{5.54}$$

We are interested not in the absolute, but the relative change in q_K, and this is bounded by

$$\frac{\tilde{q}_k^{(0)} - \tilde{q}_k}{\tilde{q}_k^{(0)}} < \frac{\delta f_n}{\tilde{q}_k^{(0)}} \tag{5.55}$$

The value of δ from the standard run at 264d is 8×10^{-6} for FeI. On the other hand, from the populations of Figure 5.4, (which are normalized to $f_0 = 1$), we see that for the core levels, $\tilde{q}_k^{(0)} \geq 1 \times 10^{-2}$, so that

$$\frac{\tilde{q}_k^{(0)} - \tilde{q}_k}{\tilde{q}_k^{(0)}} < 10^{-3} \tag{5.56}$$

The assumption that the core level populations are unchanged is thus well justified, especially since the upper limit of 5.56 would be reached only if all the increased population of the allowed levels were removed from a single core level, which is of course

not the case. As we expected, however, the population of allowed levels may undergo large relative changes with

$$\frac{\bar{q}_\ell - \bar{q}_\ell^{(0)}}{\bar{q}_\ell^{(0)}} \approx 10 \tag{5.57}$$

not being uncommon.

As the final step in the calculation of the emergent flux F(ν), we must determine the emergent line profiles $\Phi_i(\nu)$. Including for the moment an arbitrary normalization constant A, and working once again with the geometry of Figure 5.2, we can express $\Phi_i(\nu)$ as

$$\Phi_i(\nu) = A \int_{(1-h)R}^{R} dr\, 4\pi r^2 \int_{-1}^{1} d\mu\, B_i(r,\mu)\, \delta(\nu-\nu_i^*(r,\mu)) \tag{5.58}$$

Here $\nu_i^*(r,\mu)$ is the frequency of a photon emitted by transition i from the point r, in direction μ, as measured by an observer outside the nebula who is at rest with respect to its center of mass. As previously, we apply the Lorentz transform to obtain

$$\begin{aligned} \nu_i^*(r,\mu) &= \nu_i\left(1 + \mu \frac{U(r)}{c}\right) \\ &= \nu_i \left(1 + \mu \frac{r}{R} \frac{U}{c}\right) \end{aligned} \tag{5.59}$$

The delta function in equation 5.58 is justified due to the negligible intrinsic linewidth in comparison to the expansion Doppler shifts. This delta function may be rewritten as

$$\delta(\nu - \nu_i^*(r,\mu)) = \frac{Rc}{rU\nu_i}\ \delta(\mu-\mu^*(r,\nu)) \tag{5.60}$$

where

$$\mu^*(r,\nu) = \frac{Rc}{rU}\left(\frac{\nu - \nu_i}{\nu_i}\right) \tag{5.61}$$

It is convenient to work with the variable

$$x \equiv \frac{c}{U}\left(\frac{\nu - \nu_i}{\nu_i}\right) \tag{5.62}$$

instead of ν. We note that $\Phi_i(x) = 0$ unless $-1 \leq x \leq 1$. Substituting equation 5.61 into 5.58, and transforming to x, we obtain

$$\Phi_i(x) = 4\pi AR \int_{R_{min}}^{R} dr\ r\ B_i(r,\frac{Rx}{\nu}) \tag{5.63}$$

where $\Phi_i(x)dx = \Phi_i(\nu)d\nu$

and $$R_{min} = \text{Max}\left\{(1-h)R,\ |x|\ R\right\} \tag{5.64}$$

which results from requiring $|\mu^*| \leq 1$. The normalization constant, A, is easily determined from equation 5.58 and the requirement that

$$\int_0^\infty \Phi_i(\nu)d\nu = 1 \tag{5.65}$$

Utilizing equations 5.37, 5.38 and 5.43, we find that

$$A = \frac{1}{2VB_i} \tag{5.66}$$

so that

$$\Phi_i(x) = \frac{2\pi R}{VB_i}\int_{R_{min}}^{R_{max}} dr\ r\ B_i(r, \frac{Bx}{r}) \tag{5.67}$$

A final change of variables to $y = \frac{r}{R}$ results in

$$\Phi_i(x) = \frac{3}{2B_i\left(1-(1-h)^3\right)} \int_{\max\left[(1-h),x\right]}^{1} dy\ y\ B_i(yR,\frac{x}{y}) \qquad (5.68)$$

We see that in the simplest case, where $B_i = 1$ and $h = 1$, we obtain

$$\Phi_i(x) = \frac{3}{4}\ (1 - x^2) \qquad (5.69)$$

the familiar parabolic lineshape from a uniformly expanding transparent sphere (cf Mihalas 1978). When absorption is present the line profiles become asymmetric, with the emission peak shifted to the blue. Some example profiles are shown in Figure 5.5 from the standard run at 264d.

The prescription for calculating the emergent flux $F(\nu)$ is now complete:

(1) The quantities $\alpha_{ij}(r,\mu)$ and $B_i(r,\mu)$ are calculated by equations 5.36 and 5.37.

(2) Their average values α_{ij} and B_i are found by numerical integration over r and μ (equations 5.40 and 5.43).

(3) The allowed level populations in the presence of radiative coupling, $\tilde{q}_\ell$, are found from the populations $\tilde{q}_\ell^{(0)}$ and the α_{ij} by solving the linear system 5.50.

(4) The emergent line profiles $\Phi_i(\nu)$ are determined from the $B_i(r, \mu)$ by equations 5.68.

(5) The emergent spectrum is calculated from equation 5.45.

The accuracy of the method is limited only by the assumption that level opulations and the density are independent of r. It is interesting to note the power of the escape probability formalism. When it can be applied, an exact solution to the radiative transfer problem is attained without needing to solve the integral equations which are required in general.

Figure Captions

Fig. 5.1 Optical depths of allowed lines plotted versus wavelength in Angstroms. Results are from the standard numerical run with $\alpha = 0.7$, $U_g = 0.7$, $h = 1$.

a) t = 87d

b) t = 264d

Fig. 5.2 Geometry of photon propagation in the SNI nebula.

Fig. 5.3 Resonance absorption surfaces within the SNI nebula for photons emitted by transition i from point $\vec{r}$ are shown schematically.

Fig. 5.4 Fractional population and radiative rates of FeI levels for the standard run at t = 264d are plotted versus the energy of level in ev.

a. Level population, q, normalized to unity.

b. Radiative decay rate, A (sec^{-1})

Fig. 5.5 A selection of emergent line profiles, $\Phi(x)$, are shown from the standard run at t = 264d. Each profile is labelled by the value of the average escape probability, B.

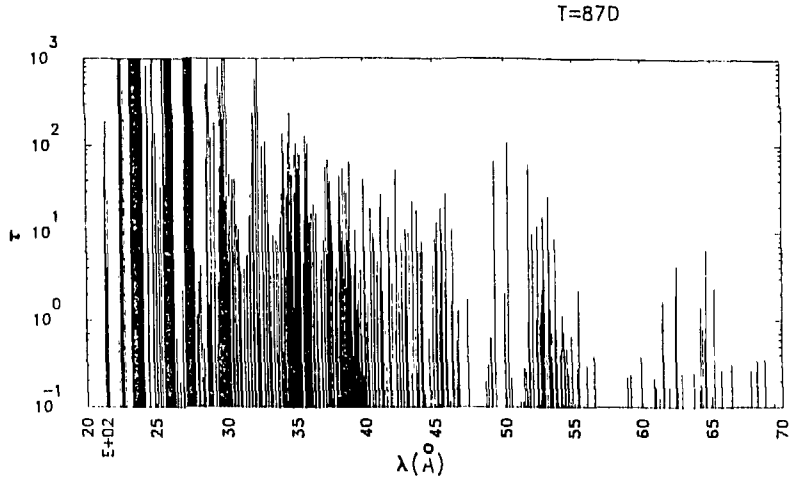

Fig. 5.1a

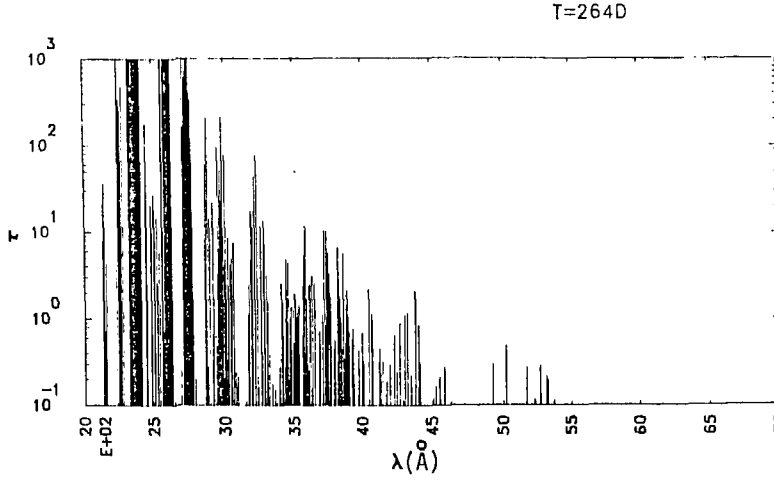

Fig. 5.1b

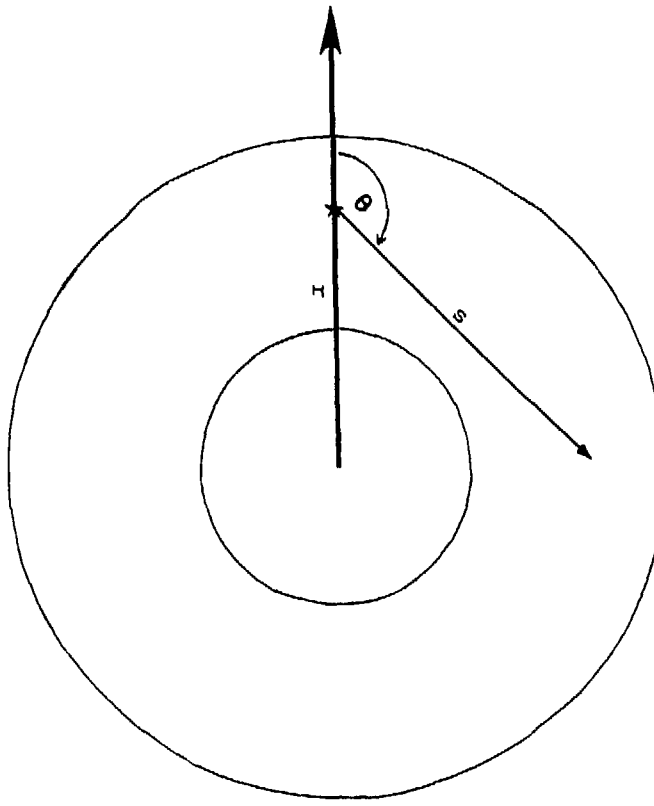

Fig. 5.2

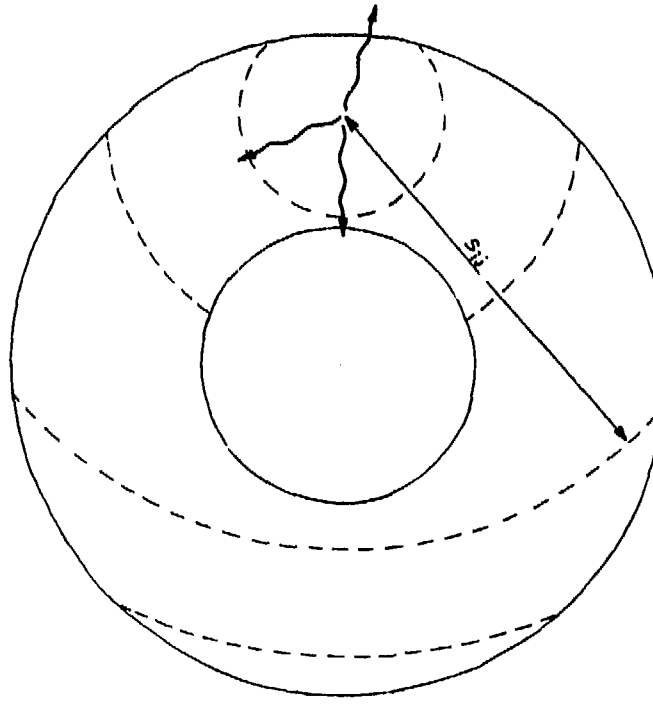

Fig. 5.3

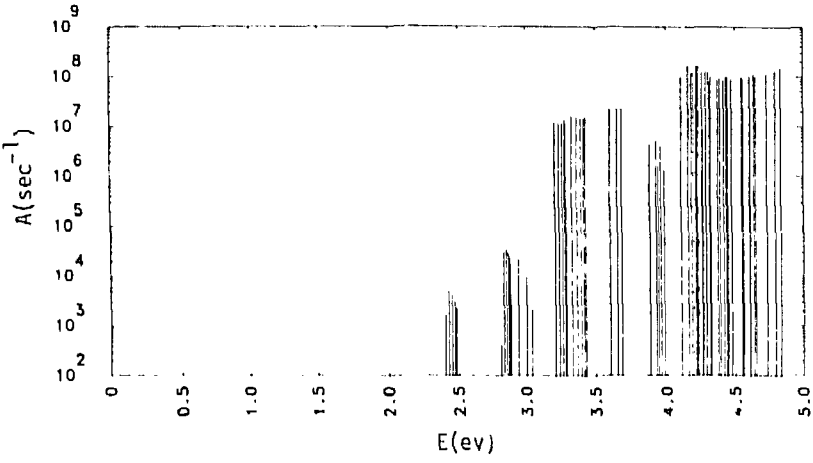

Fig. 5.4b

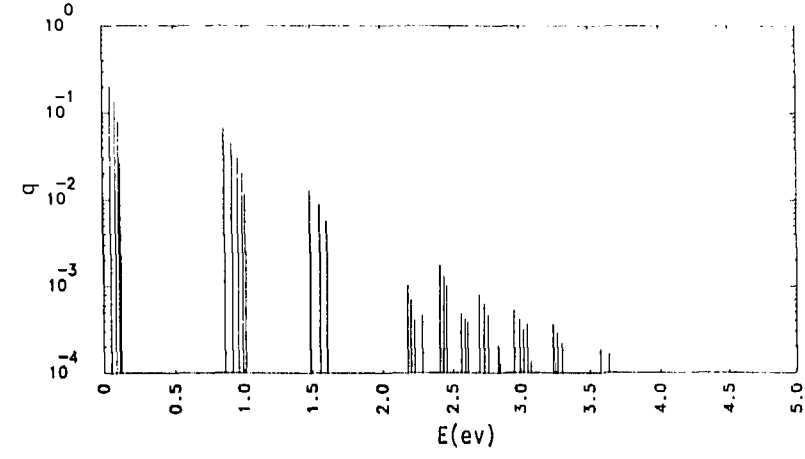

Fig. 5.4a

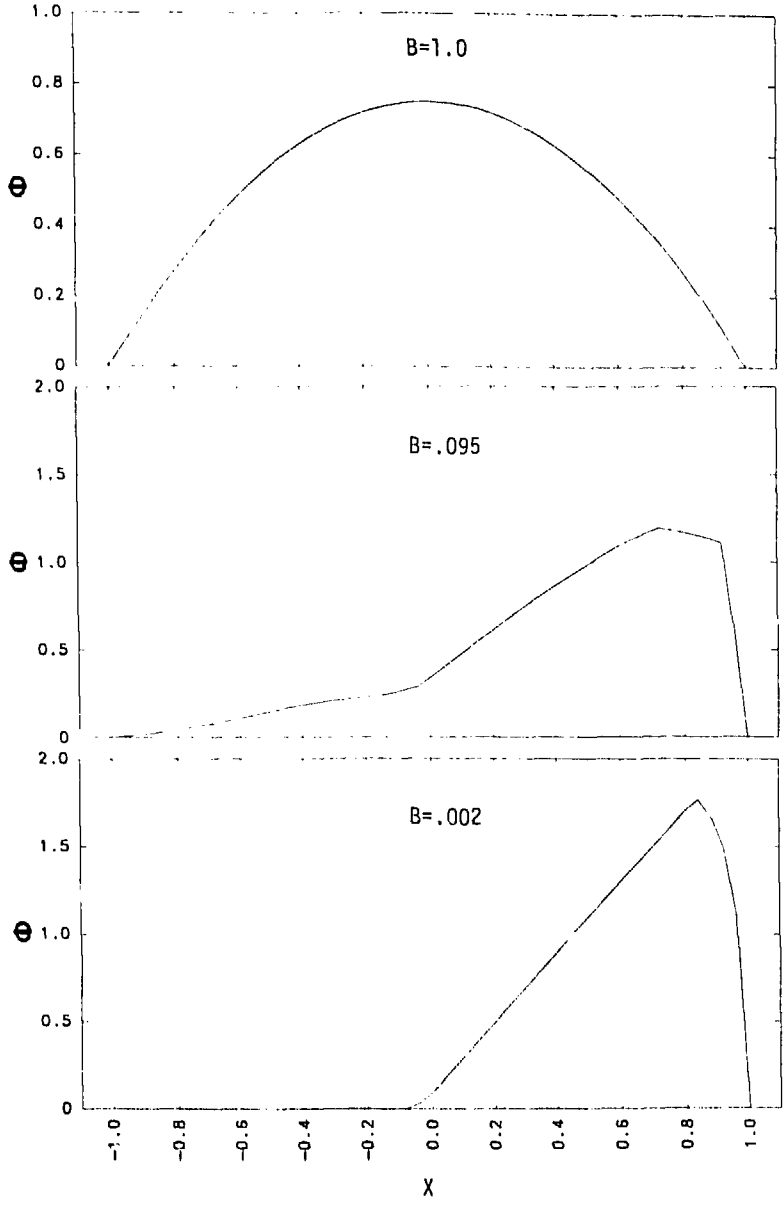
B=1.0
B=.095
B=.002
θ
X
1.0
0.8
0.6
0.4
0.2
0
2.0
1.5
1.0
0.5
-1.0
-0.8
-0.6
-0.4
-0.2
0.0
0.2
0.4
0.6
0.8
1.0

Fig. 5.5

VI. Application to Real SNI: The Optical Light Curve

The results of Section IV allow the relationship of observed SNI light curves to the parameters of the Ni^{56} nebular model to be determined, an issue which has previously been addressed by Colgate et al (1980) and Arnett (1979). As long as the temperature of the nebula remains well above T_c, so that the infrared luminosity is negligible, the bolometric luminosity in the optical region, L_{OPT}, is simply

$$L_{OPT}(t) = \mathcal{N} \mathbf{S}_{elec}(t) \tag{6.1}$$

where $\mathcal{N}$ is the total number of atoms in the nebula,

$$\mathcal{N} = 2.15 \times 10^{55} \mathcal{M} \tag{6.2}$$

As shown in IV, the heating efficiency, η, is very close to unity, so that $\mathbf{S}_{elec}$ in equation 6.1 may be replaced by $\mathbf{S}_{co}$ with negligible error. Utilizing equation 3.11 for $\mathbf{S}_{co}(t)$, we obtain

$$L_{OPT}(t) = 1.25 \times 10^{43} \mathcal{M} e^{-t/114} \left(.035 + D(pR)\right) \quad \text{erg/sec} \tag{6.3}$$

where D(pR) is the gamma deposition function given by equation 3.4, and it is assumed that $t >> \tau_{Ni}$ (8.8d). As shown in III, for $t \gtrsim 50 \sqrt{\mathcal{M}}/U_g$ days, D has the simple form

$$D(t) \approx 1.3 \times 10^3 \frac{\mathcal{M}}{(U_9 t)^2} \tag{6.4}$$

so that equation 6.3 becomes

$$L_{OPT}(t) \approx 4.38 \times 10^{41} \mathcal{M} e^{-t/114} \left(1 + \frac{3.7 \times 10^4 \mathcal{M}}{(U_9 t)^2}\right) \text{erg/sec} \tag{6.5}$$

In principle, if $L_{OPT}(t)$ were known during the nebular phase, equation 6.5 could be used to determine $\mathcal{M}$ and U_9. In particular, when $t >> 200\sqrt{\mathcal{M}}/U_9$ days, L_{OPT} becomes independent of U_9, so that $\mathcal{M}$ may be simply determined.

Several complications arise which limit the amount of information which may be derived from this approach. The least serious of these arise from the limited range of time in which equation 6.1 is valid. At early times the nebular model fails since the optical depth of the star is still large, and a photospheric surface exists. As discussed in II, the photospheric phase does not end until $t \approx 80\sqrt{\mathcal{M}}/U_9$ days. In spite of the breakdown of the nebular model, however, equation 6.1 may remain approximately valid even near maximum light ($t \approx 20$) for initially compact models in which the initial energy of the explosion is rapidly lost to adiabatic expansion. Colgate et al (1980) and Weaver et al (1980) have considered models of this type. On the other hand, for initially extended models, such as those discussed by Lasher (1975), the

luminosity near maximum light is due to the diffusive release of internal energy remaining from the explosion, so that equation 6.1 does not become valid until the photospheric era ends. Additional uncertainty arises at early times from the dependence of the effective gamma opacity on the density profile of the star and the spatial distribution of Ni^{56} within it (cf IIIA).

At sufficiently late times, as discussed in IV, new difficulties arise due to the breakdown of the steady state approximation and the occurrence of the IRC. For the moment we will assume that these effects do not become important until $t \gtrsim 500d$ and defer the discussion of this part of the light curve to the end of this section.

The most serious limitation on the accuracy of $\mathcal{M}$ and U_9 as determined from the light curve and equation 6.5 comes from the difficulty of determining $L_{OPT}(t)$ from the available SNI observations. Several different approaches are possible. In most cases the quantity determined is not L_{OPT} but rather M_B, the absolute blue magnitude, the two being related by

$$L_{OPT} = 2.97 \times 10^{35} \times 10^{-\left(\frac{M_B + BC}{2.5}\right)} \quad \text{erg/sec} \qquad (6.6)$$

where $BC < 0$ is the bolometric correction. M_B, which will henceforth designate the value at maximum luminosity, may be determined

from the redshift - magnitude diagram for SNI and H_o, Hubble's constant (Kowal 1968; Branch and Bettis 1978). Kowal determined[1]

$$M_B = -18.2 \pm 0.6 + 5 \log (H_o/100) \tag{6.7}$$

The more recent analysis by Branch and Bettis, in which only SNI in elliptical galaxies were considered, so that errors due to reddening in the parent galaxy are reduced, concluded that

$$M_B = -18.18 \pm 0.19 + 5 \log (H_o/100) \tag{6.8}$$

in excellent agreement with Kowal. If $50 \leq H_o \leq 100$, we see that

$$-19.7 \lesssim M_B \lesssim -18.2 \tag{6.9}$$

A second approach is related to Baade's (1926) method for variable stars, and has recently been applied to SNI by Branch (1979). In this approach, which has the virtue of being independent of H_o, the SNI near maximum light is assumed to be adequately represented as an expanding blackbody radiator with temperature $T_{eff}(t)$ and

---

(1) The relation $M_B = M_{PG} + 0.4$ (Branch and Bettis 1978) for an SNI at maximum luminosity has been used to convert Kowals result for M_{PG} to the given expression for M_B.

radius R(t). For a blackbody there is a unique relation between T_{eff} and the color index B-V, allowing M_B to be expressed as

$$M_B = - 5 \log (R/R_\odot) + f_B(B-V) \tag{6.10}$$

The photospheric radius R(t) may be determined by integrating the photospheric velocity $U_{ph}(t)$, which is found from measurements of spectral lines to have the constant value (Branch 1979)

$$U_{ph} \approx 1.1 \times 10^9 \text{ cm/sec} \tag{6.11}$$

In conjunction with the composite SNI color curves of Barbon et al (1973), this yields a value for M_B, which Branch found to be

$$M_B \approx - 19.6 \tag{6.12}$$

As Branch has discussed, it is difficult to assess the uncertainty in this determination of M_B, since there are many sources of error. The most serious errors are introduced by the departure of the actual SNI spectrum from the assumed blackbody. Attempts to fit blackbodies to actual SNI spectra (e.g. Kirshner et al 1973a, Kirshner et al 1976, Weaver et al 1980) indicate that the uncertainties in the resulting value of T_{eff} are large even near maximum light. One reason for this was discussed in V. The value of T_{eff} is constrained only to the approximate range

$$10000 \leq T_{eff} \leq 15000 \ ^{\circ}K \tag{6.13}$$

With $R = U_{ph} \times t_o \approx 1.4 \times 10^{15}$ cm, where $t_o \approx 15d$ is the time of peak luminosity, this results in

$$L_{OPT} = 4\pi R^2 \sigma T_{eff}^4$$

$$\approx 4(\pm 3) \times 10^{43} \quad \text{erg/sec} \tag{6.14}$$

with a corresponding range of M_B of

$$-20.5 \lesssim M_B \lesssim -18.3 \tag{6.15}$$

where a bolometric correction of 0.5 mag, appropriate to $T_{eff} \approx$ 10000 °K (Allen 1973) has been applied to obtain M_B. The actual uncertainties are probably somewhat larger than stated in 6.14, since errors in the determination of R have not been considered. It is, however, reassuring that the M_B values obtained from two quite different techniques are in rough agreement.

With a value for M_B in hand, it is now possible to determine $L_{OPT}(t)$ during the nebular phase by using the observed B light curves of SNI in conjunction with equation 6.6. Further errors are introduced, however, due to the fact that the proper value of BC is not known for the nebular phase, during which the SNI spectrum bears little resemblance to a blackbody. As a result, the usefulness of relation 6.5 for setting limits on $\mathcal{M}$ seems quite small.

Clearly the most desirable method of obtaining the SNI luminosity is to integrate the observed flux $F_\nu(erg/cm^2/sec/H_z)$ over frequency for an SNI whose distance is reliably known. Currently SN1972e in NGC5253 is the only SNI for which F_ν has been measured during the nebular phase (Lee et al 1972; Kirshner et al 1973a; Kirshner et al 1973b; Holm et al 1974; Kirshner and Oke 1975). The measurements extend (with varying accuracy and spectral resolution) from $\lambda = 2.2\mu$ to $\lambda = .14\mu$ near maximum light and from $\lambda = 1\mu$ to $\lambda = .35\mu$ during the nebular phase, so that an accurate determination of L_{OPT} should be possible. The only serious uncertainty arises from the determination of the distance D to NGC5253. Although de Vaucouleurs (1979) has recently determined D = 2.0 ± 0.4 Mpc, this result is entirely dependent on the value of H_o, which is taken to be 102 ± 7.5, and is used to determine the distance from the redshift and from the apparent magnitudes of two SNI by the use of equation 6.7. Since the value of H_o is still in considerable dispute (e.g. Sandage and Tammann 1975; de Vaucouleurs 1977), with there being agreement only that $50 \lesssim H_o \lesssim 100$, it seems necessary to admit greater uncertainty in the value of D. The range adopted here is

$$2 \lesssim D \lesssim 4 \text{ Mpc} \qquad (6.16)$$

This larger average distance is consistent with distance determinations for NGC5253 which do not rely on absolute magnitudes of SNI

(Sersic 1972) and is comparable with the average distance of the members of the Centaurus group (de Vaucouleurs 1979) of which NGC5253 is evidently a member.

The optical flux F_ν measured by Kirshner et al (1973b) and Kirshner and Oke (1975) for SN1972e have been digitized and numerically integrated over frequency to form the optical luminosity by the relation

$$L_{OPT}(t) = 4\pi D^2 \int F(\nu) R(\nu, E_{BV}) d\nu \tag{6.17}$$

where the function R removes the effects of interstellar reddening, assumed to be given by the form (Bless and Savage 1972; Whitford 1958)

$$R(\nu, E_{BV}) = e^{-\left[\frac{E_{BV}}{1.086} \frac{(\nu - \nu_R)}{(\nu_B - \nu_V)}\right]} \tag{6.18}$$

where ν_R = c/10000 Å, ν_V = c/4785 Å, ν_B = c/4167 Å.

The color excess E_{BV} has been taken to be 0.22 mag (Holm et al 1974) which results in roughly a factor of two increase in L_{OPT} over the value obtained with E_{BV} = 0. This procedure has been carried out for all reported spectra, which extend from Julian Day 2441453 to 2442163. The values obtained are listed in Table 3 for D = 4 Mpc.

For the purpose of comparing these values with those predicted by equation 6.5, it is necessary to determine the time of explosion, since this is the t = 0 point for all calculations in this paper. Observations of SN1972e did not begin until a few days after maximum light, so the time of explosion is necessarily uncertain. The date of maximum light may be determined accurately by extrapolation of the photometric oberservations, since SNI exhibit quite uniform behavior near maximum. This has been carried out by Ardeberg and de Groot (1973; 1974), who determined that the B-maximum occurred on Julian Day 2441438 ± 2. The date of explosion is less certain but a prediscovery plate taken on Julian Day 2441423 indicates the luminosity was at least 6 mag below maximum (Ardeberg and de Groot 1973). This combined with the rising branch of the composite SNI light curve (Barbon et al 1973), allows the date of explosion to be estimated, as Julian Day 2441420 ± 5.

Let us now estimate the mass $\mathcal{M}$ from equation 6.5 and the measured luminosity of SN1972e. Equation 6.5 may be solved for $\mathcal{M}$ as

$$\mathcal{M} = \frac{(U_g t)^2}{7.40 \times 10^4} \left[\sqrt{1 + \frac{L_{OPT}(t)}{2.96 \times 10^{36}\, e^{-t/114} (U_g t)^2}} - 1 \right] \qquad (6.19)$$

If we choose the measurement at Julian Day 1441684 (t = 264d), where $L_{OPT} = 9.65 \times 10^{40} (D/4)^2$ erg/sec, we find that

$$\mathcal{M} = 0.94\ U_9^2 \left[\sqrt{1 + \frac{4.74}{U_9^2}\left(\frac{D}{4}\right)^2} - 1 \right] \qquad (6.20)$$

As shown in Table 4, this results in $0.4 \lesssim \mathcal{M} \lesssim 1.4$ for $.5 \lesssim U_9 \lesssim 1.0$ and $2 \lesssim D \lesssim 4$.

To investigate how good a fit to the overall light curve results from this procedure, $L_{OPT}(t)$ has been calculated from equation 6.3 with the source rate from Ni^{56} decay included, so that the source rate is correct even near maximum light. These results are plotted in Figures 6.1 for a sampling of parameters from Table 4, along with the SN1972e observed luminosities. The luminosities due to gamma and positron deposition alone are also plotted to show their relative importance.

Bearing in mind the time restriction on the validity of the calculated luminosity, it is evident that most of the cases shown provide an acceptable fit to the light curve. Low velocities ($U_9 \lesssim .8$) result in a somewhat better fit than high velocities ($U_9 \lesssim 1.0$) but the choice is not compelling. As expected, the calculations fall below the observations during the photospheric phase, when the release of internal energy remaining from the explosion and gamma deposition in the atmosphere are expected to contribute substantially to the luminosity. At late times ($t \gtrsim 400d$), the calculations all fall above the observations, as would be expected if the infrared luminosity is becoming significant. Uncertainties in the time of explosion and the effect of changing the reference point for

performing the fit add an additional uncertainty to $\mathcal{M}(U_9,D)$ from equation 6.20 of about ± 0.2, but do not change the nature of the calculated light curve in a significant way.

We must now consider the late time light curve ($t \gtrsim 400d$), and in particular the role of the IRC in its formation. In section IV it was concluded that at late times, when the electron density N_e satisfies $N_e \lesssim 10^6$ cm^{-3}, the cooling function Λ becomes independent of N_e, so that the temperature is determined from

$$\Lambda(T) = \frac{\mathcal{S}_{elec}(t)}{N_e} \tag{6.21}$$

Due to the existence of the infrared fine structure transitions in the ground terms of nearly neutral iron, a sharp transition occurs near the critical temperature T_c, in which the fraction of the nebular luminosity radiated in the infrared increases from a negligible value above T_c to nearly unity below T_c. If we define

$$\Lambda_c = \Lambda(T_c) \tag{6.22}$$

then the condition for the IRC becomes

$$N_e > \frac{\mathcal{S}_{elec}(t)}{\Lambda_c} \tag{6.23}$$

In a nebula with a density gradient, as we expect to be the case for a real SNI, in general some fraction will satisfy the IRC condition, and therefore be invisible in the optical, while the remainder will radiate in the optical as we have previously assumed. Since S_{co} decreases exponentially with t, while N_e decreases roughly as $1/t^3$, it is clear that this fraction must increase with time. If N_e decreases monotonically with radius, the IRC will occur first at the center of the nebula and sweep progressively outward with time, so that the shape of the density profile is reflected in the time history of the optical luminosity.

An approximate form for $L_{OPT}(t)$ at late times may readily be derived from equation 6.23 and an assumed form for the density profile. The density profile adopted is that used by Colgate and McKee (1969) in thier study of early supernova luminosity, which is given by

$$N(F) = -\frac{\mathcal{N}}{4\pi\alpha(Ut)^3} F^{3\alpha+1} \tag{6.24}$$

where F is the external mass fraction related to N(r) by

$$F(r) = \frac{1}{\mathcal{N}} \int_r^\infty 4\pi r^2 N(r) dr \tag{6.25}$$

and α is a constant roughly equal to 0.25. Equation 6.23 may be used to define the critical density N_c as

$$N_c = \frac{S_{elec}(t)}{\chi \Lambda_c} \tag{6.26}$$

which may be expressed in terms of F by using equation 6.24 as

$$F_c = \left[\frac{4\pi\alpha(Ut)^3}{\mathcal{N}} \frac{S_{elec}(t)}{\chi \Lambda_c} \right]^{1/(3\alpha+1)} \tag{6.27}$$

Although the average ionization, χ, varies with position in the nebula due to the variation in N, results from the numerical model constructed in IV show that χ at the IRC always has the value $\chi_c \approx 2.2 \pm 0.2$ (cf Figure 4.3) so that it may be taken as constant in equation 6.27. The value of Λ_c is found to be approximately 4×10^{-21} erg cm^3 sec^{-1}. We note that if the IRC is idealized as a discontinuity, F_c is simply the mass fraction which is ouside the discontinuity and continues to radiate in the optical. The optical luminosity is then obtained by multiplying equation 6.1 by F_c, so that

$$L_{OPT}(t) = F_c(t) \mathcal{N} S_{elec}(t) \tag{6.28}$$

Equation 6.27 clearly has meaning only if $F_c \leq 1$, and this restriction defines the time, t_c, at which the IRC first occurs. Taking $\mathcal{S}_{elec}$ as that due to positrons only (equation 3.12) and substituting numerical values in equation 6.27, we obtain

$$F_c(t) \approx \left[\frac{4.4 \times 10^{-6}\, \alpha (U_9 t)^3\, e^{-t/114}}{\mathcal{M}} \right]^{1/(3\alpha+1)}$$

and t_c is defined by

$$t_c^3\, e^{-t_c/114} = 2.3 \times 10^5\, \frac{\mathcal{M}}{U_9^3} \qquad (6.30)$$

Taking $\alpha = 0.25$, this results in $t_c \approx 425$d if $\mathcal{M}/U_9^3 = 2$ and $t_c \approx 650$d if $\mathcal{M} / U_9^3 = 0.5$. If $\mathcal{M}/U_9^3 > 2.2$ there is no solution to equation 6.30 for t_c. This does not mean that the IRC begins at $t = 0$, but simply indicates the breakdown of the approximation that Λ is density independent. Numerical calculations with the complete model of Section IV show that $t_c \gtrsim 400$d for all values of $\mathcal{M}$ and U_9 in Table 4.

It is intriguing to note that at late times the optical luminosity predicted by equations 6.28 and 6.29 has the time dependence

$$L_{OPT}(t) \propto t^{3/(3\alpha+1)} e^{-t/\tau_{eff}} \tag{6.31}$$

where

$$\tau_{eff} = \left(\frac{3\alpha + 1}{3\alpha + 2}\right) \tau_{Co} \tag{6.32}$$

For $\alpha = 0.25$, $\tau_{eff} = 75d$, close to the observed decay rate of the late time SNI luminosity (Mihalas 1963). This asymptotic behavior is confirmed by Figure 6.2, which shows the light curve which results from $U_9 = .7$, $\mathcal{M} = .7$, D = 3Mpc, and the model of Section IV. It must, however, be reemphasized that the validity of the solution is uncertain for t > 500d, where the steady state approximation fails.

The results of this section are summarized by Figure 6.3, which shows the region in the parameter space defined by $\mathcal{M}$ and U_9 which results in an acceptable fit to the observed SN1972e lightcurve. Most of the uncertainty in $\mathcal{M}$ results from the lack of knowledge of the distance ot NGC5253, or equivalently, of the absolute magnitude of SNI at maximum. Although results for the lightcurve beyond 500 days are uncertain, it is clear that the progression of the IRC through the nebula plays an important role in determining the slope of the lightcurve at late times. As will be seen in the following section, the optical spectra of SN1972e offer some support for this view.

TABLE 3

Bolometric Luminosity of SN1972e at D = 4Mpc

Julian Day	L (erg/sec)
2441453	1.87×10^{43}
454	2.30×10^{43}
455	2.46×10^{43}
458	1.63×10^{43}
460	1.16×10^{43}
461	1.00×10^{43}
469	7.69×10^{42}
472	8.41×10^{42}
475	6.55×10^{42}
484	3.50×10^{42}
493	2.28×10^{42}
504	3.07×10^{42}
507	1.96×10^{42}
529	1.01×10^{42}
653	1.40×10^{41}
684	9.05×10^{40}
796	2.18×10^{40}
865	9.68×10^{39}
2442163	1.55×10^{38}

Table 4

Value of $\mathcal{M}$ Required to Produce Observed Optical Luminosity of SN1972e at Julian Day 2441684 (t = 264d)

$\mathcal{M}$ is Ni^{56} mass ($M_\odot$)

D is distance to NGC5253 (Mpc)

U_9 is expansion velocity (10^9 cm sec^{-1})

U_9	D = 2	D = 3	D = 4
0.5	0.32	0.55	0.79
0.7	0.38	0.69	1.02
0.9	0.43	0.80	1.20
1.1	0.46	0.88	1.35
1.5	0.49	1.00	1.58

Figure Captions

Fig. 6.1 Calculated light curves are compared with the observed light curve of SN1972e for a sampling of parameters from Table 4. Observed SN1972e bolometric luminosities are labelled by "*". The model light curve is shown by the unlabelled solid line, while the lines labelled by "G" and "P" show the contributions from gamma deposition and positron deposition, respectively. Each graph is labelled by the Ni^{56} mass, $\mathcal{M}$, expansion velocity, U_g, and assumed distance to NGC5253, D.

Fig. 6.2 Same format as Fig. 6.1, except that a power law density profile with $\alpha = 0.25$, as discussed in the text, has been assumed to illustrate the effect of the IRC on the late-time light curve.

Fig. 6.3 Limits on $\mathcal{M}$ and U_g imposed by the SN1972e light curve. Solid lines show relation between $\mathcal{M}$ and U_g resulting from the requirement that the optical luminosity of the model equal that of SN1972e at t = 264 d for the indicated distance, D, to NCG5253. Hatched area indicates acceptable values of $\mathcal{M}$ and U_g, as discussed in the text.

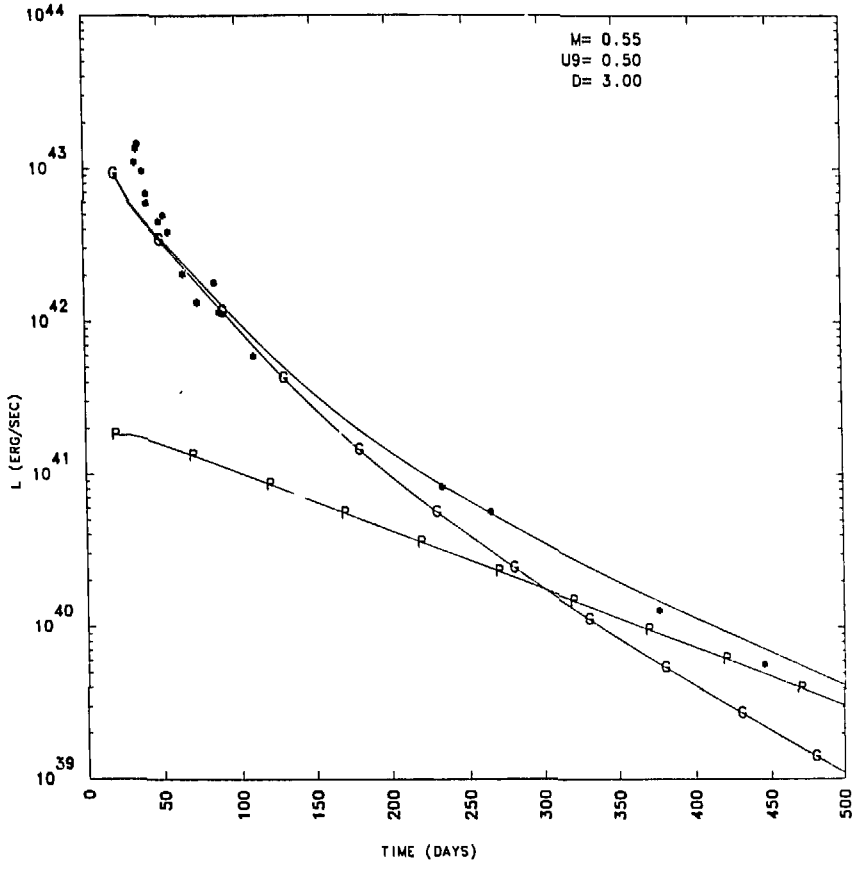
M= 0.55
U9= 0.50
D= 3.00
L (ERG/SEC)
TIME (DAYS)
10^44
10^43
10^42
10^41
10^40
10^39
0
50
100
150
200
250
300
350
400
450
500
G
P

Fig. 6.1

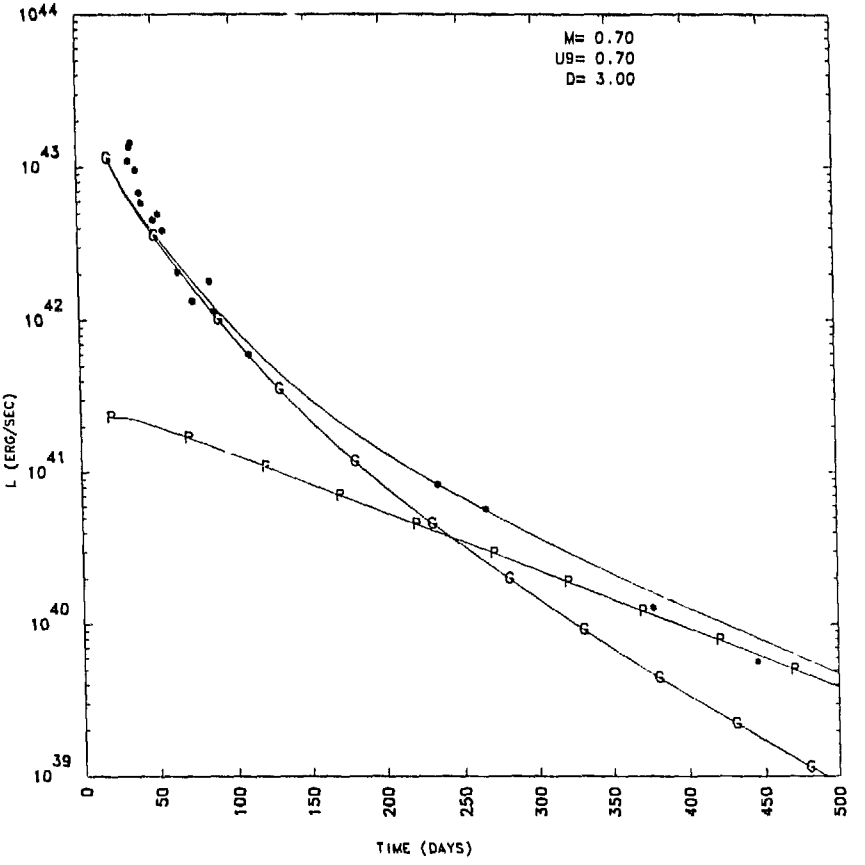

Fig. 6.1 (cont.)

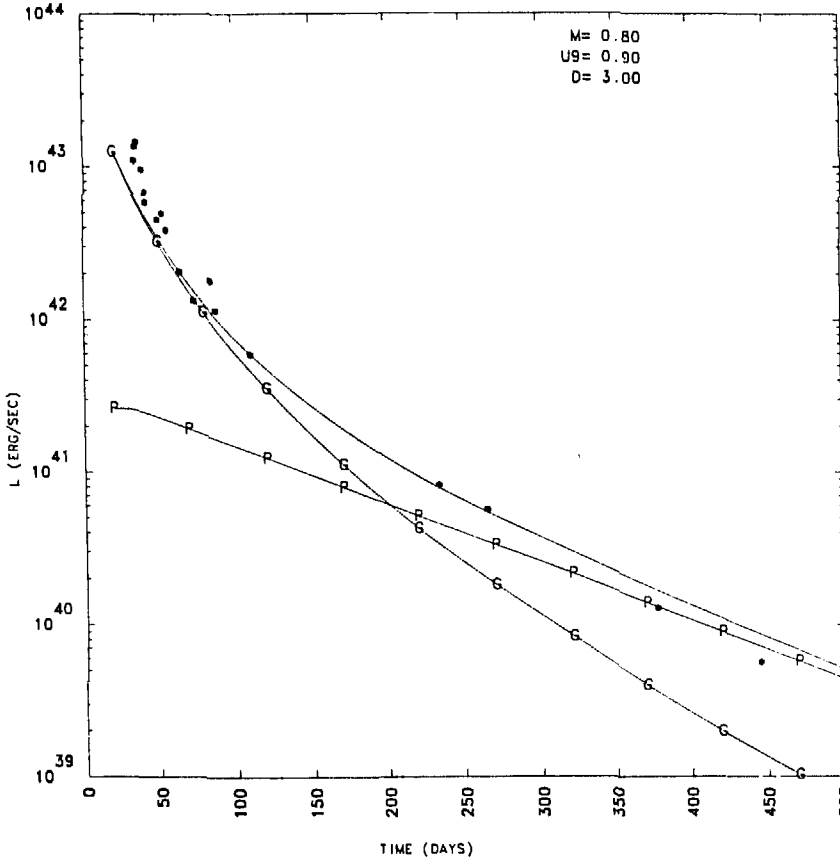

Fig. 6.1 (cont.)

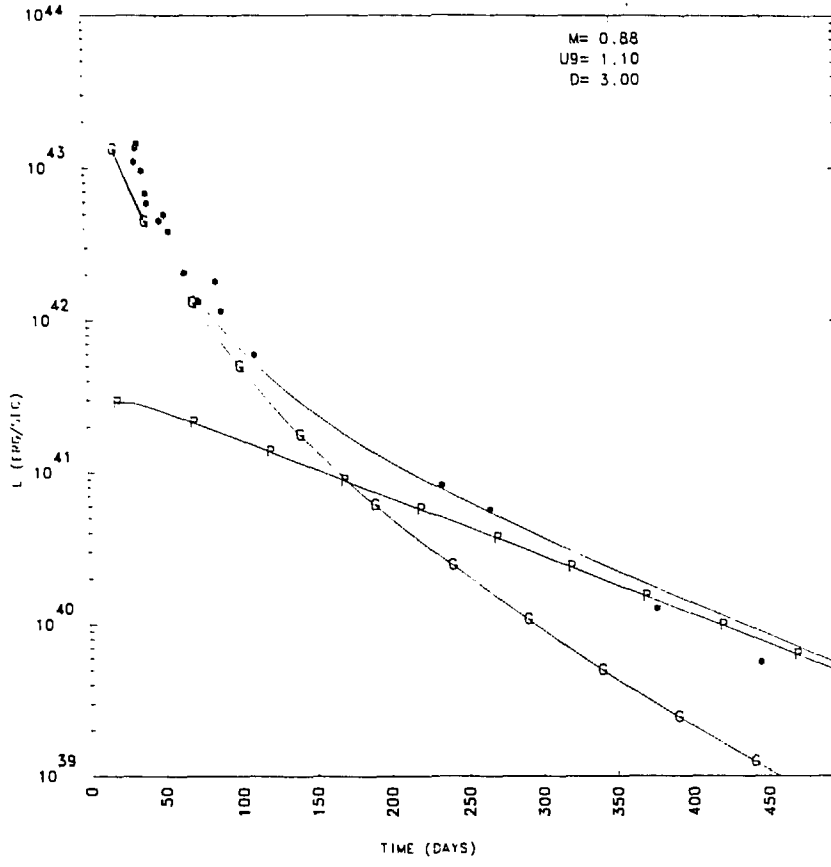
M= 0.88
U9= 1.10
D= 3.00
10^{44}
10^{43}
10^{42}
10^{41}
10^{40}
10^{39}
L (ergs/sec)
0
50
100
150
200
250
300
350
400
450
500
TIME (DAYS)

Fig. 6.1 (cont.)

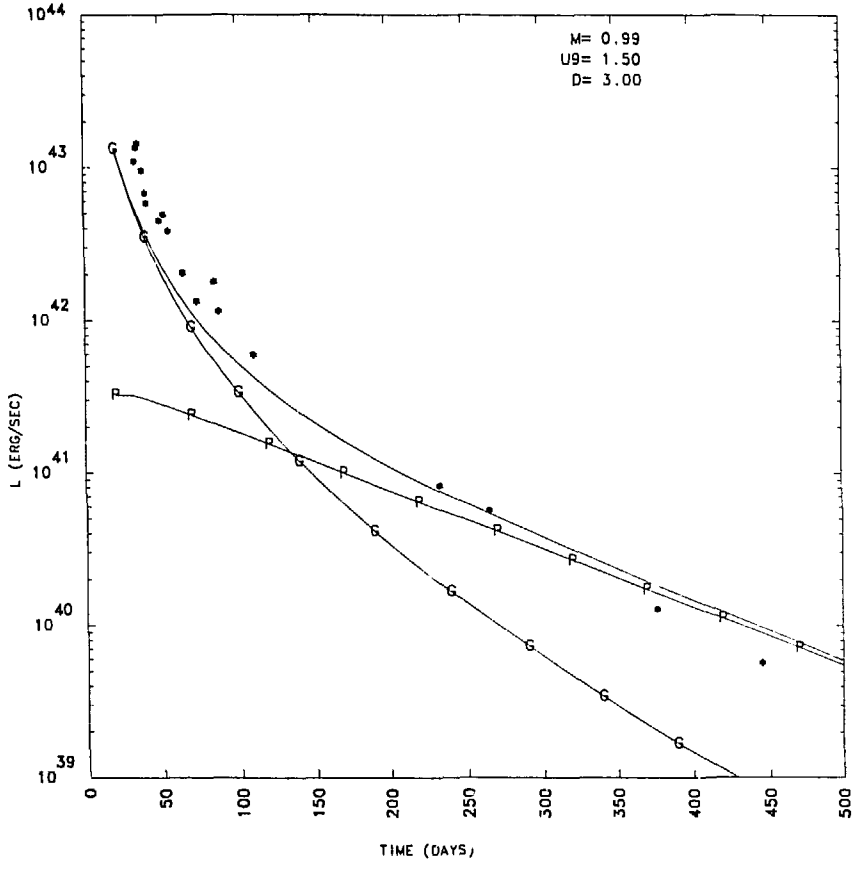
M= 0.99
U9= 1.50
D= 3.00
L (ERG/SEC)
TIME (DAYS)
10^44
10^43
10^42
10^41
10^40
10^39
0
50
100
150
200
250
300
350
400
450
500
G
P

Fig. 6.1 (cont.)

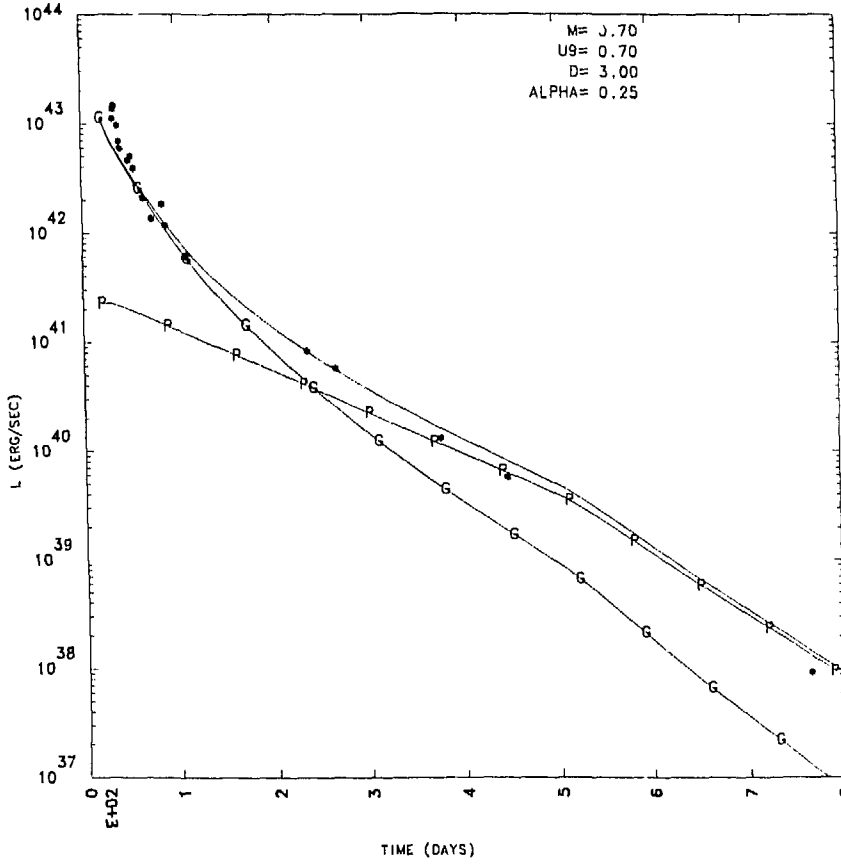

Fig. 6.2

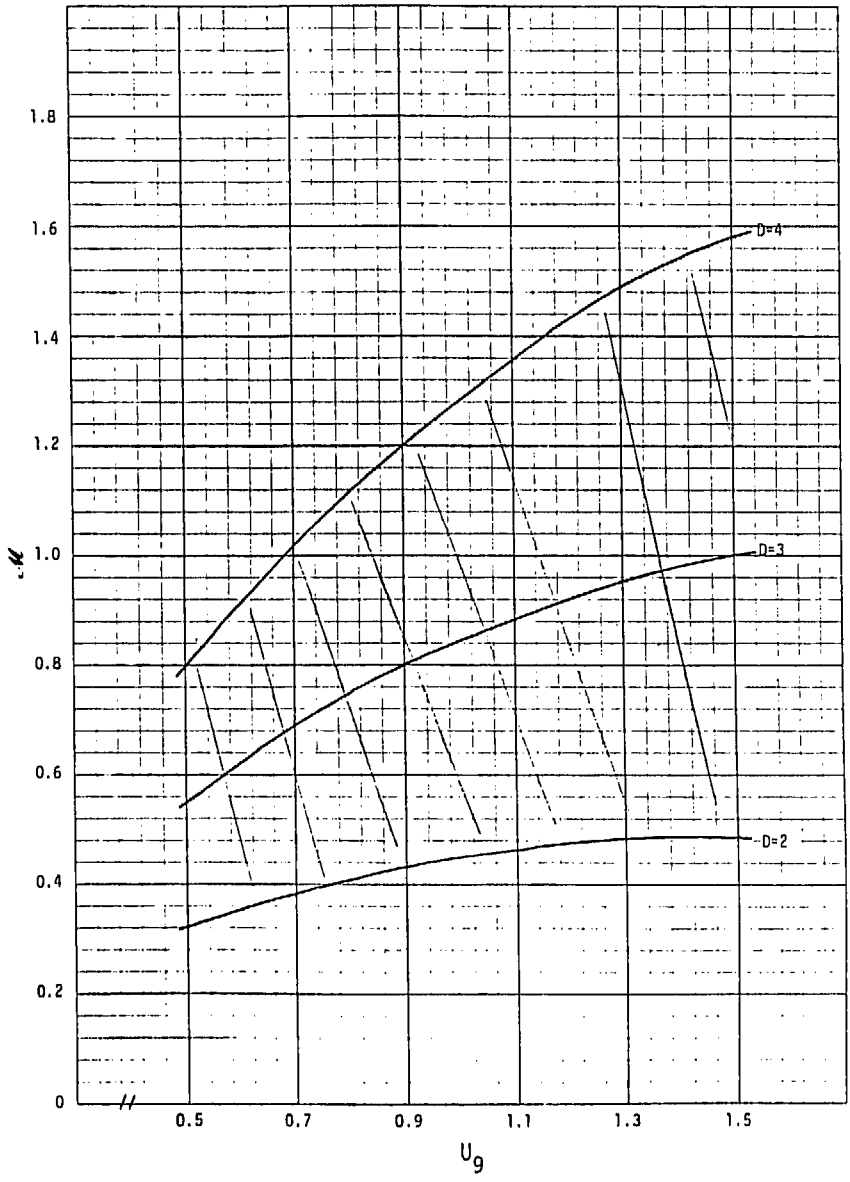

Fig. 6.3

VII. Application To Real SNI: The Optical Spectrum of SN1972e

We must now inquire whether the model for the nebular phase of SNI developed in the previous sections is capable of generating optical spectra in agreement with observations. As discussed in Section VI, at present only a single SNI, SN1972e, has been sufficiently well observed during the nebular phase that such a test is possible. The uniformity of SNI light curves and optical spectra near maximum light, however, offers considerable hope that the conclusions reached will be generally applicable to SNI. In particular, if the presence of Co can be confirmed in the optical spectra with an abundance decaying at the expected rate for Co^{56}, the Ni^{56} hypothesis will have passed a key test.

Following a similar strategy as was employed in Section VI to match the model light curve to observations, one of the observed SN1972e spectra (Kirshner et al 1973b; Kirshner and Oke 1975) is chosen as a reference, and the nebular parameters varied to find the best agreement between the calculated and reference spectra. The resulting set of parameters is then used to compare the model with observations at earlier and later times than the reference, so that the accuracy of the time evolution of the model spectrum can be checked. We expect that the model will generate reasonably accurate spectra only within a limited time interval, and it is of great interest to determine where the boundaries of this interval in fact occur.

The analysis of section IV makes it clear that the emergent spectrum will be determined principally by the nebular density parameter, Δ(cf equation 4.15), since the ionization state, temperature, and level populations are all controlled by it. In addition the spectrum is affected directly by the expansion velocity, U_9, since it determines the width of spectral features through the lineshapes calculated in section VI. We note that if Δ and U_9 can be determined by requiring agreement between the calculated and observed spectra, the relation between $\mathcal{M}$ and U_9 determined in Section VI (cf equation 6.20) from analysis of the light curve in principle supplies sufficient information to determine the nebular parameters $\mathcal{M}$, U_9, and h uniquely. Unfortunately there are several sources of uncertainty which currently prevent such a unique determination. As discussed in previous sections, these arise both for atomic physics quantities, such as the recycling fraction, ϕ_R, and for astronomical quantities, such as the distance to NGC5253. For the moment all these quantities will be assumed fixed at the following nominal values:

E_{BV} =	0.22 mag	(Color excess from interstellar reddening)
D =	3.0 Mpc	(Distance to NGC5253)
A =	$1.33 \times 10^{-14} cm^2 ev^2$	(Collisional ionization crossection parameter (cf eqn. 3.38)

ω =	.03	(Collision strength multiplier cf eqn. 4.47)
Φ_R =	0.6	(Recycling fraction cf eqn. 4.19)
α_{rec} =	$3.0 \times 10^{-13} cm^3/sec$	(Recombination coefficient cf. eqn. 4.23)

The spectrum observed on Julian Day 2441684 has been chosen as the reference. The time of explosion is assumed to be Julian Day 2441420, so the reference time is t = 264d. The calculated spectra have been reddened according to equation 6.18 and averaged over wavelength to simulate the reported spectral resolution of the multichannel spectrometer used in the observations (Oke 1969; Kirshner and Oke 1975). The Cobalt abundance is set to 0.10, as given by equation 3.1 for t = 264d. The energy deposition rate is ε_{Co} from equation 3.11, the same as used for the light curve calculation of Section VI.

Systematic variation of the nebular parameters has led to the choice

$$\begin{aligned} \mathcal{M} &= 0.7 \\ U_9 &= 0.7 \\ h &= 1.0 \end{aligned} \qquad (7.1)$$

for the best fit to the reference spectrum. These will be referred to as the "standard parameters". The calculated spectrum resulting from these parameters at t = 264d is shown in Figure 7.1 along with

the SN1972e reference spectrum. The light curve resulting from this choice of parameters was previously presented in Figure 6.1. For the purpose of comparing the calculated and observed reference spectra, the normalization error resulting from the discrepancy between the observed and calculated optical luminosities has been removed in Figure 7.1 and in the following figures. The nebular density parameter is $\Delta = 0.5$. The temperature and ionization state are listed in Table 5, while the contribution to the total spectrum of each ion individually is shown in Figures 7.2 a-f.

A. Comparison of Calculated and Observed Spectra

The agreement between the calculated and observed spectra is, on the whole, strikingly good. There are also, however, numerous discrepancies. How is the significance of these discrepancies to be assessed? We must attempt to decide whether they arise from the limitations of the model and inaccuracies in the atomic data, or from a basic lack of applicability of the model to SNI. A definitive answer to this question is of course not possible, at least without construction of a model which is free of the limitations in question! Considerable progress may be made, however, by comparing the evolution with time of the model spectra and the observed spectra.

A series of comparisons between calculated and observed spectra is presented in Figures 7.3 a-f beginning with Julian Day 2441507 (t = 87d) and extending to the observation on Julian Day

2441865 (t = 445d). No comparison is shown for the last observation on 2442163 (t = 743d), since the calculated spectrum is entirely radiated in the infrared (cf. Fig. 4.3). The nebular parameters are given by equations 7.1 for all calculated spectra. The Iron and Cobalt abundances vary with time according to equation 3.1 and are listed in Table 5 along with the temperatures and ionization states.

The agreement between the calculated and observed spectra is clearly the best for times between Julian Day 2441653 (t = 233d) and Julian Day 2441796 (t = 376d). Focusing for the moment on the three spectra within this time interval, it is clear that the observed spectra undergo significant evolution. The nature of this evolution is evident in Figure 7.4a, where the Julian Day 2441653 and 2441796 spectra are shown overlaid. The equivalent information for the model spectra is shown in Figure 7.4b. The most striking changes in the observed spectra, namely the decreased intensity of the features near 6000 Å and the increased intensity of the features with $\lambda > 6700$Å, are also present in the model spectra, although relatively smaller increases in intensity of the features near 5300 Å in the model spectra are not present in the observations. The similarity in the evolution of the calculated and observed spectra increases one's confidence in the applicability of the model.

The comparison of the spectra at Julian Day 2441507 (Fig. 7.3a) further increases this confidence. In spite of the fact

that many spectral features are not properly predicted, many major features of the observed spectrum are clearly identifiable in the model spectrum. Additionally, this spectrum differs radically from the later spectra in that it has the general appearance of a smooth continuum with relatively small scale absorption and emission features. The shape of this quasi-continuum, which is distinctly non-Planckian (cf Kirshner et al 1973a), is exceedingly well predicted by the model. This indicates that line blocking effects are being accounted for properly, and that the chosen interstellar reddening correction of $E_{BV} = 0.22$ is nearly correct. It is interesting that such a quasi-continuum results solely from spectral lines, with no truly continuous emission or absorption being present. The lack of detailed correspondence between the spectral features of the model and observed spectra may largely be due to the absence of CoIV-VI and the lack of CoII allowed lines in the calculations.

The spectral comparisons at Julian Day 2441865 and 2442163, in contrast to those at earlier times, appear to indicate a serious breakdown of the model. This is not unexpected. As discussed at length in previous sections, for $t \gtrsim 400d$ the optical luminosity is expected to be emitted from a progressively thinner outer region of the nebula which has a density lower than the critical density for the IRC. The approximation of spatial homogeneity, which has been employed extensively in the model, then loses all validity, and the optical spectrum is expected to show strong

effects from temperature and ionization gradients. In particular, the relatively dense inner region of the nebula is expected to have a large fractional abundance of neutral iron which will absorb and redistribute in frequency photons emitted by the hotter, more rarefied outer region. This will, among other effects, result in significantly altered line profiles and intensities for the lines from the outer region. Lines emitted shortward of 4000 Å should be particularly strongly affected, since this is the spectral region with the strongest FeI absorption (cf Figure 5.1).

To some extent similar effects are present at earlier times also, and may be the explanation for some of the discrepancies between the calculated and observed spectra. This is especially likely to be the case for the earliest spectrum considered here, since at t = 87d the energy deposition is dominantly due to gammas (cf Figure 6.1) and is quite nonuniform spatially. This will once again result in strong temperature and ionization gradients, but with direction reversed from those present at very late times. The central region now has higher temperature and ionization state than the outer region. Once again line profiles are altered from those used in the homogeneous model, this time with classical P-Cygni type profiles resulting. We note that the reversal in sign of the density and temperature gradients with time provides a natural explanation for the relatively good agreement of the simple model with the observations at intermediate times when the gradients are minimized.

B. Atmospheric Absorption Lines

The fact that our model of the SNI nebula ignores the effects of material external to the Ni^{56} core is a further source of discrepancies with observations. The atmosphere in fact may be expected to interpose absorption lines between the core and the observer. Considerable effort has been devoted to the identification of such absorption lines in SNI, especially during the photospheric phase (cf Branch and Tull 1979, Kirshner and Oke 1975, Mustel 1975, Greenstein and Minkowski 1973). At later times, most of the identifications become quite uncertain, especially in light of the calculated spectra presented here. Mustel (1975) has, for example, identified the minimum near 5800 Å present in the spectra of SN1972e as the HeI 5876A line in blueshifted absorption. This feature is well reproduced in the calculated spectra without He being present, however. Caution is clearly required. What appears to be an absorption line may simply be a minimum in a complex emission spectrum. Perhaps the only atmosphere absorption lines which can be identified with confidence at late times are those due to CaII. Blueshifted absorption features from the H and K lines ($\lambda \approx 3950$ Å) and the infrared triplet ($\lambda \approx 8600$ Å) are very strong in all of the SN1972e spectra until at least Julian Day 2441796, and are probably present even at later times. Branch (1980) has fit P-Cygni profiles to these features and shown that the absorbing material must have a velocity profile extending to about 1.8×10^9 cm/sec, which shows that the absorption is

occurring in the atmosphere and not in the much more slowly moving core material modelled here. Inclusion of these CaII absorption features would significantly improve the fit between the calculated and observed spectra. Other atmospheric absorption features are undoubtedly present. The NI lines in the 9000 Å $\lesssim \lambda \leq$ 11000 Å region suggested by Mustel (1975) seem particularly likely. We note that the low ionization states apparently present in the atmosphere are probably consistent with photoionization equilibrium in the UV radiation field generated by recombinations in the core.

C. Uncertainties in Atomic Data

A final source of disagreement between the model and observations is inaccuracies in atomic data. Some of these have already been "lumped" in the adjustable parameters of the model, such as Φ_R. The effect of variations in these parameters will be discussed below. Other types of inaccuracies cannot usefully be parameterized in this fashion, however. The most important example of this concerns the collision strengths Ω_{ij} used to determine the level populations. As discussed in Section IV the adjustable parameter ω has been included in a simple form for the Ω_{ij} (cf equation 4.47) and its value approximately determined by normalizing to the only available detailed calculations of Ω, those of Garstang et al (1978) for FeIII. While this procedure is quite satisfactory for determining the thermal balance, it is less

so for predicting detailed spectra features. As was shown previously in Figure 4.1, individual collision strengths may be in error by more than an order of magnitude. Particularly at late times, when collisional excitation rates are small compared to radiative decay rates even for forbidden lines, an error in a collision strength is directly reflected in the emission rates of lines. On the whole this does not result in gross distortion of spectral features because even the smallest features in the late time SNI spectra are mostly composed of blends of many lines. Still, some distortion results and it is most serious at late times.

This is probably the cause for the relatively inaccurate shape calculated for the spectral feature with 6800 A $\lesssim \lambda \lesssim$ 7800 A. This feature is due entirely to FeII in the calculations, so that its shape, which evolves significantly with time, is unaffected by the changing ionization balance. Experimentation has shown that the calculated shape of this feature is quite insensitive to temperature but changes significantly (and incorrectly) with density. This points convincingly to inaccurate collision strengths as the cause of the difficulties. Undoubtedly other spectral features are also distorted in this way.

D. Evidence for Co^{56}

From the above discussion it appears likely that the discrepancies between the calculated and observed spectra are due to the

known limitations of the model rather than to a basic lack of applicability of the model to SNI. We may now address the most crucial question for the Ni^{56} model of SNI: Is there evidence for the expected decaying abundance of Co^{56}?

Two sequences of calculated spectra are shown in Figures 7.5a-c in the same format as the earlier figures, beginning at Julian Day 2441653 and extending to Julian Day 2441796. The upper spectra are identical to those shown previously, with the Co abundance set to the value expected from the Ni^{56} model for each time, while the lower sequence has zero Co abundance. The difference is striking. The spectral region 5700 Å $\lesssim \lambda \lesssim$ 6400 A, which is very accurately reproduced in the models containing Co, is grossly in error when Co is absent. As illustrated in Figures 7.6a-c this spectral region is dominated by CoIII emission and its decline with time relative to other spectral features is strong evidence for a decaying Co abundance. A less prominent decaying spectral feature clearly visible in the Julian Day 2441653 spectrum at $\lambda \approx 6870$ A is also well fit by CoIII emission. The contributing lines are forbidden transitions originating from the a^4P and a^2G multiplets of CoIII (cf Appendix I).

An alternative explanation for these spectral features has been proposed by Branch (1980a,b), who fits the region near 6000 A with a P-Cygni profile from NaI. This cannot be ruled out, but seems unlikely. In the absence of Co, the 6000 Å region is in a deep trough in the emission calculated spectrum so that there is

no "continuum" with which to form a P-Cygni line. It is clearly not sufficient to add NaI absorption to the current nebular model with Co emission somehow suppressed. A different mechanism for the formation of the entire spectrum is required. Additionally, it seems difficult to have the optical depth of the NaI absorption vary with time in a way that will reproduce the decay of the 6000 Å feature. This question may be definitively answered by removing the limitations of the current nebular model which prevent an accurate calculation of the spectrum at Julian Day 2441507. Since at this time the Ni^{56} model predicts a Co abundance of .50, an identification of Co will not have to rely on a single spectral feature. This is evident from Figure 7.7, which shows the role of Co in forming this spectrum as predicted by the current nebular model.

E. Limits on the Ni^{56} Mass and Velocity

We must now inquire what limits can be placed on the mass and velocity of the ejected Ni^{56} from the requirement that the calculated optical spectrum agree with observations. Extensive experimentation with the numerical model has shown that the optical spectrum is most sensitive to the ionization state of the nebula and is less strongly affected by the temperature and the line profile shapes. Additionally, as the analysis of Section IV

leads us to expect, the ionization state is to a good approximation a function only of Δ, the nebular density parameter. To first order then, the proper spectrum results when

$$\Delta \equiv \frac{U_9^3 \, (1 - (1 - h)^3)}{\mathcal{M}} = \Delta^* \tag{7.2}$$

where Δ^* is a constant determined by fitting the model spectra to the observations, and was found above to have the approximate value 0.5. The value of Δ^* is, however, dependent on several atomic physics parameters which have been taken to be known constants but are in fact not known with certainty. Additionally, the shape of the optical spectrum varies smoothly with Δ, and there is a "dead band" about Δ^* within which Δ can vary without affecting the spectrum significantly. In attempting to set limits on Δ and U_9 for real SNI these uncertainties must be taken into account.

The atomic physics quantities which affect the ionization balance are A, α_{rec}, and ϕ_R. The analysis of Section IV determined that when $\phi_R = 0$ the ionization state depends on these quantities through the parameter (cf equation 4.12)

$$z = \Delta \frac{A}{\alpha_{rec}} \tag{7.3}$$

When $\phi_R \neq 0$ the significance of z is basically unchanged but recombination rates are replaced by effective recombination rates which depend on ϕ_R and the ion abundances in a nonlinear way. In general the ionization state which results from one value of ϕ_R cannot be reproduced for a different ϕ_R no matter what value is chosen for z. For ϕ_R restricted to a limited range, however, ionization states are closely similar for constant values of the quantity

$$z_{eff} = \Delta \frac{A}{\alpha_{rec}} \frac{1}{1 - \phi_R} \tag{7.4}$$

The parameter z_{eff} is useful for an approximate specification of the ionization state when $0.3 \lesssim \phi_R \lesssim 0.6$. Differences are noticeable, however, in spectra resulting from the same values of z_{eff} but different values of ϕ_R within this range, and comparison with observations shows that somewhat better results are obtained when $\phi_R \approx 0.6$. This was the value used in the calculation presented above, for which

$$z^*_{eff} = .055 \tag{7.5}$$

We expect then that any model for which $z_{eff} \approx z^*_{eff}$ will generate approximately the correct spectral shape. This is most usefully expressed as

$$\mathcal{M} = \frac{U_9^3 \, (1 - (1-h)^3)}{0.5} \left(\frac{A}{1.33 \times 10^{-14}} \right) \left(\frac{3.0 \times 10^{-13}}{\alpha_{rec}} \right) \left(\frac{0.4}{1 - \phi_R} \right) \quad (7.6)$$

It is evident that since h, the thickness of the shell, may in principle be arbitrarily small, this expression can not be used to set a lower limit on $\mathcal{M}$, but only an upper limit. There is of course some minimum value of h which may be considered physically reasonable. We recall from Section II that the parameter h was introduced not from the expectation that the actual SNI nebula is shell-like, but rather from the need to simulate the fact that a realistic density profile will possess a higher mass-averaged density than a uniform sphere with the same mass and expansion velocity. With the present level of uncertainty in the quantities that enter equation 7.6, however, a lower limit on $\mathcal{M}$ from it is not useful. The limit derived from the bolometric luminosity in Section VI is encountered first.

We assume that both A and α_{rec} are known within 30%. The "deadband" has been found to be roughly ± 30% also. The maximum value for $\mathcal{M}$ is then

$$\mathcal{M} \lesssim 4.4 \; U_9^3 \quad (7.7)$$

where we have assumed $\phi_R \lesssim 0.6$. This is probably an overly conservative upper limit. If one has information on the actual density profile, the limit may be express as

$$\mathcal{M} \lesssim 4.4 \left(\frac{\rho_0}{\bar{\rho}}\right) U_9^3 \tag{7.8}$$

where $\bar{\rho}$ is the mass-averaged density of the profile and ρ_0 is the density of a uniform sphere with the same mass and expansion velocity (cf. equation 2.4) If, for example, the density profile is that of Colgate and McKee (1969) which was adopted in Section VI (equation 6.24), then

$$\frac{\bar{\rho}}{\rho_0} = \frac{3}{\alpha(3\alpha + 2)} \approx 4.4 \tag{7.9}$$

and the upper limit becomes

$$\mathcal{M} \lesssim U_9^3 \tag{7.10}$$

The limit relations 7.7 and 7.10 are shown in Figure 7.9 along with the limits previously derived from the light curve in Section VI.

As previously noted, the shape of the optical spectrum is directly influenced by the expansion velocity U_9 through the width of line profiles. Figures 7.8 a-c show the calculated spectrum at t = 264d for the standard parameters, except that line profiles are

those resulting from a transparent uniform sphere with expansion velocities U_9 = 0.5, 0.7, and 1.0, respectively, instead of the more accurate blueshifted profiles calculated in Section V. The effect of the profile width on the shape of the spectrum is evident. Also of interest is the fact that the differences between the spectrum calculated with the accurate profiles of Section V, and that calculated with the simple parabolic profiles, are slight if the velocities used for the profiles are the same (Figures 7.5b and 7.8b). This is true only at late times. At earlier times (e.g. t = 87d), the spectrum is appreciably affected by the use of the proper blueshifted profiles, since a wider spectral region is blocked by optically thick allowed lines (cf Fig. 5.1). We conclude from examination of Figures 7.8 a-c that the expansion velocity is constrained by the profile widths to the approximate range

$$0.5 \lesssim U_9 \lesssim 1.0 \qquad (7.11)$$

Branch (1980b) has concluded from his analysis of the SN1972e spectrum near maximum light that no Co is present at velocities greater than 8×10^8 cm/sec. This allows us to place the more restrictive requirements on U_9 that

$$0.5 \lesssim U_9 \lesssim 0.8$$

These limits are incorporated into Figure 7.9.

We see that, even with the large uncertainties currently present in the astronomical and atomic physics data required for the analysis of the light curves and optical spectra of SNI, interesting limits on the mass and ejection velocity of Ni^{56} are obtained. Some models for SNI, such as the detonating dwarf model of Taam (1980; Woosley et al 1980; Weaver et al 1980) can be definitively ruled out as an explanation of SN1972e. This model, which results in a nearly bare Ni^{56} core of $\mathcal{M} = 1.1$ expanding at $U_9 \approx 1.7$ with $\bar{\rho}/\rho_0 \approx 1.7$, produces the optical spectrum shown in Figure 7.10 at t = 264d. There is little resemblance to the observed spectrum. Similar results are obtained for the model of Colgate et al (1980), which was chosen to fit the light curve.

TABLE 5

Results From the Standard Run

$\mathcal{K}$ = 0.7
U_9 = 0.7
h = 1.0
D = 3 Mpc

	JD - 2441000				
	507	653	684	796	865
t (days)	87	233	264	376	445
f_{Co}	.50	.14	.10	.04	.02
N (cm^{-3})	2.45(7)	1.28(6)	8.78(5)	3.04(5)	1.83(5)
X	2.40	2.48	2.46	2.31	2.21
T (°K)	9530	7700	7550	6640	6130
f_0	5.3(-5)	4.1(-5)	4.5(-5)	9.2(-5)	1.4(-4)
f_1	8.8(-2)	7.2(-2)	7.4(-2)	1.1(-1)	1.4(-1)
f_2	4.9(-1)	4.6(-1)	4.6(-1)	5.2(-1)	5.4(-1)
f_3	3.6(-1)	4.0(-1)	3.9(-1)	3.2(-1)	2.8(-1)
f_4	5.3(-2)	6.5(-2)	6.3(-2)	4.2(-2)	3.2(-2)
f_5	5.3(-3)	6.6(-3)	6.4(-3)	4.11(-3)	3.11(-3)
L_{OPT}(erg/sec)	1.1(42)	7.4(40)	5.2(40)	1.3(40)	6.2(39)
L_{IR}(erg/sec)	1.7(40)	2.6(39)	2.1(39)	1.7(39)	1.7(39)
L_{UV}(erg/sec)	3.3(40)	2.4(39)	1.6(39)	4.7(38)	2.4(38)

Figure Captions

Fig. 7.0 The observed spectra of SN1972e reproduced from Kirshner et al (1973b) and Kirshner and Oke (1975). Vertical axis is the spectral flux $F(\nu)$ (erg cm^{-2} Hz^{-1} sec^{-1}). Horizontal axis is $\log_{10}$ ν. Each curve is labelled on right by JD-2441000, where JD is the Julian Date of the observation.

Fig. 7.1 The calculated spectrum resulting from the standard run at t = 264d (dashed line) is compared with the JD2441684 observation of SN1972e (solid line). Vertical axis is the spectral flux $F(\nu)$ (erg cm^{-2} Hz^{-1} sec^{-1}). Horizontal axis is $\log_{10}$ ν. Wavelength in Angstroms is shown across the top of the graph for reference.

Fig. 7.2 Same as Fig. 7.1 except dashed line shows contribution from the indicated ion to the calculated spectrum of Fig. 7.1.

Fig. 7.3 Same format as Fig. 7.1. Comparison between calculated spectra resulting from the standard run and SN1972e observations are shown for a series of observation times. The Julian Date of each observation is shown at upper right.

Fig. 7.4 Time evolution of SNI spectra. The spectrum at JD2441653 (solid line) is shown overlaid on the

spectrum at JD2441796 (dashed line). Axes are the same as Fig. 7.1.

a) SN1972e observations

b) calculated (standard run)

Fig. 7.5 Role of Co^{56} in SNI spectra is shown by two time series of spectra. The upper frame on each page shows the comparison between the SN1972e observation and the calculated spectrum from the standard run with the Co fractional abundance, f_{Co}, given by the decay of Ni^{56} with $f_{Ni} = 1.0$ at $t = 0$. The lower frame shows the same comparison with $f_{Co} = 0$, $f_{Fe} = 1$. Format is the same as Figure 7.1.

Fig. 7.6 Same as Fig. 7.4 except that the dashed line indicates the contribution of CoIII to the calculated spectra.

Fig. 7.7 Same as Fig. 7.4 except that the dashed line indicates the contribution of CoI, II, and III together to the calculated spectrum at JD2441507, when $f_{Co} = .50$.

Fig. 7.8 The effect of differing expansion velocities on the optical spectrum due solely to the resulting change in the emergent line profiles is shown. The same comparison is shown as in Fig. 7.1 except that line profiles resulting from a transparent sphere

expanding with velocity Up (10^9 cm sec^{-1}) have been used forming the calculated spectra.

a) Up = 0.5

b) Up = 0.7

c) Up = 1.0

Fig. 7.9 a) Limits on $\mathcal{M}$ and U_9 imposed by the optical spectrum. Vertical axis is the Ni^{56} mass, ($M_\odot$). Horizontal axis is expansion velocity U_9 (10^9 cm sec^{-1}). Curve labelled by "Δ" shows upper limit on $\mathcal{M}$ including atomic phsyics uncertainties (eqn 7.7). Curve labelled by "O" shows up per limit assuming no atomic physics inaccuracies. Curve labelled by "□" shows upper limit with $\bar{\rho}/\rho_0$ = 4.4 (eqn 7.10). Vertical lines show significant bounds on U_9 (see text).

b) Same as Fig. 7.9a except that the limits shown in Fig. 6.3 determined from the light curve have been added. Singly hatched area shows limits determined with the curve "Δ" of Fig. 7.9a, while the doubly hatched area results from the use of curve "O". The standard run is located by the indicated point.

Fig. 7.10 Same as Fig. 7.1 except that the calculated spectrum results from the detonating white dwarf model discussed in the text.

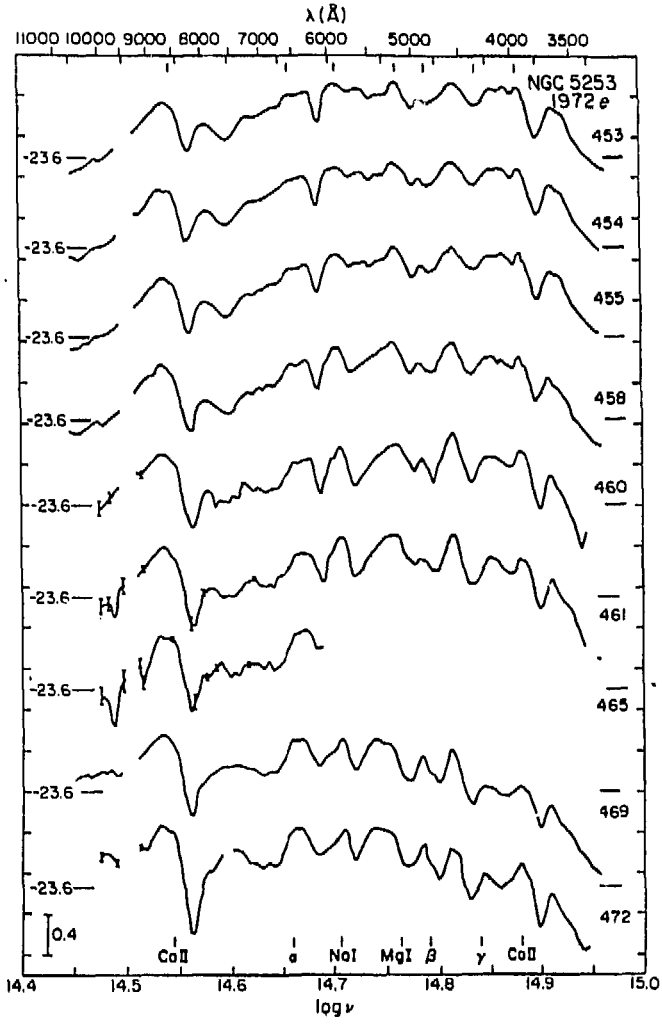
λ(Å)
11000 10000 9000 8000 7000 6000 5000 4000 3500
NGC 5253
1972e
453
454
455
458
460
461
465
469
472
-23.6
0.4
CaII
α
NaI
MgI
β
γ
CaII
14.4 14.5 14.6 14.7 14.8 14.9 15.0
log ν

Fig. 7.0

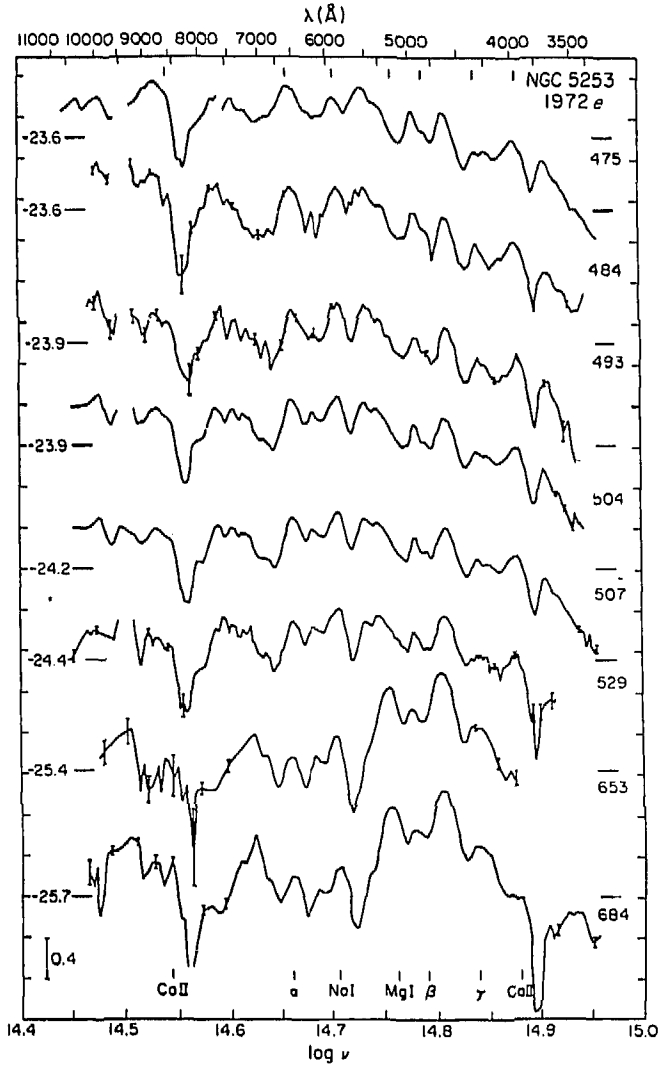
λ(Å)
11000 10000 9000 8000 7000 6000 5000 4000 3500
NGC 5253
1972 e
-23.6
475
-23.6
484
-23.9
493
-23.9
504
-24.2
507
-24.4
529
-25.4
653
-25.7
684
0.4
CaII
α
NaI
MgI
β
γ
CaII
14.4 14.5 14.6 14.7 14.8 14.9 15.0
log ν

Fig. 7.0 (cont.)

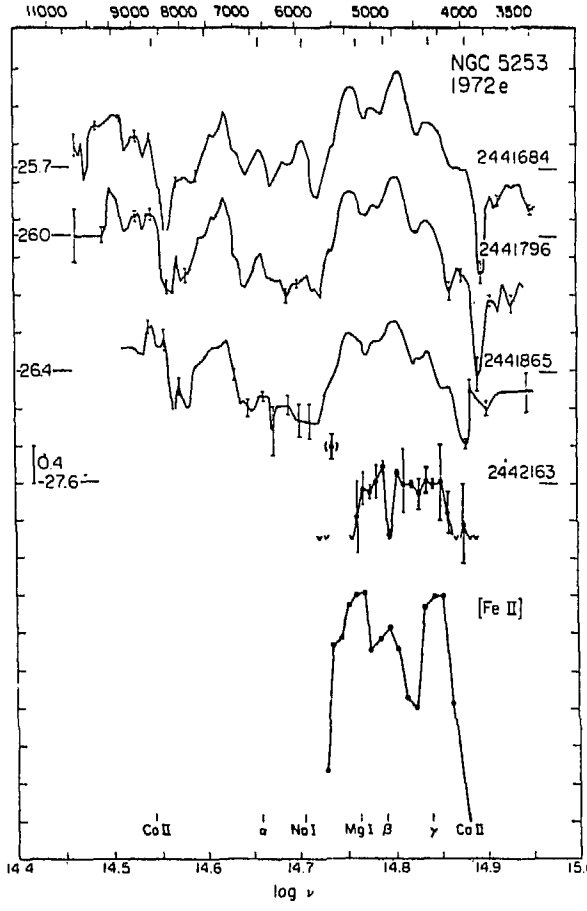
11000
9000
8000
7000
6000
5000
4000
3500
NGC 5253
1972e
25.7
2441684
260
2441796
264
2441865
0.4
-27.6
2442163
[Fe II]
CaII
α
NaI
MgI
β
γ
CaII
14.4
14.5
14.6
14.7
14.8
14.9
15.0
log ν

Fig. 7.0 (cont.)

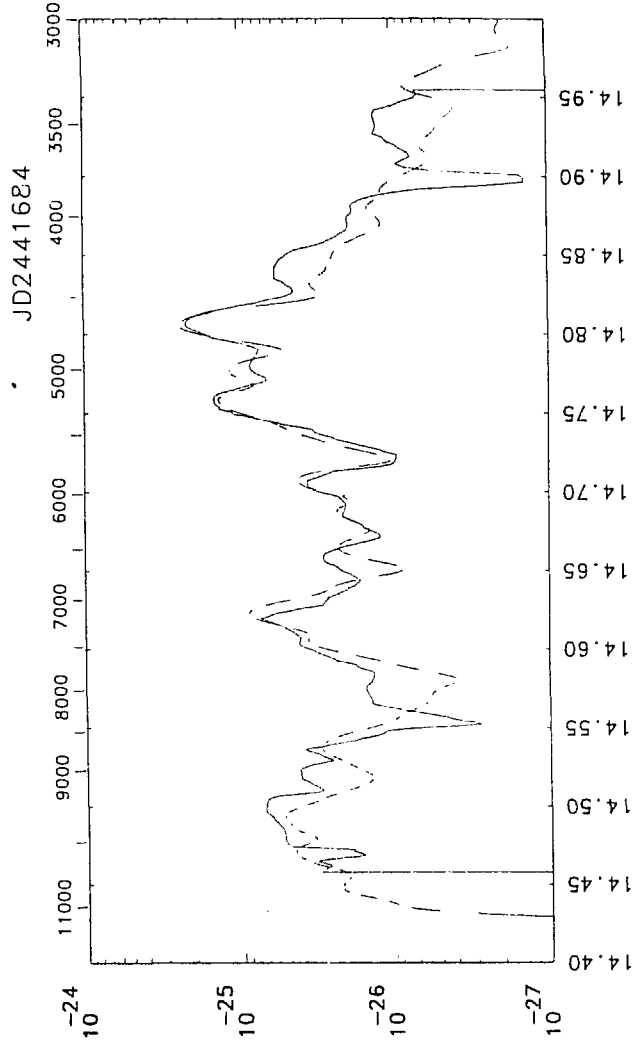
JD2441684
3000
3500
4000
5000
6000
7000
8000
9000
11000
14.95
14.90
14.85
14.80
14.75
14.70
14.65
14.60
14.55
14.50
14.45
14.40
10^{-24}
10^{-25}
10^{-26}
10^{-27}

Fig. 7.1

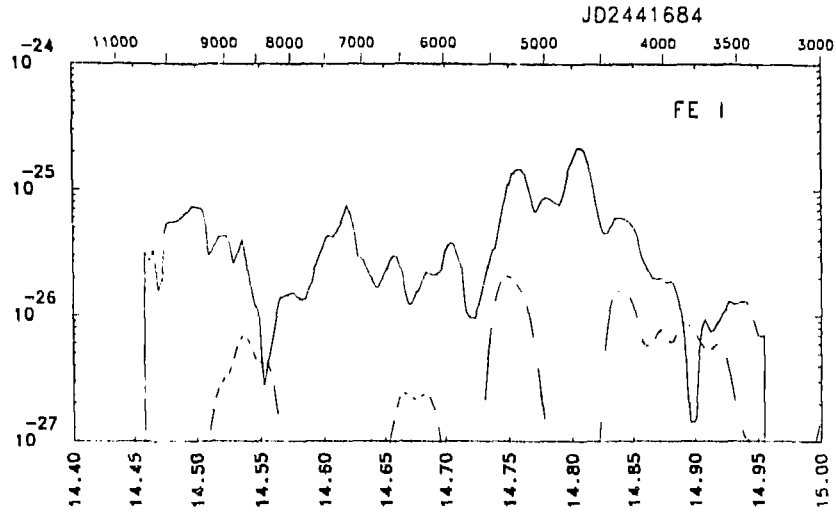
JD2441684
FE I
11000
9000
8000
7000
6000
5000
4000
3500
3000
10^-24
10^-25
10^-26
10^-27
14.40
14.45
14.50
14.55
14.60
14.65
14.70
14.75
14.80
14.85
14.90
14.95
15.00

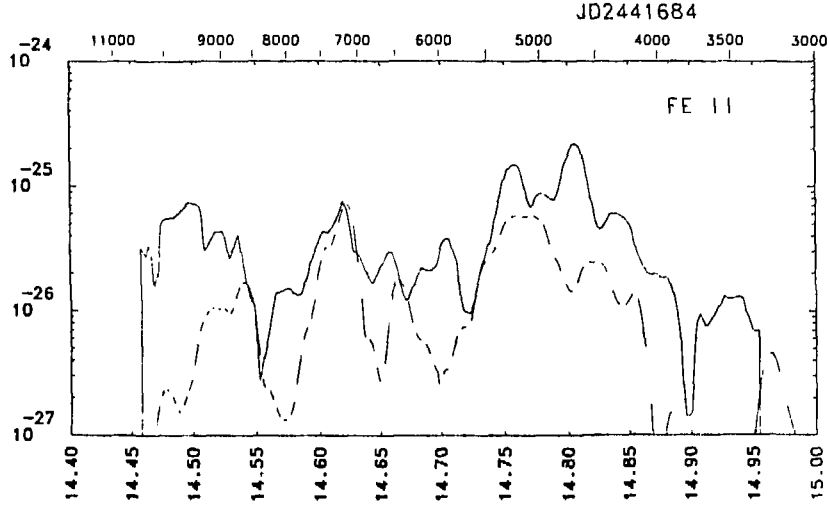
JD2441684
FE II
11000
9000
8000
7000
6000
5000
4000
3500
3000
10^-24
10^-25
10^-26
10^-27
14.40
14.45
14.50
14.55
14.60
14.65
14.70
14.75
14.80
14.85
14.90
14.95
15.00

Fig. 7.2

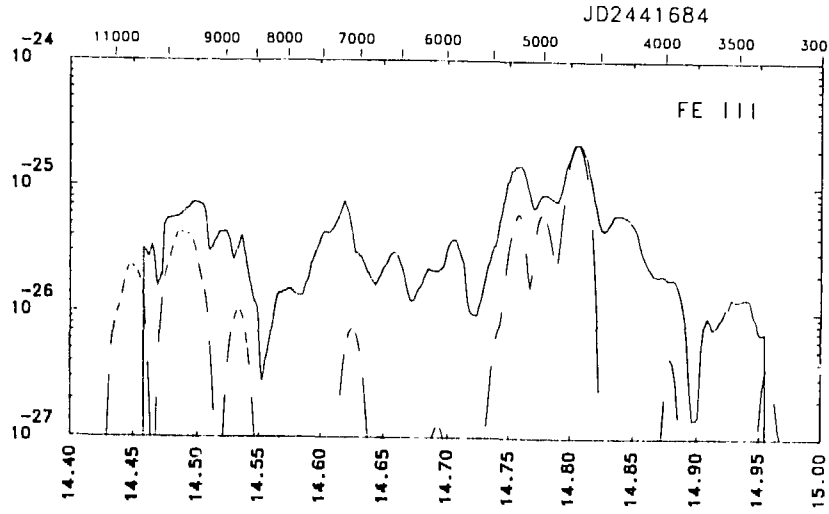
JD2441684
FE III
11000
9000
8000
7000
6000
5000
4000
3500
3000
14.40
14.45
14.50
14.55
14.60
14.65
14.70
14.75
14.80
14.85
14.90
14.95
15.00

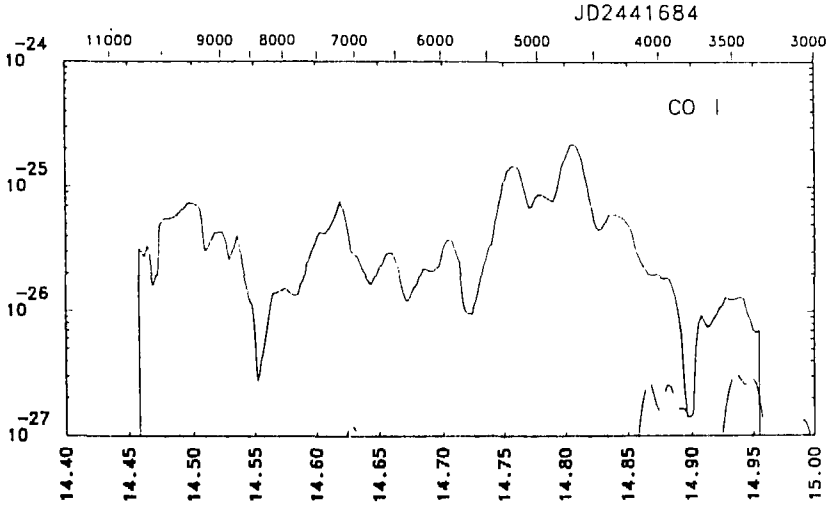
JD2441684
CO I
11000
9000
8000
7000
6000
5000
4000
3500
3000
14.40
14.45
14.50
14.55
14.60
14.65
14.70
14.75
14.80
14.85
14.90
14.95
15.00

Fig. 7.2 (cont.)

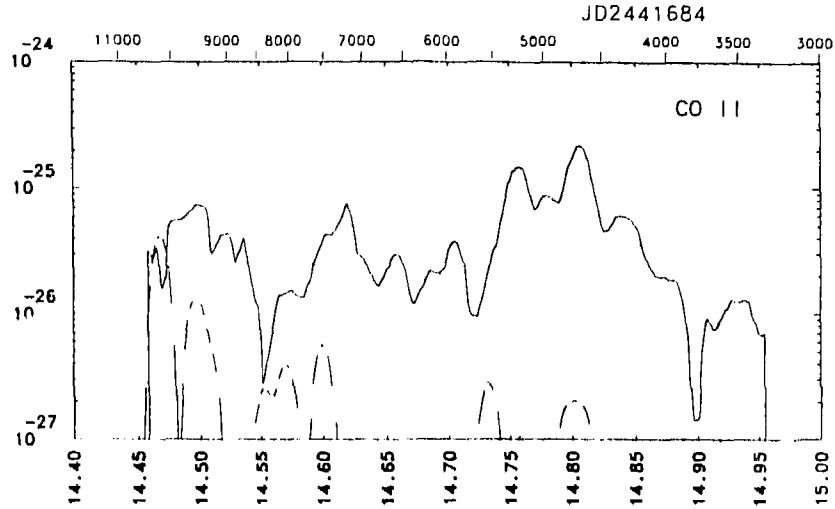
JD2441684
CO II
11000
9000
8000
7000
6000
5000
4000
3500
3000
14.40
14.45
14.50
14.55
14.60
14.65
14.70
14.75
14.80
14.85
14.90
14.95
15.00

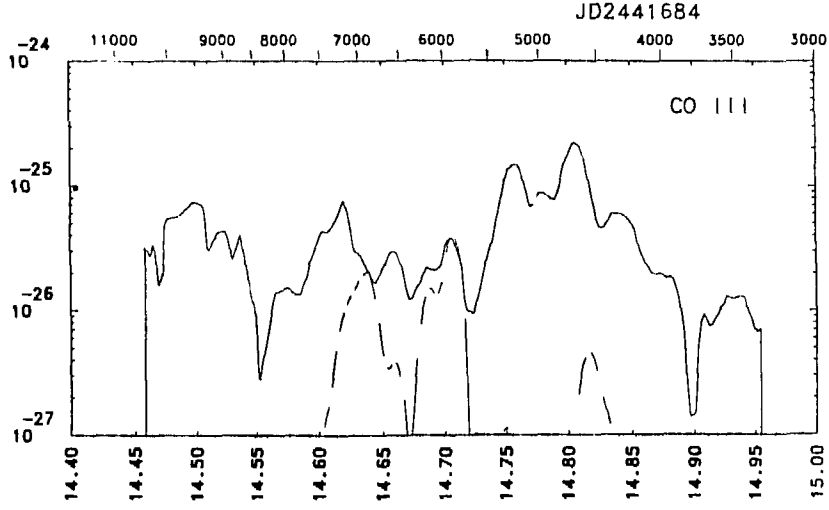
JD2441684
CO III
11000
9000
8000
7000
6000
5000
4000
3500
3000
14.40
14.45
14.50
14.55
14.60
14.65
14.70
14.75
14.80
14.85
14.90
14.95
15.00

Fig. 7.2 (cont.)

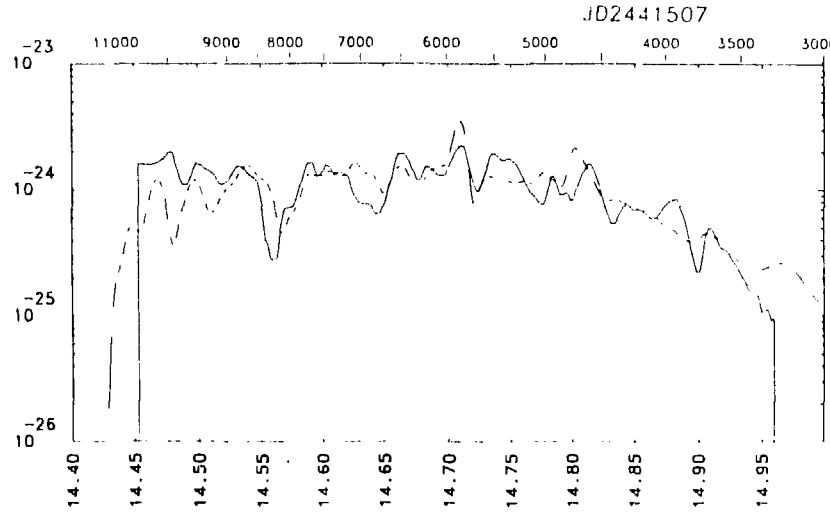
JD2441507
11000
9000
8000
7000
6000
5000
4000
3500
3000
10^{-23}
10^{-24}
10^{-25}
10^{-26}
14.40
14.45
14.50
14.55
14.60
14.65
14.70
14.75
14.80
14.85
14.90
14.95

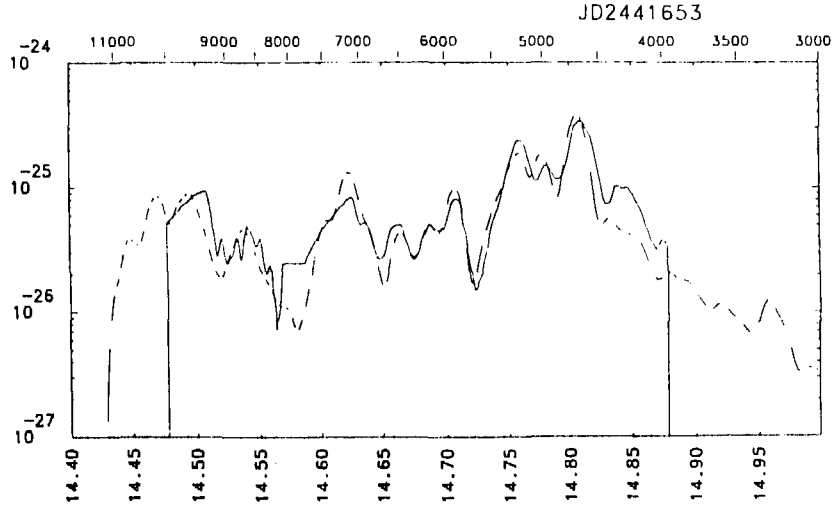
JD2441653
11000
9000
8000
7000
6000
5000
4000
3500
3000
10^{-24}
10^{-25}
10^{-26}
10^{-27}
14.40
14.45
14.50
14.55
14.60
14.65
14.70
14.75
14.80
14.85
14.90
14.95

Fig. 7.3

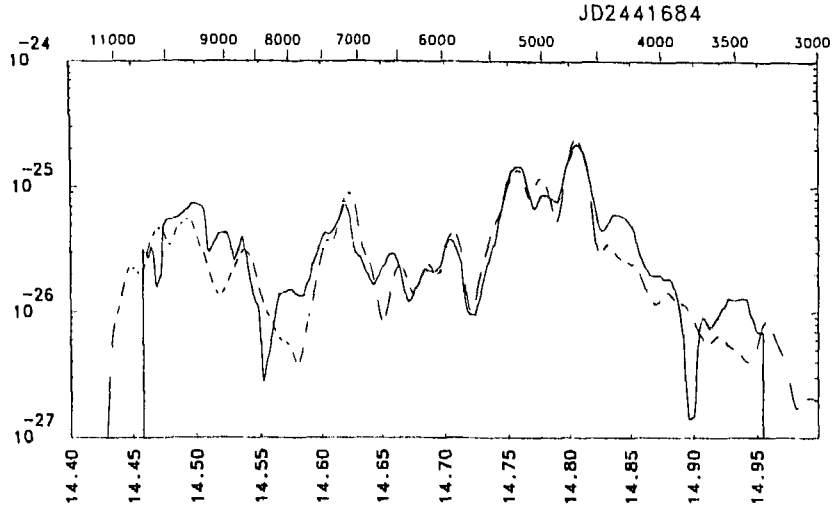
JD2441684
11000
9000
8000
7000
6000
5000
4000
3500
3000
10^{-24}
10^{-25}
10^{-26}
10^{-27}
14.40
14.45
14.50
14.55
14.60
14.65
14.70
14.75
14.80
14.85
14.90
14.95

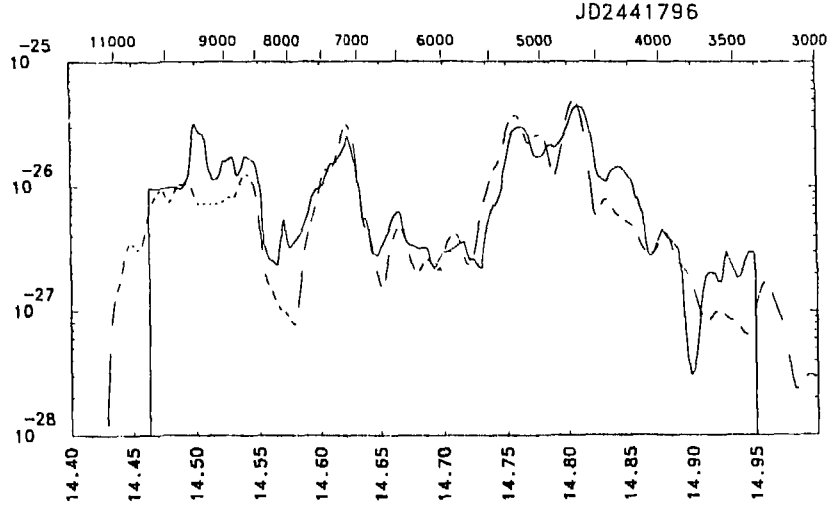
JD2441796
11000
9000
8000
7000
6000
5000
4000
3500
3000
10^{-25}
10^{-26}
10^{-27}
10^{-28}
14.40
14.45
14.50
14.55
14.60
14.65
14.70
14.75
14.80
14.85
14.90
14.95

Fig. 7.3 (cont.)

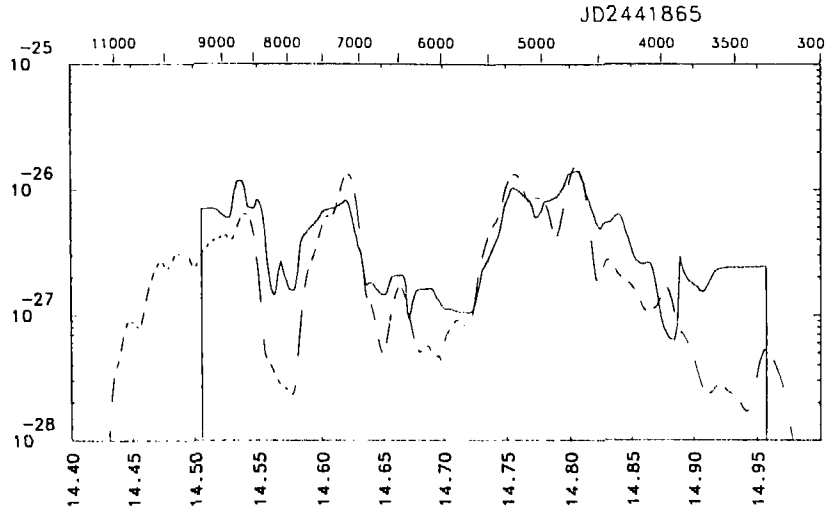
JD2441865
11000
9000
8000
7000
6000
5000
4000
3500
3000
10^{-25}
10^{-26}
10^{-27}
10^{-28}
14.40
14.45
14.50
14.55
14.60
14.65
14.70
14.75
14.80
14.85
14.90
14.95

Fig. 7.3 (cont.)

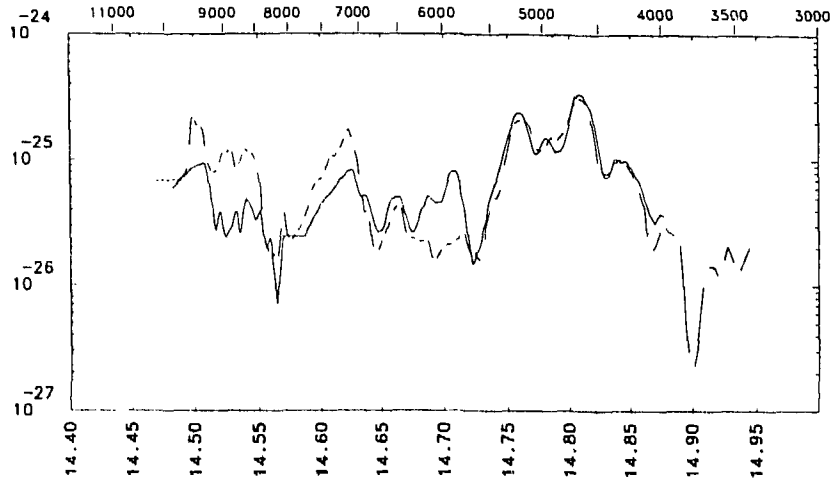

Fig. 7.4a

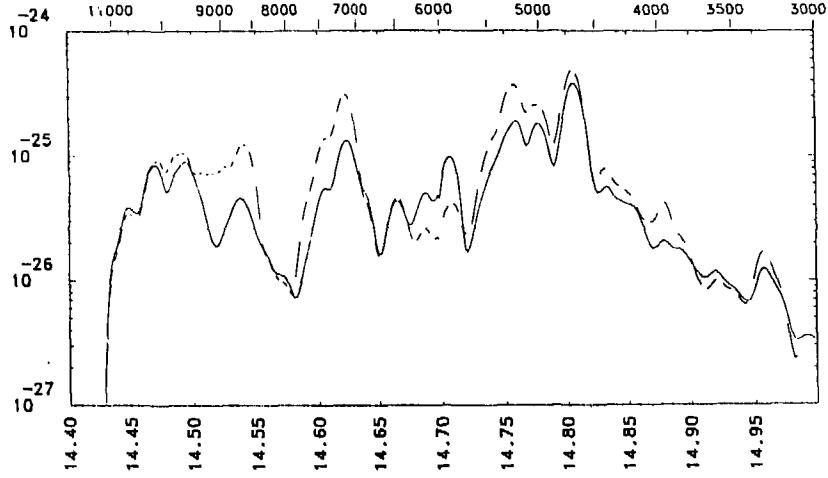

Fig. 7.4b

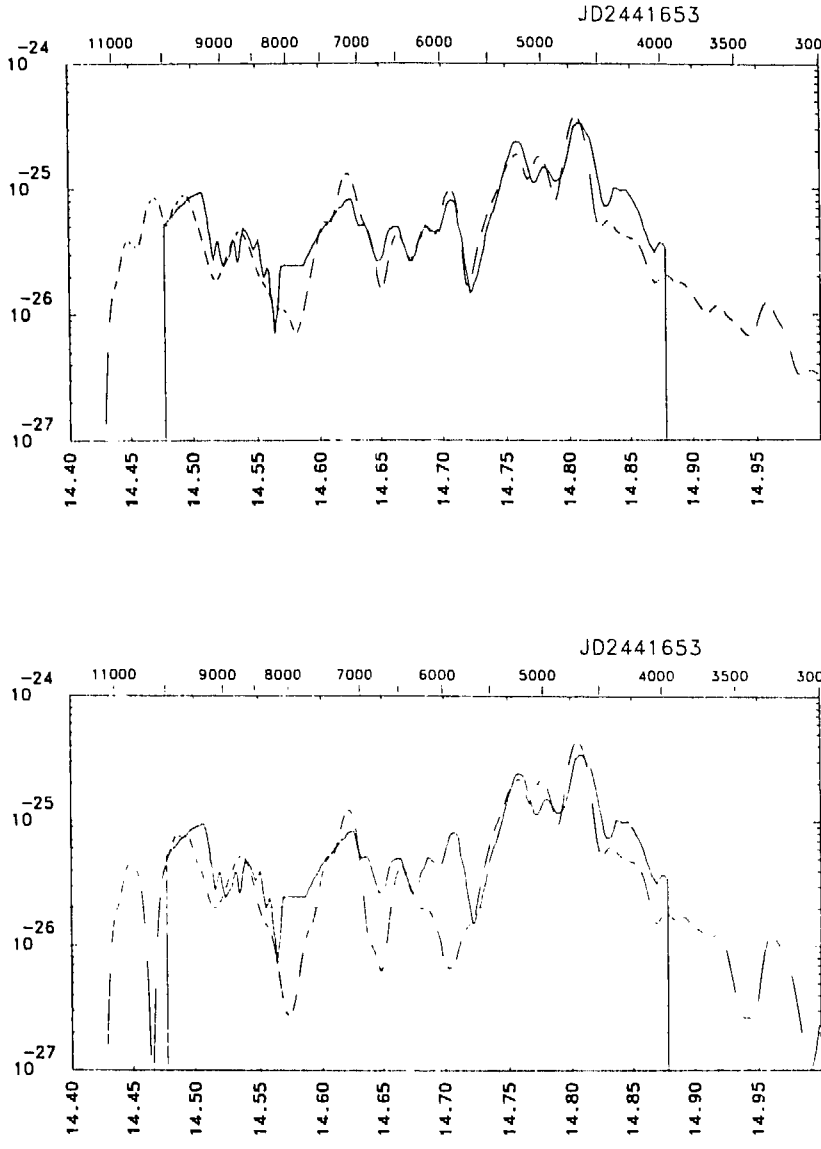
JD2441653
11000
9000
8000
7000
6000
5000
4000
3500
3000
10^{-24}
10^{-25}
10^{-26}
10^{-27}
14.40
14.45
14.50
14.55
14.60
14.65
14.70
14.75
14.80
14.85
14.90
14.95

Fig. 7.5

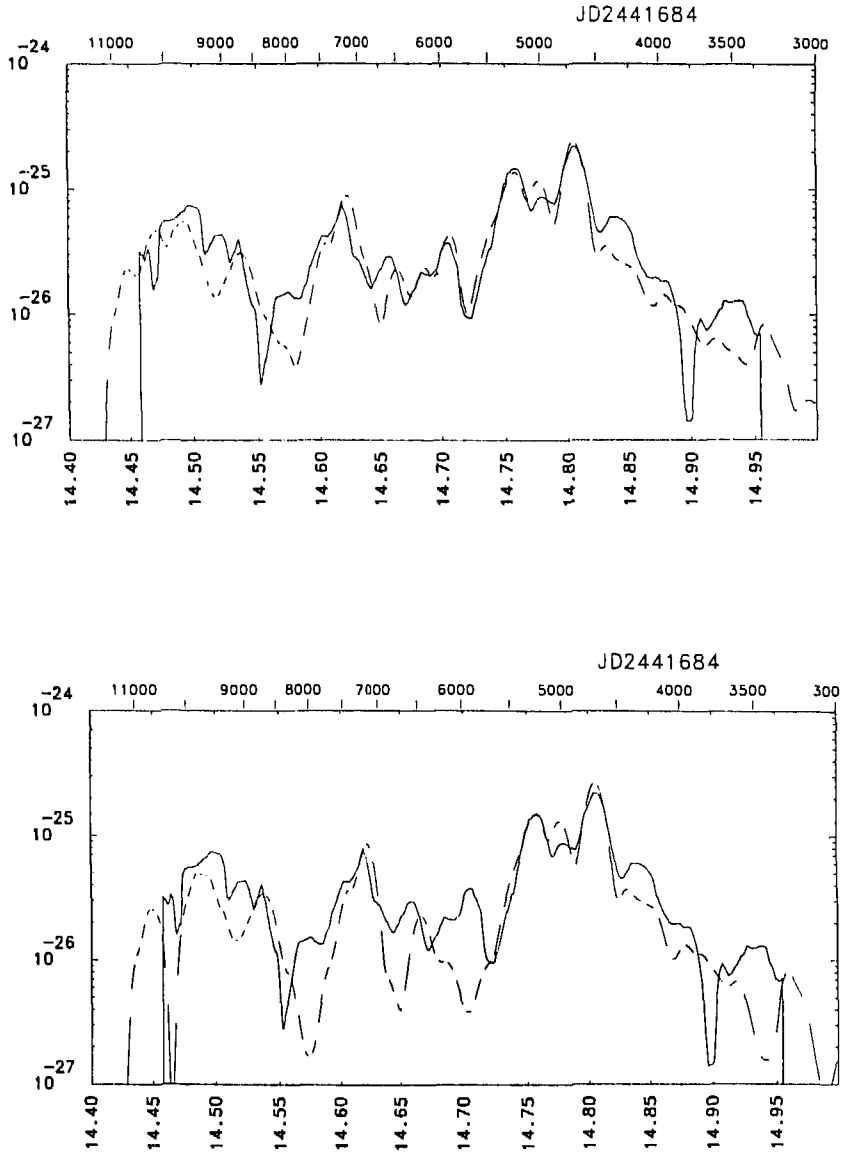
JD2441684
11000
9000
8000
7000
6000
5000
4000
3500
3000
10^{-24}
10^{-25}
10^{-26}
10^{-27}
14.40
14.45
14.50
14.55
14.60
14.65
14.70
14.75
14.80
14.85
14.90
14.95
JD2441684
11000
9000
8000
7000
6000
5000
4000
3500
3000
10^{-24}
10^{-25}
10^{-26}
10^{-27}
14.40
14.45
14.50
14.55
14.60
14.65
14.70
14.75
14.80
14.85
14.90
14.95

Fig. 7.5 (cont.)

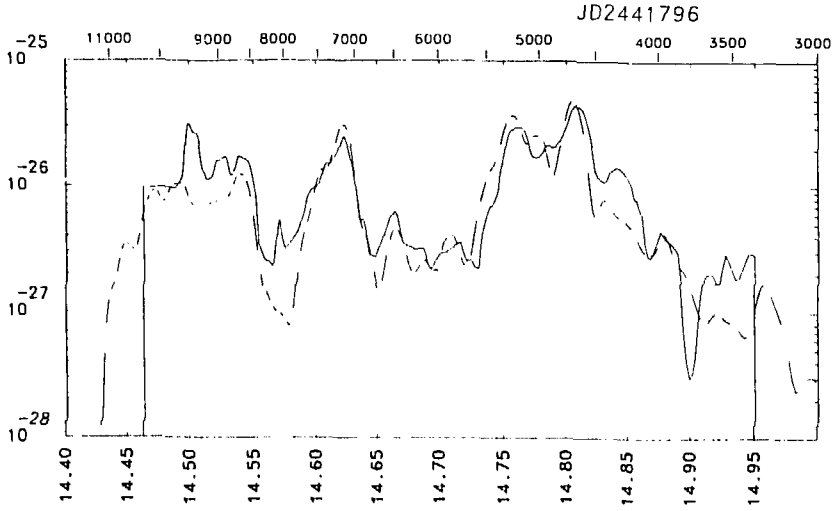
JD2441796
11000
9000
8000
7000
6000
5000
4000
3500
3000
10^{-25}
10^{-26}
10^{-27}
10^{-28}
14.40
14.45
14.50
14.55
14.60
14.65
14.70
14.75
14.80
14.85
14.90
14.95

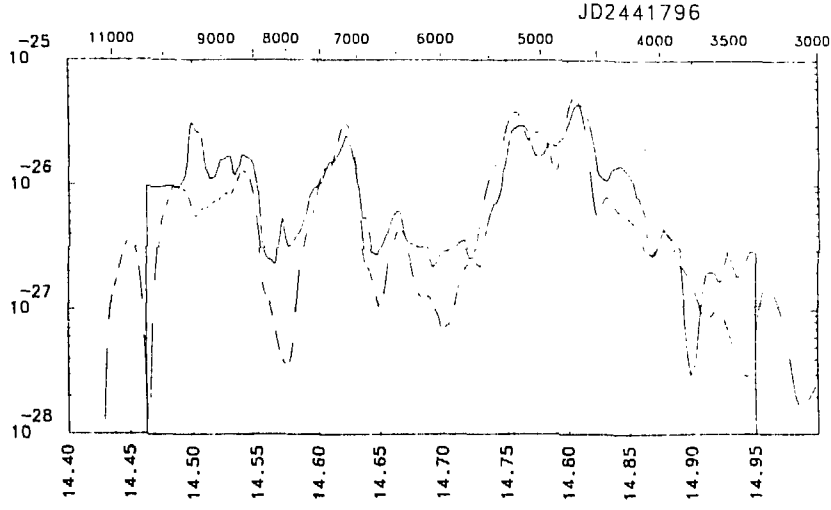
JD2441796
11000
9000
8000
7000
6000
5000
4000
3500
3000
10^{-25}
10^{-26}
10^{-27}
10^{-28}
14.40
14.45
14.50
14.55
14.60
14.65
14.70
14.75
14.80
14.85
14.90
14.95

Fig. 7.5 (cont.)

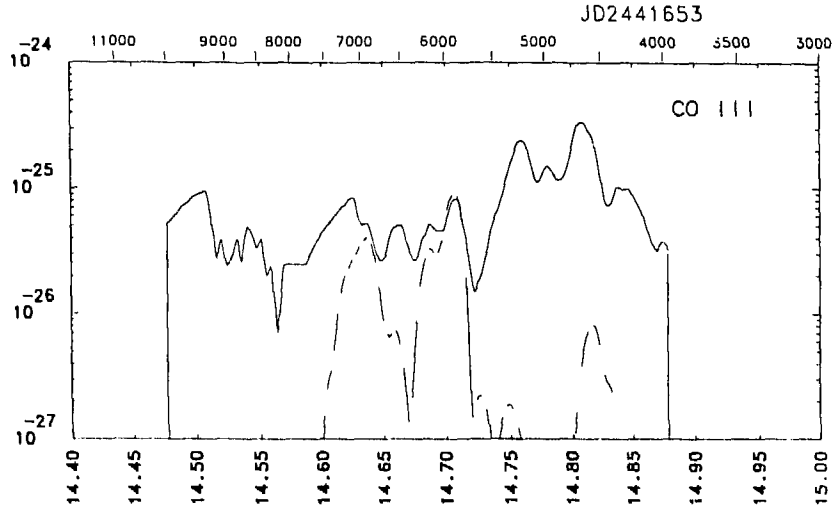
JD2441653
CO III
11000
9000
8000
7000
6000
5000
4000
3500
3000
14.40
14.45
14.50
14.55
14.60
14.65
14.70
14.75
14.80
14.85
14.90
14.95
15.00

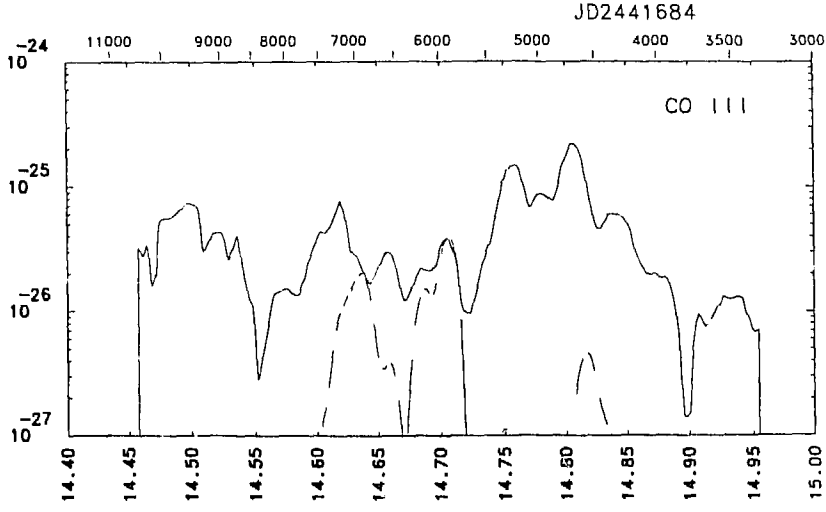
JD2441684
CO III
11000
9000
8000
7000
6000
5000
4000
3500
3000
14.40
14.45
14.50
14.55
14.60
14.65
14.70
14.75
14.80
14.85
14.90
14.95
15.00

Fig. 7.6

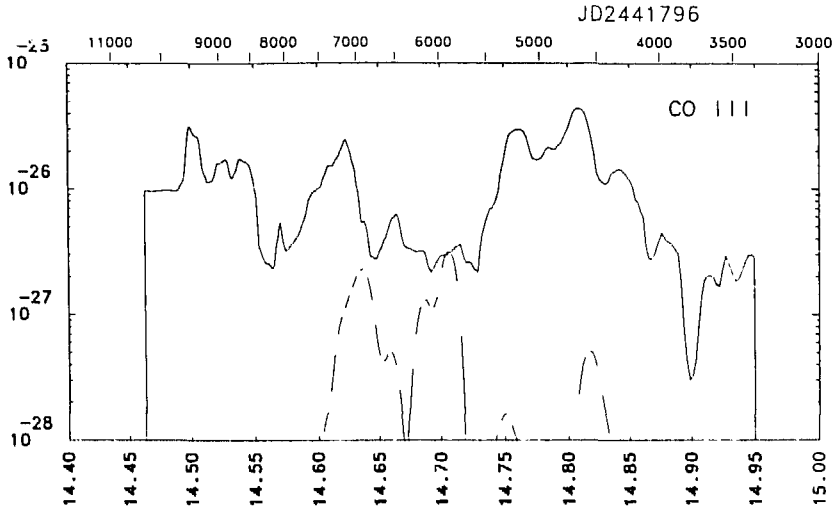
JD2441796
11000
9000
8000
7000
6000
5000
4000
3500
3000
CO III
10^{-25}
10^{-26}
10^{-27}
10^{-28}
14.40
14.45
14.50
14.55
14.60
14.65
14.70
14.75
14.80
14.85
14.90
14.95
15.00

Fig. 7.6 (cont.)

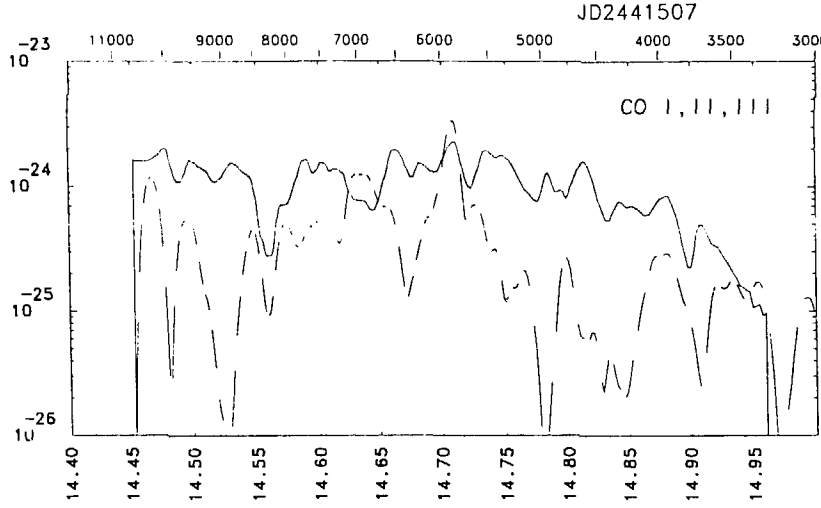
JD2441507
11000
9000
8000
7000
6000
5000
4000
3500
3000
10^{-23}
10^{-24}
10^{-25}
10^{-26}
CO I, II, III
14.40
14.45
14.50
14.55
14.60
14.65
14.70
14.75
14.80
14.85
14.90
14.95

Fig. 7.7

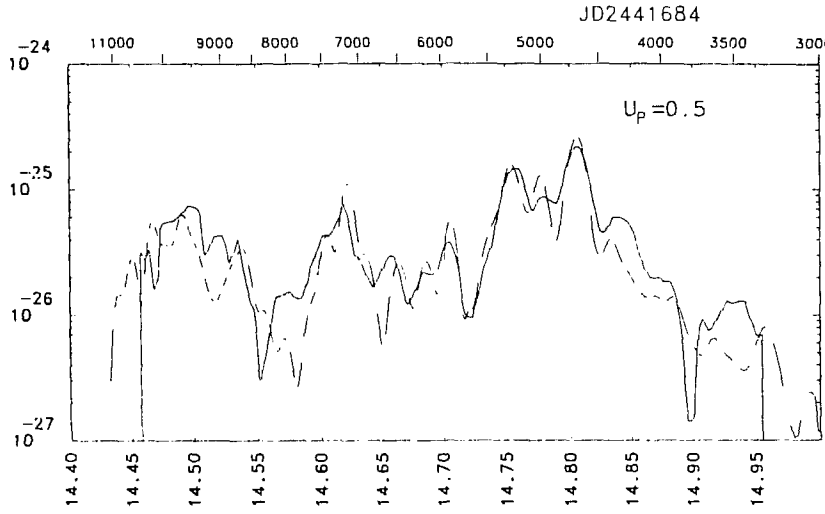

Fig. 7.8a

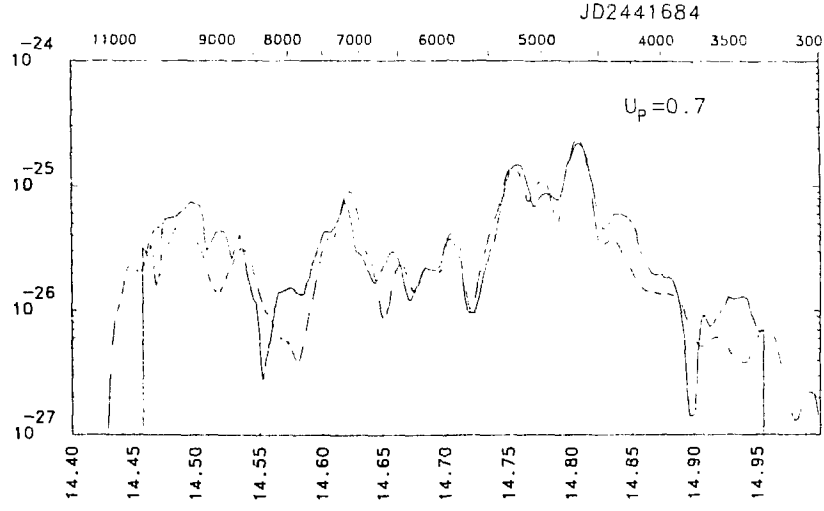

Fig. 7.8b

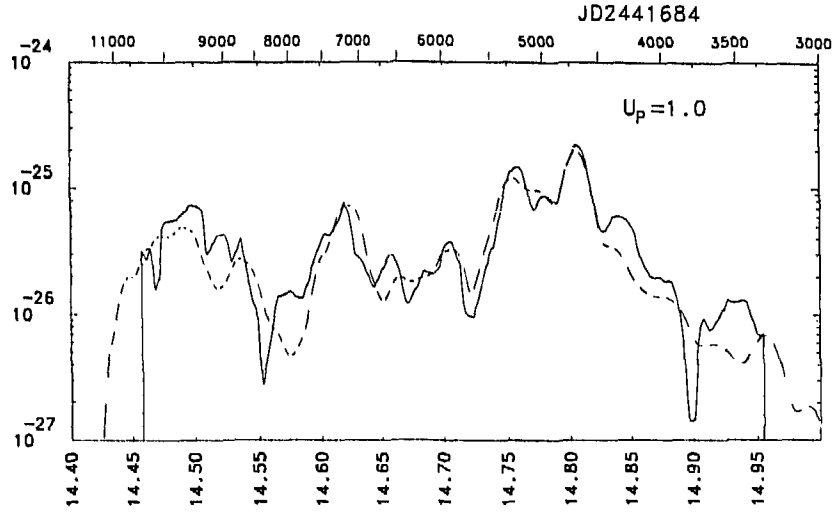
JD2441684
11000
9000
8000
7000
6000
5000
4000
3500
3000
10^{-24}
10^{-25}
10^{-26}
10^{-27}
U_p=1.0
14.40
14.45
14.50
14.55
14.60
14.65
14.70
14.75
14.80
14.85
14.90
14.95

Fig. 7.8c

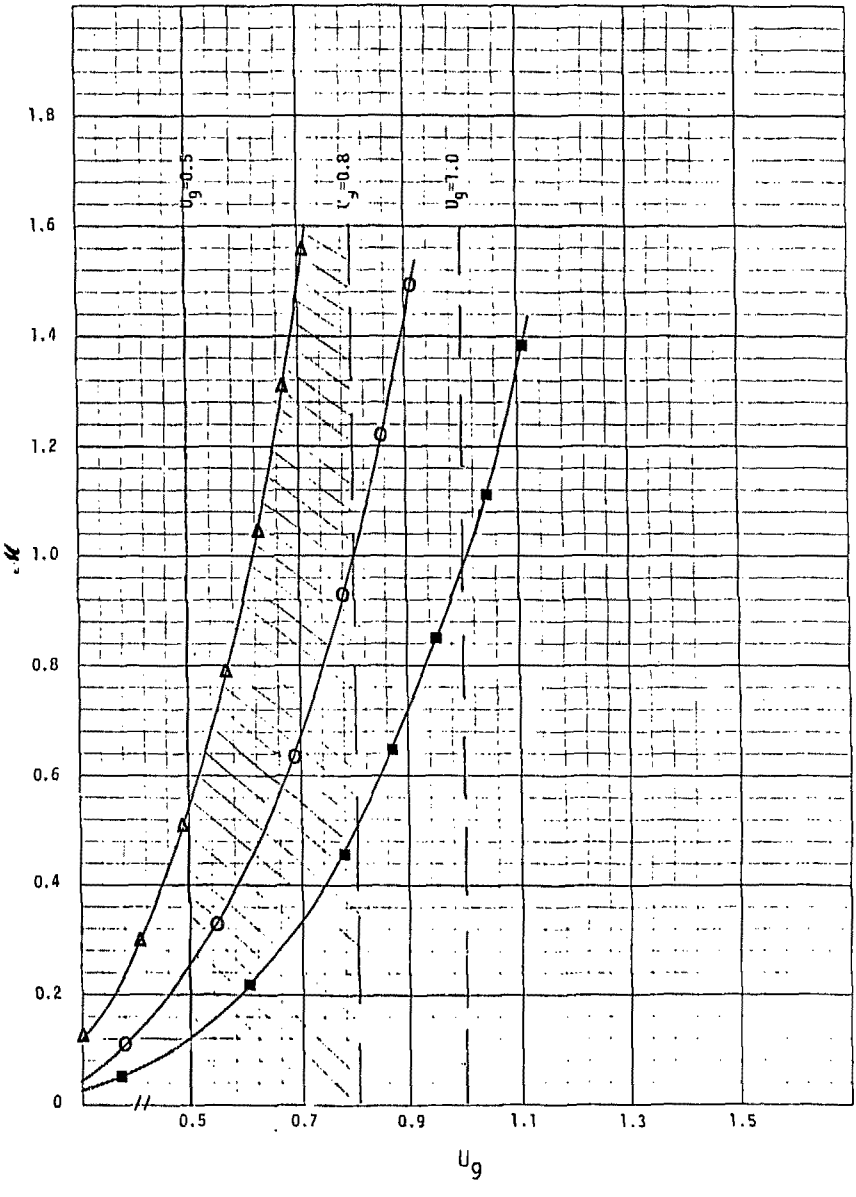

Fig. 7.9a

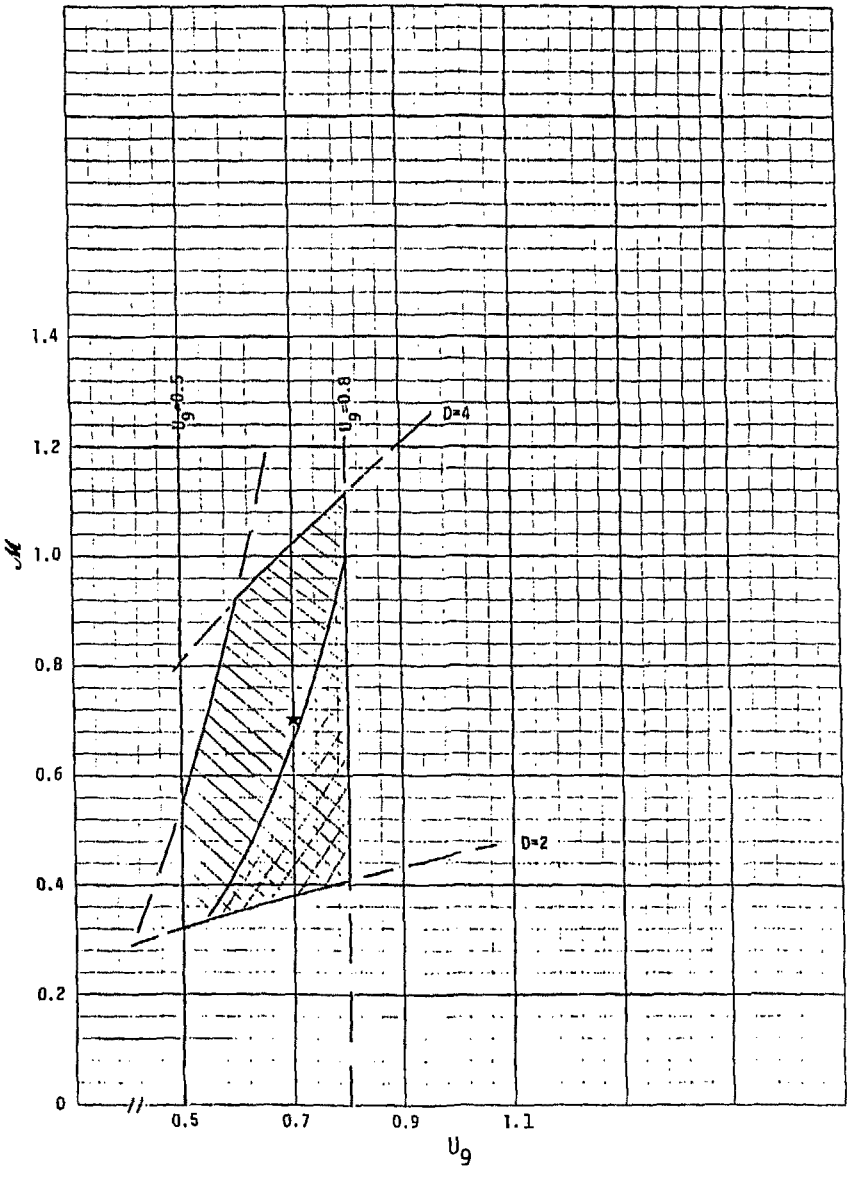

Fig. 7.9b

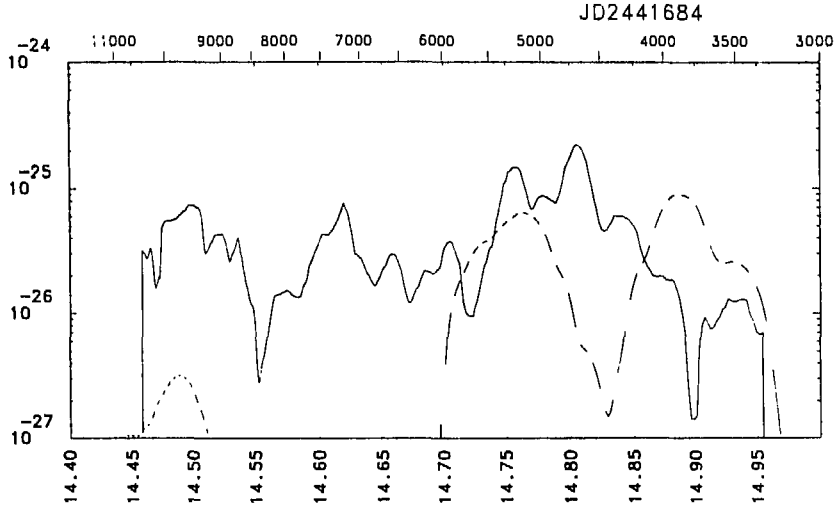
JD2441684
11000
9000
8000
7000
6000
5000
4000
3500
3000
10^{-24}
10^{-25}
10^{-26}
10^{-27}
14.40
14.45
14.50
14.55
14.60
14.65
14.70
14.75
14.80
14.85
14.90
14.95

Fig. 7.10

VIII. Conclusion: Constraints on the Progenitors of SNI

The results of Sections VI and VII show that the hypothesis that late time SNI luminosity is powered by the beta decay of Co^{56} is supported by observations of SN1972e. The SNI lightcurve and evolution of the optical spectra during the nebular phase are well reproduced by a numerical model which simulates the atomic processes and radiative transfer occurring in a homologouly expanding shell composed initially of Ni^{56}. Evidence for the expected decaying abundance of Co^{56} has been found in the observed spectra of SN1972e. The discrepancies between the observed optical spectra and those resulting from the numerical model appear to result from approximations incorporated in the model and incomplete or inaccurate atomic data.

The limits on the Ni^{56} mass and expansion velocity determined by the analysis are consistent with current astrophysical constraints:

a) The ejected mass is consistent with limits determined from galactic Fe abundance and observed SNI rates (Chevalier 1980; Tinsley 1980; Wheeler 1980).

b) The kinetic energy of the core falls well below the rough upper limit of 10^{51} - 10^{52} ergs set by observations of remnants (Gorenstein et al 1974).

c) The required Ni^{56} mass can be ejected by a wide variety of stellar models.

What can be inferred about the progenitor of SN1972e from the results of the numerical model? As discussed in Section VII, with the current uncertainties in atomic physics and the extragalactic distance scale, the progenitor is restricted only by the requirement that it eject 0.3 - 1.0 $M_\odot$ of Ni^{56} with maximum velocity of 5 x 10^8 - 1 x 10^9 cm/sec. This relatively weak restriction is of limited value in discriminating between possible progenitors. The required Ni^{56} mass is uncomfortably large for core collapse models, which typically produce less than 0.1 $M_\odot$ for stars with $\mathcal{M} \lesssim 15\ M_\odot$ (Weaver and Woosley 1979). Arnett (1979), however, has calculated that 0.3 $M_\odot$ of Ni^{56} may be ejected following core collapse in a low mass helium star, so the issue cannot be considered settled. Detonation and deflagration models can readily produce the required amount of Ni^{56} (Woosley, Weaver, and Taam 1980; Mazurek and Wheeler 1980; Sugimoto and Nomoto 1980). Detonation models tend to eject the Ni^{56} at velocities far in excess of the limit imposed by the optical spectra, however. The presence of material external to the core with density too low to sustain a detonation may eliminate this difficulty, since it absorbs a large fraction of the energy released by the detonation and leaves the Ni^{56} travelling at a low velocity. Weaver, Axelrod, and Woosley (1980) have estimated that 0.2 - 0.5 $M_\odot$ of helium external to a 1 $M_\odot$ core will reduce the velocity sufficiently, and suggest that

this situation may arise in a 9 $M_\odot$ star which has lost its hydrogen envelope through a stellar wind. Carbon deflagration models (Chevalier 1980) are also capable of producing sufficiently low velocities.

The constraints imposed by spectral modelling should rapidly become more restrictive in the future. The capability currently exists to perform precise calculations of the atomic physics quantities which are most necessary for a precise determination of the Ni^{56} mass and ejection velocity. These include collision strengths, photoionization crossections of excited states, and electron ionization crossections of the nearly neutral ions of Fe and Co. Additionally extension of the current model to include the effects of a realistic density profile and the existence of scattering lines in the atmosphere should allow the structure of post explosion SNI to be determined in considerable detail.

References

Allen, C. W. 1973 "Astrophysical Quantities," Third Edition. London: Athlone Press.

Andersen, H. H., Sorensen, H., and Vadja, P. 1969 Phys. Rev. 180, 373.

Ardeberg, A., and DeGroot, M., 1973 Astron & Astrophys. 28, 295.

Ardeberg, A., and DeGroot, M. 1974 in C. B. Cosmovici (ed.), "Supernovae and Supernova Remnants" p. 113

Arnett, W. D., and Truran, J. W., 1969, Ap. J. 157, 339.

Arnett, W. D., 1979, Ap J. 230, L37.

Axelrod, T. S., 1978 unpublished.

Baade, W. 1926, Astr. Nachr. 228, 359

Barbon, R., Ciatti, F., and Rosino, L., 1973, Astron. & Astrophys. 25, 241.

Barbon, R., Ciatti, F., and Rosino, L., 1979, Astron. & Astrophys. 72, 287.

Bergeron, J., and Collin-Souffrin, S., 1973, Astron. & Astrophys. 25, 1.

Bless, R. C., and Savage, B. D., 1972, Ap. J. 171, 293.

Bodansky, D., Clayton, D. D., and Fowler, W. A. 1968, Ap. J. Suppl. 16, 299.

Bodenheimer, P. and Ostriker, J. P., 1974, Ap. J. 191, 465.

Borst, L. B., 1950, Phys. Rev. 78, 807.

Branch, D., 1977, MNRAS 179, 401.

Branch, D., 1979, MNRAS 186, 609.

Branch, D., 1980a, Preprint; Workshop on Atomic Physics and Spectroscopy For Supernovae, La Jolla, CA, 1980.

Branch, D., 1980b, Preprint; Workshop on Type I Supernovae, Austin, TX, 1980.

Branch, D., and Bettis, C., 1978, Astron. J. 83, 224.

Branch, D., and Patchett, B., 1973, MNRAS 161, 71.

Branch, D., and Tull, R. G., 1979, Astron. J. 84, 1837.

Burbidge, G. R., Hoyle, F., Burbidge, E. M., Christy, R. F., and Fowler, W. A., 1956, Phys. Rev. 103, 1145.

Bussard, R. W., Ramaty, R., and Drachman, R. J., 1979, Ap. J. 228, 928.

Chevalier, R. A., 1980, Preprint.

Colbert, H. M., 1974, Sandia Laboratories Report SLL-74-0012 (unpublished).

Colgate, S. A., and White, R. H. 1966, Ap. J. 143, 626.

Colgate, S. A., and McKee, C. 1969, Ap. J. 157, 623.

Colgate, S. A., 1974, Ap. J. 187, 321.

Colgate, S. A., Petschek, A. G., and Kriese, J. T., 1980, Preprint.

Dalgarno, A., and McCray, R. A., 1972, Ann. Rev. of Astronomy and Astrophysics 10, 375.

de Vaucouleurs, G., 1977, Nature 266, 126.

de Vaucouleurs, G., 1979, Astron. J. 84, 1270.

Drawin, H-W, 1961, Z Phys. 164, 513.

Fano, U., 1963, Annu. Rev. Nucl. Sci. 13, 1.

Garstang, R. H., Robb, W. D., and Rountree, S. P., 1978, Ap. J. 222, 384.

Gould, R. J., 1972, Physica 60, 145.

Greenstein, J. L. and Minkowski, R., 1973, Ap. J. 182, 225.

Gordon, C., 1975. Ap. J. 198, 765.

Gorenstein, P., Harnden, F. R., and Tucker, W. H., 1974, Ap. J. 192, 661.

Hainebach, K. L., Clayton, D. D., Arnett, W. D., and Woosley, S. E., 1974, Ap. J. 193, 157.

Hansen, J. E., Ziegenbein, B., Lincke, R., and Kelly, H., 1977, J. Phys. B. 10, 37.

Holm, A. V., Wu, C., and Caldwell, J. J., 1974, Publ. Astrom. Soc. Pacific 86, 296.

Hoyle, F., and Fowler, W. A., 1960, Ap. J. 132, 565.

Inokuti, M., 1971, Rev. Mod. Phys. 43, 297.

Inokuti, M., Itikawa, Y., and Turner, J., 1978, Rev. Mod. Phys. 50, 23.

Jacobs, V. L., Davis, J., Rozsnyai, B. F., and Cooper, J., 1979, Lawrence Livermore Laboratory Report UCRL-83752

Kelly, H. P., and Ron, A., 1972, Phys. Rev. A5, 168.

Kelly, H. P., 1980, Workshop on Atomic Physics and Spectroscopy For Supernovae, La Jolla, CA, 1980.

Kirshner, R. P., and Oke, J. B., 1975, Ap. J. 200, 574.

Kirshner, R. P., Arp, H. C., and Dunlap, J. R., 1976, Ap. J. 207, 44.

Kirshner, R. P., Oke, J. B., Penston, M. V. and Searle, L., 1973b, Ap. J. 185, 303.

Kirshner, R. P., Willner, S. P., Becklin, E. E., Neugebauer, G., and Oke, J.B., 1973a, Ap. J. 180, L-97.

Kowal, C. T., 1968, Astron. J. 73, 1021.

Lasher, G., 1975, Ap. J. 201, 194.

Lederer, C. M., Hollander, J. M., and Perlman, I., 1967, "Table of Isotopes", Sixth Edition, New York: J. Wiley and Sons.

Lederer, C. M., and Shirley, V. S. (eds.), 1978. "Table of Isotopes," Seventh Edition. New York: J. Wiley and Sons.

Lee, T. A., Wamsteker, W., Wisniewski, W. Z., and Wdowiak, T. J., 1972, Ap. J., 177, L-59.

Lombardi, G. G., Smith, P. L., and Parkinson, W. H., 1978, Phys. Rev. A-18, 2131.

Lotz, W., 1967, Z. Physik 206, 205.

Lotz, W., 1968, J. Opt. Soc. Am. 58, 915.

Mazurek, T. J. and Wheeler, J. C., 1980, Fund. of Cos. Phys. 5, 193.

McGuire, E. J., 1977, Phys. Rev. A 16, 62.

Meyerott, R. E., 1978, Ap. J. 221, 975.

Meyerott, R. E., 1979, Preprint.

Mihalas, D., 1963, Publ. A.S.P. 75, 256.

Mihalas, D., 1978, "Stellar Atmospheres", San Francisco, Calif: W. H. Freeman.

Morrison, P., and Sartori, L., 1969, Ap. J. 158, 541.

Mott, N. F., and Massey, H. S. W., 1965, "The Theory of Atomic Collisions," 3rd Ed. London: Oxford University Press.

Mustel, E. R., 1975, Soviet Astron. 19, 685.

Mustel, E. R., and Chugai, N. N., 1975, Sov. Astron. 19, 411.

Oemler, A., and Tinsley, B. M., 1979, Astron. J. 84, 985.

Oke, J. B., 1969, Pub. Astron. Soc. Pac. 81, 11.

Opal, C. B., Beaty, E. C., and Peterson, W. K., 1972, Atomic Data 4, 209.

Opal, C. B., Peterson, W. K., and Beaty, E. C., 1971, J. Chem. Phys. 55, 4100.

Osterbrock, D. E., 1974, "Astrophysics of Gaseous Nebulae," San Francisco: W. H. Freeman.

Patchett, B., and Wood, R., 1976, MNRAS 175, 595.

Phillips, M. M., 1979, Ap. J., Suppl. 39, 377.

Platzman, R. L., 1961, Int. J. App. Radiation and Isotopes 10, 116.

Plechaty, E. F., Cullen, D. E., and Howerton, R. J., 1978. Lawrence Livermore Laboratory report UCRL-50400, Vol. 6, Rev. 2.

Pettersson, H., Bergman, O., and Bergman, C., 1964, Arkiv For Fysik 29, 423.

Reilman, R. F., and Manson, S. T., 1978, Phys. Rev. A18, 2124.

Rohrlich, F., and Carlson, B. C., 1954, Phys. Rev. 93, 38.

Rozsnyai, B. F., Jacobs, V. L., and Davis, J., 1979, Lawrence Livermore Laboratory Report UCRL-83526.

Rozsnyai, B. F., 1980. Private communication.

Sandage, A., and Tammann, G. A. 1975, Ap. J. 197, 265.

Seaton, M. J., 1962, in "Atomic and Molecular Processes," D. R. Bates (ed), New York: Academic Press.

Sersic, J. L., Carranza, G., and Pastoriza, M., 1972, Astrophys. Space Sci. 19, 469.

Sobolev, V., 1957, Soviet Astron. 1, 678.

Sugimoto, D., and Nomoto, K., 1980, Space Sci. Rev. 25, 155.

Taam, R. E., 1980, Ap. J. 237, 142.

Tarter, C. B., 1971, Ap. J. 168, 313.

Tarter, C. B., 1979. Private communication.

Tinsley, B. M., 1980, Workshop on Type I Supernovae, Austin, TX.

Van Regemorter, H., 1962, Ap. J. 136, 906.

Van Riper, K., and Arnett, W. D., 1978, Ap. J., 225, L-129.

Weaver, T. A., and Woosley, S. E., 1980, Ann. N. Y. Acad. Sci. 336, 335 (1980).

Weaver, T. A., Axelrod, T. S., and Woosley, S. E. 1980, Workshop on Type I Supernovae, Austin, TX.

Wheeler, J. C., 1978, Ap. J. 225, 212.

Whelan, J. and Iben, I., 1973, Ap. J. 186, 1007.

Whitford, A. E., 1958, Astron. J. 63, 201.

Wilcox, T. P., 1973, Lawrence Livermore Laboratory Report UCID-17106 (unpublished).

Wilson, J. R., 1971, Ap. J. 163, 209.

Woosley, S. E., Arnett, W. D., and Clayton, D. D., 1973, Ap. J. Supp. 26, 231.

Woosley, S. E., Weaver, T. A., and Taam, R. E., 1980, Preprint; Workshop on Type I Supernovae, Austin, TX, 1980.

Appendix. Energy Levels and Radiative Rates

The tables on the following pages list the energy levels and radiative rates used in the numerical calculations. The sources from which the data has been derived are listed below. When more than one source is listed for a given ion, they are listed in order of preference, so that information is incorporated from a source only if it is unavailable from sources listed above it. Unless otherwise noted, energy levels are from C. E. Moore, "Atomic Energy Levels", NBS Circular 467, 1952.

FeI

Forbidden Rates

1. Grevesse, N., Nussbaumer, H., and Swings, J. P., 1971, MNRAS 151, 239.

Allowed Rates

1a. Blackwell, D. E., Ibbetson, P. A., Petford, A. D., and Shallis, M. J., 1979, MNRAS 186, 633.

b. Blackwell, D. E., Petford, A. D., and Shallis, M. J., 1979, MNRAS 186, 657.

2. Huber, M. C. E., and Tubbs, E. F., 1972, Ap. J. 177, 847.

3. Ross, J. E., 1973, Ap. J. 180, 599.

4. May, M., Richter, J., and Wichelmann, J., 1974, Astron. Astrophys. Suppl. 18, 405.

5. Bridges, J. M., and Kornblith, R. L., 1974, Ap. J. 192, 793.

6a. Corliss, C. H., and Tech, J. L., 1968, NBS Monograph 108.

b. Corliss, C. H., and Tech, J. L., 1976, J. Res. Nat. Bur. Stand., A80, 787.

FeII

Forbidden Rates

1. Johansson, S., 1977, Physica Scripta 15, 183.

Allowed Rates

1. Phillips, M., 1979, Ap. J. Suppl. 39, 377.

FeIII

Forbidden Rates

1. Garstang, R. H., 1957, MNRAS 117, 393.

FeV

Energy Levels

1. Reader, J., and Sugar, J., 1975, J. Phys. Chem. Ref. Data, 4, 353.

Forbidden Rates

1. Garstang, R. H., 1957, MNRAS 117, 393.

FeVI

Energy Levels

1. Reader, J., and Sugar, J., 1975, J. Phys. Chem. Ref. Data, 4, 353.

Forbidden Rates

1. Smith, M., and Weise, W., 1973, J. Phys. Chem. Ref. Data, 2, 85.

CoI

Allowed Rates

1. Corliss, C. H., and Bozman, W. R., 1962, NBS Monograph 53.

CoII

Energy Levels

1. Moore, C. E., 1952, "Atomic Energy Levels," NBS Circular 467.

2. Racah, G., and Shadmi, Y., 1959, Bull. Res. Counc. Israel, 8F, 15.

Forbidden Rates

1. Scofield, J., 1979, Private communication.

CoIII

Energy Levels

1. Moore, C. E., 1952, "Atomic Energy Levels," NBS Circular 467.

2. Shadmi, Y., 1962, Bull. Res. Counc. Israel, 10F, 109.

Forbidden Rates

1. Rudzikas, Z. B., 1969, Litov. Fiz. Sb. 9, 433.

Fe I

Desig.	J	E(cm^{-1})	λ(Å)	A(sec^{-1})
a ^{5}D	4.	0.		
	3.	415.933		
			240539.	.0025
	2.	704.003		
			347043.	.0016
	1.	888.132		
			542946.	.0006
	0.	978.074		
a ^{5}F	5.	6928.280		
			14429.7	.0020
			15351.3	.0005
	4.	7376.775		
			13552.3	.0015
			14362.1	.0007
			14982.2	.0008
			222905.	.0036
	3.	7728.071		
			12936.3	.0005
			13672.2	.0017
			14232.9	.0001
			14616.0	.0009
			284588.	.0031
	2.	7985.795		
			13206.7	.0011
			13729.1	.0016
			14266.1	.0008
			387897.	.0017
	1.	8154.725		
			13417.8	.0015
			12918.4	.0002
			13757.8	.0019
			591800.	.0005
a ^{3}F	4.	11976.260		
			8347.56	.0007
			8647.90	.0001
			19804.5	.0094
			21735.7	.0011
			23533.0	.0017
	3.	12560.953		
			8231.56	.0004
			8431.56	.0001
			19284.2	.0017
			20686.0	.0016
			21851.2	.0035

	2.	12968.573		
			8151.33	.0002
			19076.9	.0001
			20063.7	.0017
			20767.8	.0052
a ^5P	3.	17550.210		
			5696.36	.12
			5834.64	.090
			5934.41	.039
			5999.99	.0085
	2.	17727.017		
			5639.54	.14
			5775.04	.0096
			5872.77	.034
			5936.99	.054
			5968.87	.024
	1.	17927.411		
			5708.96	.15
			5804.44	.089
			5867.17	.021
a ^3P	2.	18378.215		
			5439.71	.0053
			5565.67	.36
			5656.39	.0018
			5715.94	.038
	1.	19552.493		
			5303.99	.458
			5356.32	.001
			5382.25	.079
	0.	20037.86		
			5220.55	.57
z $^7D^o$	5.	19350.894		
			5166.29	1.45e+3
			8047.60	2.22e+2
	4.	19562.457		
			5110.41	4.93e+3
			7912.87	1.68e+2
	3.	19757.040		
			5060.08	5.66e+1
			5168.90	3.83e+3
			5247.06	3.92e+2
			8075.13	1.27e+2
	2.	19912.511		
			5204.59	2.29e+3
			5254.96	8.32e+2
	1.	20019.648		
			5225.53	1.32e+3
			5250.21	9.30e+2
a ^3H	6.	19390.197		
	5.	19621.036		

	4.	19788.280		
			5052.09	.0082
			5160.56	.0015
b ^{3}F	4.	20641.144		
			4843.34	.415
			4942.94	.077
	3.	20874.521		
			4989.19	.039
			4886.56	.229
			4956.35	.079
	2.	21039.021		
			4847.58	.025
			4916.25	.092
			4961.18	.045
a ^{3}G	5.	21715.770		
			6760.61	.126
			6972.07	.026
			10264.64	.011
	4.	21999.167		
			4544.35	.007
			4631.93	.002
			6633.48	.007
			6836.94	.072
			7005.24	.032
			9974.41	.015
	3.	22249.461		
			4578.83	.003
			4640.05	.001
			6721.88	.004
			6884.49	.028
			7008.89	.022
			10318.68	.012
			10771.88	.008
z ^{7}F^o	6.	22650.427		
			6358.69	4.32e+2
	5.	22845.880		
			4375.93	2.95e+4
			6280.62	6.31e+2
	4.	22996.686		
			4347.24	1.23e+2
			4427.31	3.42e+4
			6400.32	6.52e+2
	3.	23110.948		
			4461.65	2.95e+4
			6498.95	4.51e+2
	2.	23192.508		
			4389.25	1.81e+3
			4445.48	2.45e+2
			4482.17	2.10e+4
			6574.24	3.54e+2

			6648.12	1.48e+2
	1.	23244.847		
			4435.15	4.72e+3
			4471.68	1.13e+2
			4489.74	1.19e+4
			6625.04	1.01e+2
	0.	23270.392		
b ^3P	2.	22838.360		
			4458.57	.033
			9203.80	.013
			18905.04	.057
			19559.00	.031
			20357.10	.007
	1.	22946.860		
			4494.56	.048
			19917.06	.055
	0.	23051.790		
			4510.63	.101
			19509.23	.049
z $^7P^o$	4.	23711.467		
			4216.19	1.84e+4
			4291.48	3.84e+3
			5956.70	5.19e+2
	3.	24180.876		
			4134.34	1.98e+3
			4206.70	5.26e+3
			4258.32	2.54e+3
			5949.35	3.29e+2
	2.	24506.928		
			4149.77	7.23e+2
			4199.97	5.87e+2
			4232.73	8.79e+2
b ^3G	5.	23783.654		
			22754.95	.028
			24016.84	.020
	4.	24118.854		
			23085.35	.017
	3.	24338.805		
			21969.47	.031
c ^3P	2.	24335.804		
	1.	24772.060		
			4153.71	.016
	0.	25091.62		
			13954.46	.020
a ^1G	4.	24574.690		
			7935.31	.064
z $^5D^o$	4.	25900.002		
			3859.91	9.70e+6
			3922.91	1.08e+6
			5269.54	1.27e+6

			5397.13	2.59e+5
			5501.47	3.46e+4
			7180.02	1.51e+3
	3.	26140.193		
			3824.45	2.83e+6
			3886.28	5.30e+6
			3930.30	2.00e+6
			5328.04	1.15e+6
			5429.70	4.27e+5
			5506.78	5.02e+4
	2.	26339.708		
			3856.37	4.64e+6
			3899.71	2.58e+6
			3927.92	2.80e+6
			5371.49	1.05e+6
			5446.92	6.65e+5
			5497.52	6.25e+4
	1.	26479.393		
			3878.57	8.91e+6
			3906.48	8.33e+5
			3920.26	2.60e+6
			5405.78	1.09e+6
			5455.61	5.81e+5
	0.	26550.495		
			3895.66	9.40e+6
			5434.53	1.71e+6
b ^3H	6.	26105.95		
			22771.89	.013
	5.	26351.09		
			21567.6	.013
	4.	26627.64		
			21599.52	.022
			22834.31	.010
a ^3D	3.	26225.03		
			3812.07	.021
			5304.06	.175
			7016.21	.033
			7316.44	.020
			11524.46	.068
			11764.24	.015
	2.	26623.73		
			3856.97	.011
			5290.75	.222
			5363.91	.020
			5412.97	.022
			7321.22	.011
			11237.03	.025
			12124.49	.020
	1.	26406.49		
			3917.64	.016

			3931.49	.011
			5427.17	.170
			5477.40	.082
			7439.58	.016
			14586.03	.014
z $^5F^o$	5.	26874.562		
			3719.94	1.63e+7
			5012.07	5.50e+4
			5127.36	1.14e+4
			6710.31	3.78e+2
	4.	27166.837		
			3679.92	1.38e+6
			3737.13	1.42e+7
			4939.69	1.39e+4
			5051.64	4.66e+4
			5142.93	4.23e+4
			6581.22	2.97e+2
	3.	27394.703		
			3649.30	1.30e+5
			3705.57	3.22e+6
			3745.56	1.15e+7
			4994.13	3.18e+4
			5083.34	4.06e+4
			5150.84	3.85e+4
	2.	27559.598		
			3683.06	4.60e+5
			3722.56	4.97e+6
			3748.26	9.15e+6
			5041.07	7.51e+4
			5107.45	4.19e+4
			5151.92	2.40e+4
	1.	27666.362		
			3707.82	8.89e+5
			3733.32	7.29e+6
			3745.90	7.33e+6
			5079.74	5.19e+4
			5123.72	7.24e+4
a ^1P	1.	27543.00		
			5111.78	.023
			5156.32	.011
a ^1D	2.	28604.61		
			6231.27	.166
			6393.71	.093
			17337.56	.027
			17670.05	.012
			23419.34	.026
a ^1H	5.	28819.98		
			14072.31	.033
			14657.01	.015
z $^5P^o$	3.	29056.341		

			3440.6	1.53e+7
			3490.6	4.40e+6
			3526.0	6.83e+5
			4687.3	1.27e+3
			8688.6	1.41e+6
			8824.2	7.68e+5
			9362.4	2.77e+4
	2.	29469.033		
			3441.0	1.10e+7
			3475.5	7.30e+6
			3497.8	1.98e+6
			4598.4	1.03e+3
			4690.4	1.89e+3
			8387.8	1.02e+6
			8514.1	2.44e+5
			8661.9	9.17e+5
			9013.9	2.33e+4
	1.	29732.749		
			3443.9	6.81e+6
			3465.9	9.28e+6
			3476.7	4.21e+6
			8327.1	1.78e+6
			8468.4	5.56e+5
			8804.6	6.77e+4
a ^{1}I	6.	29313.04		
			10075.00	.079
			10341.96	.052
b ^{3}D	1.	29320.05		
			3516.17	.102
			3527.33	.089
			10235.17	.030
	2.	29356.78		
			3454.33	.021
			3489.06	.083
			3511.63	.070
			9106.16	.030
	3.	29371.86		
			3403.64	.184
			3452.53	.052
			3487.23	.039
			9093.67	.037
b ^{1}G	4.	29798.96		
			10916.64	.186
			11202.12	.092
1S	0.	30694.8		
			8974.84	.82
z $^{3}F^{o}$	4.	31307.272		
			3193.23	7.79e+5
			3236.22	5.39e+5
			4100.74	2.92e+4

			4177.59	3.72e+4
			5171.60	4.82e+5
			5332.90	6.58e+4
			9372.90	3.78e+4
	3.	31805.097		
			3143.24	3.38e+4
			3184.90	5.22e+5
			3214.40	7.78e+5
			4092.51	3.35e+3
			4152.17	3.24e+4
			4197.10	5.84e+3
			5041.76	1.95e+5
			5194.94	4.60e+5
			5307.36	6.50e+4
			9146.11	5.26e+4
	2.	32134.014		
			3151.87	8.94e+4
			3180.76	3.93e+5
			4096.22	1.04e+4
			4139.93	1.83e+4
			5107.64	2.53e+5
			5216.28	5.96e+5
			9010.55	6.02e+4
z $^3D^o$	3.	31322.639		
			3191.66	5.39e+5
			3234.61	3.98e+5
			3265.05	3.41e+5
			4174.92	5.87e+4
			4237.08	2.22e+3
			5167.49	2.47e+6
			5328.53	6.11e+5
			7723.20	1.49e+4
			9359.42	3.53e+4
	2.	31686.377		
			3226.71	3.77e+4
			3246.01	5.89e+5
			4172.75	6.46e+4
			5227.19	3.96e+6
			5341.03	6.73e+5
			8239.13	2.77e+3
			9246.54	5.66e+4
	1.	31937.350		
			3200.79	1.85e+5
			3229.12	6.16e+5
			4173.92	6.70e+4
			4203.57	4.17e+4
			5270.36	3.11e+6
			9173.12	8.20e+4
c ^3F	4.	32873.68		
	3.	33412.78		

	2.	33765.33		
y $^5D^o$	4.	33095.96		
			3059.09	3.03e+7
			3820.43	6.68e+7
			3887.05	3.52e+6
			3940.88	1.20e+5
			4733.60	6.91e+4
			6430.85	2.43e+5
	3.	33507.14		
			2983.57	2.80e+7
			3021.07	4.56e+7
			3047.61	2.84e+7
			3825.88	5.98e+7
			3878.02	7.72e+6
			3917.18	4.35e+5
			4643.22	8.01e+2
			6265.14	1.19e+5
			6335.34	1.60e+5
			6608.03	2.56e+3
	2.	33801.60		
			2994.43	3.17e+7
			3037.39	3.47e+7
			3834.22	4.53e+7
			3872.50	1.05e+7
			3898.01	1.59e+5
			4798.74	4.10e+3
			6151.62	1.69e+4
			6219.29	1.50e+5
			6297.80	5.98e+4
			6481.88	3.48e+4
			7016.08	2.10e+4
			9118.89	3.75e+5
			9210.03	1.76e+5
	1.	34017.13		
			3000.95	6.42e+7
			3017.63	6.82e+6
			3025.84	3.48e+7
			3840.44	4.70e+7
			3865.53	1.55e+7
			4749.58	3.43e+3
			6137.00	1.16e+5
			6213.44	1.92e+5
			6392.55	1.89e+4
			7151.50	4.88e+4
			8943.00	1.40e+5
			9117.10	1.41e+5
	0.	34121.62		
			3008.14	1.07e+8
			3849.97	6.06e+7
			6173.34	1.92e+5

			6861.93	6.75e+4
y $^5F^o$	5.	33695.42		
			2966.90	2.72e+7
			3734.87	9.02e+7
			3798.51	3.23e+6
			4602.94	3.44e+5
			6988.53	3.42e+3
	4.	34039.54		
			2936.91	1.43e+7
			2973.24	1.83e+7
			3687.46	8.01e+6
			3749.49	7.64e+7
			3799.55	7.32e+6
			4531.15	3.22e+5
			4654.50	1.05e+5
			6062.89	1.84e+3
			6933.63	1.11e+4
			7461.53	1.63e+4
	3.	34328.78		
			2912.16	3.32e+6
			2947.88	1.87e+7
			2973.13	1.35e+7
			3709.25	1.56e+7
			3758.24	6.34e+7
			3795.00	1.15e+7
			4592.65	2.55e+5
			4680.30	7.74e+3
			7430.56	2.28e+4
	2.	34547.24		
			2929.01	5.32e+6
			2953.94	1.89e+7
			2970.11	1.08e+7
			3727.62	2.25e+7
			3763.79	5.44e+7
			3787.88	1.29e+7
			4547.02	1.51e+4
			4632.92	9.85e+4
	1.	34692.17		
			2941.34	7.08e+6
			2957.37	1.77e+7
			2980.26	1.16e+7
			3743.36	2.60e+7
			3767.19	6.40e+7
			4602.00	7.26e+4
z $^3P^o$	2.	33946.97		
			2981.45	6.54e+6
			3007.28	2.73e+6
			3024.03	4.88e+6
			3812.97	7.92e+6
			3850.82	1.66e+6

			3876.04	2.03e+5
			4674.66	1.25e+3
			4765.48	7.23e+3
			6163.54	6.39e+3
			6240.66	1.50e+4
			6421.36	4.40e+5
			6945.21	1.85e+5
			8999.56	2.00e+6
			9088.33	5.90e+5
	1.	34362.89		
			2986.46	2.19e+5
			2994.50	1.49e+6
			3790.09	2.68e+6
			3814.53	8.81e+5
			4672.84	6.27e+3
			6082.71	1.62e+4
			6254.26	2.06e+5
			6750.15	1.44e+5
			6978.86	2.88e+5
			8674.75	9.79e+5
			8757.19	8.78e+5
			8838.43	7.00e+5
	0.	34535.64		
			2969.36	3.66e+6
			3786.68	2.77e+6
			6663.45	6.04e+5
			8611.81	1.98e+6
b ^1D_o	2.	34636.82		
z ^5G	6.	34843.98		
			3581.20	1.02e+8
	5.	34782.45		
			2874.17	9.17e+5
			3589.11	3.61e+5
			3647.84	2.92e+7
			4383.55	4.89e+7
			6494.98	8.77e+5
			6593.88	5.18e+4
			9089.41	2.41e+5
	4.	35257.35		
			2835.46	3.76e+5
			2869.31	1.06e+6
			3528.94	4.74e+3
			3585.71	3.75e+6
			3631.47	5.17e+7
			4294.13	3.93e+6
			4404.75	2.70e+7
			6393.60	6.15e+5
			6462.73	5.61e+4
			6839.83	7.08e+3
			8713.19	4.91e+4

			8975.41	1.36e+5
	3.	35611.65		
			2807.25	1.08e+5
			2840.42	5.30e+5
			2863.86	8.63e+5
			3540.71	1.78e+5
			3585.32	1.23e+7
			3618.77	5.78e+7
			4229.76	3.14e+4
			4337.05	1.33e+6
			4415.12	1.38e+7
			6318.02	2.81e+5
			8868.42	7.13e+4
	2.	35856.42		
			2820.80	1.01e+5
			2858.90	3.92e+5
			3554.12	1.36e+6
			3586.99	1.61e+7
			3608.86	8.14e+7
			4291.47	3.02e+5
			4367.91	1.97e+5
z $^3G^o$	5.	35379.24		
			2825.69	3.53e+5
			3513.82	3.41e+6
			3570.10	6.77e+7
			4271.76	2.23e+7
			6252.56	3.36e+5
			6344.15	1.94e+4
			8621.61	6.14e+4
	4.	35767.59		
			2795.01	1.95e+5
			2827.89	1.95e+5
			3466.50	3.19e+5
			3521.26	9.12e+6
			3565.38	4.13e+7
			4202.03	9.70e+6
			4307.90	3.73e+7
			6191.56	6.45e+5
			6256.37	5.72e+4
			6609.12	3.31e+4
			7261.02	1.10e+4
			8582.27	9.90e+4
	3.	36079.40		
			2803.17	7.70e+4
			2826.00	5.74e+4
			3483.01	3.38e+5
			3526.17	5.10e+6
			3558.52	1.58e+7
			4147.67	6.36e+5
			4250.79	1.11e+7

			4325.76	5.46e+7
			6136.62	1.17e+6
			6475.63	3.28e+4
			6575.02	4.20e+4
			7228.69	2.21e+4
			8515.08	2.25e+5
y $^5F^o$	4.	36686.20		
			2756.27	3.41e+6
			3359.49	2.09e+5
			3410.91	1.77e+5
			3452.28	1.72e+6
			4045.82	7.93e+7
			4143.87	1.25e+7
			5916.25	6.44e+4
			6230.73	8.58e+5
			6322.69	8.35e+4
			6677.99	7.66e+5
			6806.85	2.08e+4
			7748.28	4.71e+5
	3.	37162.77		
			2690.07	4.54e+5
			2720.52	9.27e+4
			2742.02	5.62e+5
			3396.39	3.12e+4
			3969.26	2.14e+7
			4063.60	5.87e+7
			4132.06	1.30e+7
			5322.05	1.33e+5
			6137.70	1.05e+6
			6200.32	1.00e+5
			6592.92	6.43e+5
			6703.57	2.31e+4
			7664.30	5.21e+5
	2.	37521.19		
			2694.22	6.47e+4
			2715.32	1.30e+5
			2728.97	2.03e+5
			3355.52	3.08e+4
			3384.77	2.64e+4
			4005.24	2.43e+7
			4071.74	7.62e+7
			6005.53	2.59e+4
			6065.49	1.22e+6
			6546.24	7.41e+5
			7583.8	4.78e+5
y $^5P^o$	3.	36787.00		
			2719.03	6.93e+7
			2750.14	2.00e+7
			3401.52	1.43e+6
			3442.67	5.83e+5

			3473.50	9.75e+4
			4032.63	3.62e+5
			4130.04	3.88e+4
			5202.34	8.64e+5
			5250.65	3.96e+5
			5436.59	2.34e+4
	2.	37157.59		
			2720.90	5.29e+7
			2742.41	3.14e+7
			2756.33	1.63e+7
			3396.98	9.57e+5
			3446.95	1.22e+5
			4064.45	1.36e+5
			5098.70	7.54e+5
			5145.40	7.43e+4
			5198.71	5.77e+5
	1.	37409.58		
			2723.58	4.13e+7
			2737.31	4.71e+7
			2744.07	2.40e+7
			3397.64	8.77e+5
			3417.27	5.00e+5
			4090.33	1.39e+4
			5079.23	1.11e+6
			5131.48	3.70e+5
y $^3D^o$	3.	38175.38		
			2618.71	8.65e+5
			2647.56	8.86e+5
			2667.91	2.89e+5
			3283.43	3.09e+4
			3311.45	8.96e+3
			3815.84	8.93e+7
			3902.95	2.19e+7
			3966.06	1.72e+6
			4889.01	6.84e+4
			5049.82	1.28e+6
			5701.55	4.00e+5
			6180.21	7.11e+4
			6518.38	8.99e+4
			7112.18	4.17e+4
			7223.67	1.80e+5
			8365.64	1.61e+5
	2.	38678.07		
			2612.77	1.02e+6
			2632.60	1.26e+6
			2645.42	5.60e+5
			3827.83	1.06e+8
			3888.52	2.47e+7
			4771.70	5.43e+4
			4817.77	3.85e+4

		4924.78	2.39e+5
		5615.30	4.31e+5
		6085.27	4.41e+4
		6311.51	6.35e+4
		6355.04	1.89e+5
		7189.17	1.32e+5
		8293.53	1.84e+5
1.	38995.76		
		2610.75	9.77e+5
		2623.37	1.50e+6
		2629.58	8.38e+5
		3223.84	4.43e+6
		3241.50	3.73e+4
		3841.05	1.43e+8
		4745.13	3.10e+4
		4848.88	4.92e+4
		5141.75	7.26e+5
		5273.38	1.12e+6
		5567.40	2.41e+5
		6229.53	1.43e+5
		6270.24	2.24e+5
		7190.13	1.10e+5
		7941.09	2.31e+5
		8080.67	1.69e+5

Fe II

Desig.	J	E(cm^{-1})	λ(A)	A(sec^{-1})
a ^{6}D	4.5	0.		
	3.5	384.77		
			259896.	.0021
	2.5	667.64		
			353519.	.0016
	1.5	862.63		
			512847.	7.2e-4
	0.5	977.03		
			874126.	1.9e-4
a ^{4}F	4.5	1872.60		
	3.5	2430.08		
			179379.	.0058
	2.5	2837.94		
			245182.	.0039
	1.5	3117.48		
			357731.	.0014
a ^{4}D	3.5	7955.24		
			12570.3	.0054
			13209.2	.0015
			13721.9	9.2e-4
	2.5	8391.92		
			12488.8	4.7e-4
			12946.2	.0022
			13281.5	.0014
			229001.	.0026
	1.5	8680.47		
			12791.3	.0029
			12981.2	.0013
			12524.9	7.3e-4
			12706.9	.0039
			346560.	.0014
	0.5	8846.76		
			601359.	3.8e-4
a ^{4}P	2.5	13474.43		
			7637.538	.0039
			8616.952	.017
			9051.948	.0042
	1.5	13673.21		
			7686.938	.0040
			8891.912	.010
			9226.617	.006
			9470.935	.0017
	0.5	13904.87		
			7665.302	.0036

			7733.157	.0013
			9033.496	.0075
			9267.563	.0099
a ^{2}G	4.5	15844.71		
			7155.157	.15
			7452.539	.048
	3.5	16369.39		
			6896.173	.0052
			7172.002	.056
			7388.176	.043
a ^{2}P	1.5	18360.65		
			6440.400	.023
			6558.497	.016
			10028.641	.0034
	0.5	18886.75		
			9795.159	.0034
a ^{2}H	5.5	20340.36		
	4.5	20805.83		
a ^{2}D	2.5	20516.98		
			5527.340	.27
			5654.856	.030
			5745.698	.013
	1.5	21308.08		
			5412.654	.27
			5495.824	.14
b ^{4}P	2.5	20830.52		
			4889.616	.36
			5006.624	.027
			5273.346	.37
			5433.129	.11
			5556.288	.022
			7764.683	.029
			8037.251	.010
			8228.104	.008
	1.5	21812.04		
			4728.068	.48
			4772.062	.026
			4798.274	.082
			5158.001	.30
			5268.874	.19
			5347.653	.057
			7613.15	.012
	0.5	22409.82		
			4639.667	.49
			4664.440	.15
			5107.942	.24
			5181.948	.34
			7370.94	.018
a ^{4}H	6.5	21251.55		
			5158.777	.44

	5.5	21430.39		
			5111.627	.10
			5261.621	.31
	4.5	21581.64		
			4632.271	.0022
			5072.392	.022
			5220.059	.11
			5333.646	.26
	3.5	21711.89		
			5184.788	.021
			5296.829	.091
			5376.452	.26
b ^{4}F	4.5	22637.19		
			4416.266	.46
			4492.634	.060
			4814.534	.40
			4947.373	.050
			6809.226	.025
	3.5	22810.33		
			4382.742	.055
			4457.945	.29
			4514.900	.066
			4774.718	.13
			4905.339	.22
			5005.512	.071
			6729.856	.017
	2.5	22939.35		
			4432.447	.054
			4488.749	.15
			4528.383	.046
			4745.480	.013
			4874.485	.17
			4973.388	.14
			5043.520	.065
			6872.175	.022
	1.5	23031.30		
			4470.294	.029
			4509.602	.058
			4533.003	.016
			4852.730	.022
			4950.744	.17
			5020.233	.18
			6966.309	.026
			7047.990	.016
a ^{6}S	2.5	23317.60		
			4287.394	1.12
			4359.333	.82
			4413.782	.58
			4452.098	.37
			4474.904	.18

a ^4G	5.5	25428.80		
			4243.969	.90
			4346.852	.21
	4.5	25805.32		
			3874.071	.014
			4177.196	.14
			4276.829	.65
			4352.778	.31
	3.5	25981.65		
			3905.626	.0080
			4146.649	.0087
			4244.813	.25
			4319.619	.53
			4372.427	.28
	2.5	26055.40		
			4231.554	.024
			4305.890	.31
			4358.360	.73
b ^2P	1.5	25787.60		
			5746.966	.37
			5483.90	.015
			5901.26	.04
	0.5	26932.74		
			5477.242	.44
			5527.609	.12
b ^2H	5.5	26170.19		
			4114.48	.045
			4211.1	.024
			9682.13	.013
	4.5	26352.80		
			10013.9	.01
a ^2F	3.5	27314.93		
			5163.952	.32
			5283.109	.14
			8715.84	.052
	2.5	27620.39		
			8885.66	.012
b ^2G	4.5	30388.55		
			6873.87	.098
			7131.13	.011
			9949.32	.021
	3.5	30764.46		
			6944.91	.087
			6700.68	.012
			10038.8	.019
b ^4D	0.5	31368.45		
			3289.457	.22
			3504.019	.52
			3538.688	.40
			5649.661	.16

			3277.12	.041
			5586.9	.02
	1.5	31364.47		
			3277.548	.16
			3455.111	.36
			3504.511	.21
			3539.190	.38
			3289.89	.061
			4351.80	.014
			5725.92	.039
			5650.94	.074
			5588.15	.072
			9491.4	.021
	2.5	31387.98		
			3254.242	.12
			3387.092	.20
			3452.306	.37
			3501.626	.34
			5580.821	.13
			3224.54	.046
			3275.02	.056
			4266.34	.024
			4402.6	.013
			5718.3	.066
			9469.8	.030
	3.5	31483.20		
			3175.381	.22
			3376.198	.73
			3440.990	.24
			5551.310	.13
			3244.18	.029
			3214.67	.069
			4329.43	.017
			5613.3	.073
			9385.3	.055
b ^{2}F	2.5	31811.87		
			6473.86	.063
			6261.2	.014
			9083.5	.03
	3.5	31999.12		
			6188.55	.13
			6396.30	.045
			8574.7	.031
a ^{2}I	6.5	32875.63		
			5870.0	.14
			7974.8	.069
			8734.3	.039
			8600.5	.097
	5.5	32909.87		
			6043.9	.11

			8259.5	.06
			8825.3	.038
			8708.4	.038
c ^{2}G	4.5	33466.50		
			5673.2	.30
			5847.0	.033
			7719.9	.029
			8305.4	.15
			8411.7	.019
			9380.9	.07
			9231.1	.21
	3.5	33501.32		
			5835.4	.32
			8199.2	.019
			8387.7	.15
			8480.2	.10
			9465.3	.065
			9351.1	.10
			9202.2	.013
b ^{2}D	1.5	36126.41		
			5060.1	.63
			5799.2	.081
			5627.5	.15
			6746.7	.056
			6404.8	.062
			9670.4	.075
	2.5	36252.96		
			5027.8	.087
			4898.7	.82
			5587.5	.036
			5756.8	.018
			6353.1	.17
			6689.4	.043
			6482.5	.042
			6922.8	.01
			9553.1	.022
a ^{2}S	0.5	37227.32		
			5982.8	.25
			6280.1	.17
			6485.4	.73
			6747.1	.20
			8739.6	.23
			9711.7	.23
c ^{2}D	2.5	38164.24		
			4082.0	.033
			4479.2	.24
			5048.3	.42
			5186.1	.11
			5767.7	.082
			6511.2	.16

			6566.3	.022
			8077.9	.021
	1.5	38214.50		
			4576.2	.48
			5172.4	.21
			5035.4	.11
			5913.1	.09
			6094.8	.047
			6544.4	.19
			6584.1	.11
			8861.3	.013
			8044.8	.03
			9435.8	.045
z ^{6}Do	4.5	38459.0		
			2599.40	2.66e+8
			2625.67	4.03e+7
			2732.45	1.82e+4
			3277.34	2.20e+5
	3.5	38660.0		
			2611.87	1.40e+8
			2585.88	8.62e+7
			2631.32	5.89e+7
			2759.33	2.18e+4
			2717.51	2.71e+4
			2790.75	1.90e+3
			3302.86	1.92e+4
			3255.88	2.49e+5
			3969.40	5.67e+3
			2611.9	6.56e+7
			6516.1	1.30e+4
			5607.12	2.53e+2
			6239.36	6.17e+2
	2.5	38859.0		
			2617.62	5.62e+7
			2598.37	2.73e+8
			2631.05	8.82e+7
			2775.34	1.41e+4
			2797.05	1.21e+3
			3312.67	2.16e+3
			3281.29	2.11e+5
			3234.92	3.52e+3
			3969.38	1.44e+3
			3938.29	4.63e+3
			5864.54	1.55e+2
			5545.25	7.91e+0
			6229.34	4.33e+2
			6432.67	6.15e+3
	1.5	39013.3		
			2620.41	4.32e+6
			2607.08	2.04e+8

			2628.29	1.01e+4
			3313.98	1.78e+4
			3295.81	1.53e+5
			3264.75	1.80e+4
			3981.60	2.58e+1
			3945.20	3.39e+3
			3914.49	2.67e+3
			6021.17	7.29e+1
			5811.92	2.06e+1
			5498.19	4.69e+1
			6219.53	2.11e+2
			6369.42	2.98e+3
	0.5	39109.3		
			2621.67	7.34e+7
			2613.82	2.56e+8
			3303.46	1.40e+5
			3285.41	4.36e+4
			3966.43	2.86e+1
			3930.32	5.94e+3
			5986.54	5.48e+1
			5779.65	6.90e+1
			6217.94	6.69e+1
z ^{6}Fo	5.5	41968.1		
			2382.04	3.81e+8
			4825.71	2.39e+2
			4867.73	2.57e+1
			4903.85	6.51e+0
			5171.62	1.28e+3
			6044.53	5.27e+1
			6185.34	2.77e+1
	4.5	42114.8		
			2395.63	3.43e+8
			2373.74	4.93e+7
			4833.21	4.32e+2
			4868.81	1.17e+2
			5178.71	1.22e+2
			5132.67	1.83e+3
			6129.71	1.77e+2
			5991.39	2.45e+3
			6196.71	2.14e+1
	3.5	42237.0		
			2404.88	2.75e+8
			2388.63	1.11e+8
			2366.87	2.47e+6
			2953.77	2.95e+6
			2511.37	2.09e+5
			3475.74	1.38e+4
			4670.16	3.33e+3
			4839.99	3.64e+2
			4870.71	6.85e+1

		5180.52	3.65e+0
		5146.12	2.08e+3
		5100.66	9.45e+2
		5284.10	2.98e+4
		6150.10	1.83e+2
		6084.10	1.75e+3
		6178.13	1.04e+1
2.5	42334.9		
		2410.52	2.05e+8
		2399.24	1.68e+8
		2383.06	1.15e+7
		2970.51	2.29e+6
		2531.08	4.26e+4
		2505.21	4.25e+5
		3487.98	1.52e+4
		3463.96	6.71e+3
		4871.26	3.39e+3
		4648.92	1.78e+3
		4847.61	1.40e+2
		5178.95	4.65e+1
		5154.40	1.66e+3
		5120.34	1.25e+3
		5256.92	1.72e+4
		6141.01	1.09e+2
		6113.32	1.01e+3
1.5	42401.3		
		2413.31	1.31e+8
		2406.66	2.18e+8
		2395.42	3.41e+7
		2979.35	1.46e+6
		2526.83	3.77e+5
		3508.20	1.08e+4
		3479.91	1.44e+4
		3456.00	1.40e+3
		5000.73	2.26e+3
		4855.54	3.31e+3
		4634.60	3.31e+2
		5161.18	1.06e+3
		5136.79	1.45e+3
		5238.61	4.20e+3
		6116.04	4.46e+2
0.5	42439.9		
		2411.06	3.08e+8
		2404.43	7.60e+7
		2975.93	8.43e+5
		2961.27	8.32e+5
		2542.32	3.11e+5
		3503.47	2.37e+4
		3475.25	5.02e+3
		4991.10	5.09e+3

			4846.46	1.08e+3
			5150.93	2.13e+3
z ^{6}Po	3.5	42658.2		
			2343.50	2.35e+8
			2364.83	1.01e+8
			2380.76	2.87e+7
			2451.10	1.79e+6
			2485.07	2.51e+5
			2880.75	6.34e+6
			2917.46	6.93e+5
			3425.58	2.00e+4
			4580.05	1.32e+4
			4993.35	1.79e+4
			5036.91	1.89e+3
			5169.02	6.82e+5
			5932.05	3.67e+2
	2.5	43238.6		
			2332.80	1.86e+8
			2348.30	1.60e+8
			2359.11	6.92e+7
			2449.73	8.66e+5
			2868.87	2.69e+6
			2892.83	6.81e+5
			3381.36	8.46e+3
			3358.78	2.97e+3
			4665.80	1.81e+3
			4461.42	7.36e+3
			4893.81	7.88e+3
			5018.43	1.76e+6
			5793.16	1.86e+2
	1.5	43621.0		
			2327.39	1.04e+8
			2338.01	1.75e+8
			2344.28	1.42e+8
			2861.17	6.01e+5
			3364.21	1.22e+3
			3338.19	1.30e+3
			3316.18	3.47e+2
			4713.18	6.10e+2
			4583.99	6.91e+3
			4386.57	7.72e+2
			4923.91	1.69e+6
			5691.37	2.70e+1
z ^{4}Fo	4.5	44232.5		
			2260.08	2.92e+6
			2279.92	4.35e+6
			2360.00	3.30e+7
			2391.48	3.07e+6
			2755.73	2.53e+8
			3521.63	1.32e+3

		3587.95	2.16e+1
		4384.33	8.51e+3
		4413.60	2.85e+3
		4439.13	1.17e+2
		4629.34	9.84e+4
		4666.75	1.14e+4
		5316.62	2.41e+5
		5425.26	6.53e+3
		5477.67	3.77e+1
		5534.85	1.81e+4
		5591.38	3.46e+2
		5909.37	1.78e+2
		7841.40	1.97e+3
3.5	44753.8		
		2253.13	3.94e+6
		2267.58	3.09e+6
		2362.02	1.84e+7
		2331.31	1.89e+7
		2385.00	3.85e+6
		2749.32	2.47e+8
		2716.69	5.79e+6
		3196.07	1.00e+6
		3522.05	8.65e+1
		3458.13	2.25e+3
		4178.85	1.69e+5
		4314.31	1.23e+4
		4338.69	2.61e+3
		4555.88	1.24e+5
		4520.22	3.32e+4
		4582.83	1.99e+4
		4663.70	6.07e+3
		5275.99	1.89e+5
		5325.55	1.22e+4
		5346.56	1.53e+2
		5432.97	5.02e+3
		5834.93	5.61e+1
		5732.72	2.37e+2
		7479.70	3.18e+3
		7533.37	4.64e+2
2.5	45079.9		
		2250.93	2.89e+6
		2236.69	6.26e+4
		2260.86	1.57e+6
		2366.59	1.54e+7
		2343.96	2.02e+7
		2382.36	3.73e+6
		2746.48	2.28e+8
		2724.88	2.92e+7
		2692.83	1.33e+4
		3183.11	5.89e+5

			3163.09	1.40e+5
			3482.05	8.96e+2
			3741.56	2.51e+3
			4296.56	8.31e+4
			4122.65	3.85e+4
			4278.15	7.82e+3
			4515.33	1.19e+5
			4489.17	1.74e+4
			4534.16	1.87e+4
			5234.62	2.03e+5
			5254.92	1.68e+4
			5181.97	3.69e+2
			5725.95	1.82e+2
			5627.49	8.81e+2
			7289.05	3.39e+3
	1.5	45289.8		
			2250.18	1.25e+6
			2255.99	4.84e+5
			2370.50	2.10e+7
			2354.89	1.61e+7
			2743.19	2.07e+8
			2730.73	5.00e+7
			2709.38	6.55e+5
			3185.32	1.72e+5
			3161.98	1.67e+5
			3142.22	7.90e+3
			3786.36	2.54e+2
			3712.39	3.11e+2
			4369.40	2.14e+4
			4258.14	2.97e+4
			4087.27	3.15e+3
			4491.40	1.06e+5
			4472.92	4.08e+3
			5197.56	2.57e+5
			5445.97	7.24e+2
			5126.19	1.75e+1
			5657.92	1.61e+3
			7181.21	2.81e+3
z ^{4}Do	3.5	44446.9		
			2249.18	1.22e+7
			2268.82	2.75e+6
			2348.1	7.90e+7
			2379.3	1.90e+7
			2402.60	1.44e+6
			2739.6	2.40e+8
			2772.72	4.22e+6
			3227.8	6.70e+6
			4177.7	4.56e+3
			4372.2	1.58e+3
			4233.2	5.60e+5

		4397.37	2.60e+1
		4583.9	3.20e+5
		4620.5	1.80e+4
		4648.23	4.23e+2
		4731.4	2.50e+4
		5362.9	1.00e+5
		5414.1	1.30e+4
		5435.79	2.35e+2
		7655.5	1.83e+3
		7711.7	2.17e+4
2.5	44784.8		
		2251.55	4.08e+6
		2265.99	4.73e+6
		2360.29	7.10e+7
		2383.24	2.50e+7
		2399.23	1.89e+6
		2714.41	6.40e+7
		2746.98	1.69e+8
		2768.94	1.82e+7
		3213.31	5.30e+6
		3192.92	1.40e+6
		3783.35	2.70e+4
		4258.35	2.80e+3
		4119.53	6.40e+2
		4351.76	3.60e+5
		4549.46	3.02e+5
		4576.33	4.41e+4
		4595.68	1.82e+3
		4173.45	1.60e+5
		4332.88	1.03e+3
		4656.97	1.17e+4
		5316.78	1.01e+5
		5337.72	1.15e+4
		7462.38	2.10e+3
		7515.88	3.90e+3
		7449.34	5.00e+3
1.5	45044.21		
		2262.69	4.10e+6
		2268.56	2.19e+5
		2368.60	7.30e+7
		2384.39	2.60e+7
		2727.54	1.10e+8
		2749.18	1.20e+8
		2761.81	3.16e+7
		3210.45	3.30e+6
		3186.74	3.30e+6
		3166.67	1.90e+5
		3821.92	7.70e+3
		3746.56	1.50e+4
		4211.80	8.60e+2

			4075.95	6.90e+2
			4416.82	2.10e+5
			4303.17	2.70e+5
			4128.74	2.90e+4
			4522.62	3.24e+5
			4541.52	6.42e+4
			4601.36	2.17e+3
			5264.79	5.12e+4
			7308.07	1.80e+4
			7320.65	1.10e+4
			7310.19	7.30e+3
	0.5	45206.49		
			2254.41	4.97e+5
			2260.24	3.42e+6
			2375.19	1.00e+8
			2736.97	1.30e+8
			2749.48	1.21e+8
			3193.80	6.10e+6
			3170.34	9.60e+5
			3798.35	8.60e+3
			3723.91	2.40e+3
			4183.20	1.30e+3
			4385.37	4.10e+5
			4273.32	8.20e+4
			4508.28	4.22e+5
			7224.47	2.10e+4
			7222.39	1.90e+4
z ^{4}Po	2.5	46967.0		
			2562.53	2.39e+8
			2591.54	6.59e+7
			2611.07	8.55e+6
			2146.04	6.64e+5
			2159.16	8.46e+4
			2984.82	3.13e+7
			3002.65	1.15e+7
			3494.67	8.69e+4
			3779.58	9.14e+3
			3896.11	3.75e+3
			3824.92	9.13e+2
			3974.16	5.22e+3
			4138.40	1.56e+3
			4160.62	4.05e+2
			4227.16	2.01e+4
			4720.14	6.28e+2
			6456.38	1.46e+5
			6416.92	3.24e+4
			6407.25	3.57e+3
	1.5	47689.8		
			2563.47	1.88e+8
			2582.58	1.07e+8

			2593.73	1.84e+7
			2139.64	6.78e+5
			2153.90	2.21e+4
			2965.03	6.42e+6
			2985.55	1.74e+7
			3507.39	5.27e+4
			3443.82	5.47e+4
			3833.01	2.98e+3
			3720.17	3.72e+3
			3908.54	1.41e+3
			3764.09	1.74e+4
			4002.07	3.29e+3
			4088.75	1.12e+3
			4104.18	3.13e+2
			4153.00	1.24e+4
			4886.92	2.98e+2
			4627.86	8.73e+0
			6247.55	1.48e+5
			6238.39	6.79e+4
			6239.94	1.13e+4
	0.5	47626.1		
			2566.91	1.53e+8
			2577.92	1.62e+8
			2137.75	4.93e+5
			2964.62	7.06e+6
			3478.55	1.95e+4
			3416.01	3.13e+5
			3798.59	1.16e+4
			3964.56	5.09e+3
			3872.75	1.25e+4
			4064.75	4.52e+2
			4831.11	1.13e+3
			4577.78	2.70e+2
			6147.73	1.27e+5
			6149.23	1.14e+5
c ^{4}F	4.5	50157.45		
x ^{4}G	5.5	65580.0		
			2489.82	9.00e+7
			6482.21	1.74e+3

Fe III

Desig.	J	E(cm^{-1})	λ(Å)	A(sec^{-1})
a ^{5}D	4.	0.		
	3.	436.2		
			229253.	.0028
	2.	738.9		
			330360.	.0018
	1.	932.4		
			516796.	6.7e-4
	0.	1027.3		
			1054000.	1.4e-4
a ^{3}P	2.	19404.8		
			5272.	.40
			5413.	.038
	1.	20688.4		
			5086.	.091
			5013.	.53
	0.	21208.5		
			4932.	.67
a ^{3}H	6.	20051.1		
	5.	20300.8		
	4.	20481.9		
a ^{3}F	4.	21462.2		
			4659.	.44
			4756.	.081
	3.	21699.9		
			4703.	.27
			4771.	.087
			4608.	.038
	2.	21857.2		
			4735.	.10
			4779.	.049
			4668.	.026
a ^{3}G	5.	24558.8		
	4.	24940.9		
			4009.	.019
	3.	25142.4		
a ^{7}S	3.	30088.84		
a ^{1}I	6.	30356.2		
			9945.	.058
			9704.	.089
a ^{3}D	1.	30725.8		
			3367.	.13
			3356.	.15
			10507.	.023
			9963.	.085

			8833.	.019
	2.	30716.2		
			3336.	.11
			3358.	.095
			3303.	.027
			8841.	.066
	3.	30857.8		
			3241.	.23
			3320.	.044
			3287.	.047
			8731.	.063
a ^{1}G	4.	30886.4		
			9447.	.20
			10886.	.12
			10611.	.23
			9611.	.081
a ^{1}S	0.	34812.4		
			7080.	1.5
a ^{1}D	2.	35803.7		
			7170.	.12
			7090.	.22
			6616.	.033
			6098.	.096
a ^{5}S	2.	40999.9		
a ^{1}F	3.	42896.9		
			5632.	.05
			5569.	.098
			8210.	.034
			8306.	.061
b ^{3}P	0.	49148.		
	1.	49576.9		
	2.	50412.3		

Fe V

Desig.	J	E(cm^{-1})	λ(Å)	A(sec^{-1})
^5D	0.	0.		
	1.	142.1		
	2.	417.3		
	3.	803.1		
	4.	1282.8		
$^3P2$	0.	24055.4		
			4181.	1.3
	1.	24972.9		
			4071.	1.1
			4003.	.13
	2.	26468.3		
			3896.	.71
			3798.	.036
^3H	4.	24932.5		
			4227.	.0011
	5.	25225.9		
	6.	25528.5		
$^3F2$	2.	26760.7		
			3795.1	.20
			3851.	.047
			3756.	.10
	3.	26842.3		
			3840.	.40
			3912.	.066
			3784.	.16
	4.	26974.0		
			3891.	.74
			3820.	.16
^3G	3.	29817.1		
			3400.	.007
			3445.	.017
			3504.	.0026
	4.	30147.0		
			3407.	.0078
			3463.	.032
	5.	30430.1		
$^1G2$	4.	36586.3		

Fe VI

Desig.	J	E(cm^{-1})	λ(Å)	A(sec^{-1})
^4F	1.5	0.		
	2.5	512.		
	3.5	1188.		
	4.5	2001.		
^4P	0.5	18738.		
			5485.	.031
			5335.	.055
	1.5	18942.		
			5631.	.036
			5424.	.032
			5279.	.014
	2.5	19611.		
			5677.	.048
			5427.	.021
			5237.	.0053
^2G	3.5	20617.		
			5146.	.22
			5371.	.012
			4972.	.20
	4.5	21315.		
			5176.	.56
			4969.	.22
^2P	1.5	26215.		
			3996.	.0036
			3891.	.422
			3815.	.27
	0.5	26496.		
			3849.	.001
			3775.	.0025
$^2D2$	2.5	28425.		
			3664.	.95
			3576.	.12
			3512.	.045
	1.5	28628.		
			3646.	.0013
			3558.	.68
			3495.	.37
^2H	4.5	28725.		
			3630.	.0033
			3740.	.0056
	5.5	29203.		
^2F	3.5	46218.		
	2.5	46604.		

Co I

Desig.	J	E(cm^{-1})	λ(Å)	Log(gf)
a ^{4}F	4.5	0.		
	3.5	816.		
	2.5	1406.8		
	1.5	1809.3		
b ^{4}F	4.5	3482.8		
	3.5	4142.7		
	2.5	4690.2		
	1.5	5075.8		
a ^{2}F	3.5	7442.4		
	2.5	8460.8		
a ^{4}P	2.5	13795.5		
	1.5	14036.3		
	0.5	14399.3		
b ^{4}P	2.5	15184.0		
	1.5	15774.0		
	0.5	16195.7		
a ^{2}G	4.5	16467.9		
	3.5	17233.7		
a ^{2}D	1.5	16470.6		
	2.5	16778.2		
a ^{2}P	1.5	18389.6		
	0.5	18775.0		
b ^{2}P	1.5	20500.7		
	0.5	21215.9		
a ^{2}H	5.5	21780.5		
	4.5	22475.4		
b ^{2}D	2.5	21920.1		
	1.5	23152.6		
b ^{2}G	4.5	23184.2		
	3.5	23207.8		
z ^{6}F^o	5.5	23841.8		
			4234.00	-3.27
	4.5	23855.6		
			4190.71	-2.65
	3.5	24326.1		
			4252.31	-2.77
	2.5	24733.3		
			4285.79	-3.11
	1.5	25041.2		
	0.5	25232.8		
z ^{6}D^o	4.5	24627.8		
			4727.94	-3.15
	3.5	25269.3		
	2.5	25739.9		

	1.5	26063.1		
	0.5	26250.5		
z $^6G^?$	6.5	25138.9		
	5.5	25568.7		
			3909.93	-2.28
	4.5	25937.6		
			3979.52	-2.36
	3.5	26232.1		
			4027.04	-2.53
	2.5	26450.0		
			4057.20	-2.89
	1.5	26597.6		
c ^2D	2.5	27497.1		
	1.5	28470.5		
z $^4F^c$	4.5	28345.9		
			3526.85	-0.32
			3631.39	-1.98
			4020.90	-1.58
	3.5	28777.3		
			3474.02	-0.19
			3575.36	-0.65
			3652.54	-1.92
			3952.33	-2.42
			4058.19	-2.14
			7354.59	-2.01
	2.5	29216.4		
			3520.08	-1.52
			3594.87	-0.71
			3647.66	-2.00
			3987.12	-2.36
	1.5	29563.2		
			3550.60	-1.23
			3602.08	-0.75
			4019.30	-2.60
z $^4G^o$	5.5	28845.2		
			3465.80	-0.38
			3941.73	-1.68
	4.5	29269.7		
			3513.48	-0.44
			3876.84	-1.61
			3978.66	-1.88
	3.5	29735.2		
			3456.93	-1.93
			3529.03	-0.52
			3808.11	-2.18
			3906.29	-1.84
			3991.69	-2.12
	2.5	30103.0		
			3533.36	-0.63
			3933.91	-2.42

			3994.54	-2.25
z $^4D^o$	3.5	29294.5		
			3412.63	-0.70
			3974.73	-2.05
			3510.43	-0.86
			3873.12	-0.31
			6450.24	-1.32
			7084.99	-0.86
			7987.38	-1.44
	2.5	29948.8		
			3431.58	-0.56
			3502.62	-1.18
			3873.96	-0.53
			3957.94	-1.62
			6189.00	-1.85
			6282.63	-1.67
			6771.06	-1.58
			7052.89	-1.13
			7417.38	-1.50
			7590.57	-2.13
	1.5	30443.6		
			3442.93	-0.70
			3491.32	-1.20
			3881.87	-1.01
			3940.89	-1.68
			6093.13	-1.81
			6230.97	-2.02
			6551.44	-2.26
			6814.94	-1.41
			7016.61	-1.47
			7154.71	-1.75
	0.5	30742.7		
			3455.23	-0.84
			3894.98	-1.12
			5984.08	-2.04
			6116.98	-1.91
			6678.81	-2.02
			6872.40	-1.36
z $^2G^o$	4.5	31699.7		
			3627.81	-0.74
			4121.32	-0.03
			6563.42	-1.45
	3.5	32733.1		
			3496.68	-0.92
			3564.95	-0.63
			3952.92	-1.03
			4118.77	-0.10
z $^2F^o$	3.5	31871.2		
			3219.15	-1.83
			3521.57	-0.26

			3605.36	-0.76
			4092.39	-0.74
			5530.77	-1.60
			6490.34	-1.85
	2.5	32781.7		
			3558.78	-1.59
			3945.33	-1.28
			4110.54	-0.80
			6429.91	-1.82
y $^4D^o$	3.5	32027.5		
			3121.42	-1.40
			3502.28	0.30
			3585.16	-0.64
			3656.97	-1.95
			4066.37	-1.11
			5483.34	-1.20
			5935.39	-1.95
	2.5	32654.5		
			3139.94	-1.32
			3506.32	0.24
			3574.96	-0.38
			3624.96	-1.76
			5301.06	-1.39
			5369.58	-1.25
	1.5	33150.7		
			3512.64	0.14
			3560.89	-0.48
			5230.22	-1.04
			5331.47	-1.40
	0.5	33449.2		
			3523.43	0.0-
			5247.93	-1.00
y $^4G^o$	5.5	32430.6		
			3082.62	-1.07
			3453.50	0.66
	4.5	32464.7		
			3529.81	0.24
			3995.31	0.16
			3158.78	-1.22
			3449.44	-0.33
			6243.51	-1.67
	3.5	33173.4		
			3013.60	-1.31
			3089.60	-1.27
			3147.06	-1.07
			3367.11	-0.84
			3443.64	0.38
			3509.84	-0.08
			3885.29	-1.81
			4045.39	-0.95

	2.5	33674.4		
			3042.48	-1.42
			3098.20	-1.29
			3137.33	-1.08
			3385.22	-0.55
			3449.17	0.11
			3495.69	-0.11
y $^4F^o$	4.5	32842.0		
			3044.00	-0.36
			3121.57	-1.75
			3405.12	0.43
			3483.41	-1.61
			3935.97	-0.42
	3.5	33466.9		
			2987.16	-0.96
			3061.82	-0.53
			3334.14	-0.73
			3409.18	0.11
			3841.46	-1.79
			3922.75	-1.56
			3997.91	-0.51
	2.5	33945.9		
			3017.55	-0.88
			3072.34	-0.74
			3354.38	-0.72
			3417.16	-0.05
			3462.80	0.24
	1.5	34196.2		
			3048.89	-1.05
			3086.78	-0.76
			3388.17	-0.41
			3433.04	0.20
			3884.62	-1.38
y $^2G^o$	4.5	33439.7		
			2989.59	-0.96
			3064.37	-1.94
			3412.34	0.28
			3845.47	0.29
			5890.48	-1.49
			8574.57	-1.54
	3.5	34133.6		
			2928.81	-2.25
			3000.55	-1.65
			3395.38	-0.12
			3745.50	-1.06
			3894.08	0.45
			5659.11	-2.00
			5915.54	-1.39
			8575.35	-1.06
z $^2D^o$	2.5	33462.8		

			3062.20	-2.08
			3842.05	-0.41
			5469.30	-1.82
			5991.88	-1.31
			6632.44	-1.22
			7712.68	-1.02
			8661.09	-1.52
	1.5	34352.4		
			3034.43	-1.91
			3370.33	-1.40
			3414.74	-0.72
			3861.16	-0.62
			5381.10	-1.79
			5590.73	-1.33
			6417.82	-1.41
			7610.24	-1.28
y $^2F^o$	3.5	35450.6		
			2886.44	-1.31
			3569.38	0.70
			3704.06	-0.43
			5266.49	-0.83
			7388.70	-1.01
	2.5	36329.9		
			2862.61	-1.62
			3587.19	0.70
			5235.21	-0.73
			6937.61	-1.37
			7586.72	-1.25
y $^2D^o$	2.5	36092.4		
			3489.40	0.49
			5176.08	-1.08
			5647.22	-1.06
			7054.04	-0.99
	1.5	36875.1		
			3518.35	0.60
			4899.52	-1.37
			5523.29	-1.15
			7285.28	-1.09
x $^4D^o$	3.5	39649.2		
			2574.35	-0.25
			2614.13	-1.33
			2764.19	-0.86
			2815.56	-0.93
			4086.31	-0.27
			4371.13	-1.26
	2.5	40346.0		
			2567.35	-0.09
			2594.16	-1.25
			2803.77	-1.05
			4068.54	-0.49

		4187.25	-1.15
1.5	40827.8		
		2562.15	-0.11
		2796.23	-1.40
		3898.49	-1.18
0.5	41101.8		
		2544.25	0.17
		4013.94	-.72

Co II

Desig.	J	E(cm^{-1})	λ(Å)	A(sec^{-1})
a ^3F	4.	0.		
	3.	950.3		
	2.	1597.2		
a ^5F	5.	3350.5		
	4.	4028.9		
	3.	4560.8		
	2.	4950.0		
	1.	5204.5		
b ^3F	4.	9812.7		
			10191.	.084
	3.	10708.1		
			9303.	.039
			10248.	.066
	2.	11321.5		
			9642.	.05
			10284.	.087
^1D	2.	11400.		
			9570.	.190
			10201.	.086
a ^3P	2.	13261.5		
			7541.	.192
			8123.	.041
	1.	13404.6		
			8029.	.149
			8469.	.063
	0.	13593.5		
			8336.	.20
a ^5P	3.	17771.5		
	2.	18031.5		
			5546.	.01
	1.	18338.5		
^1G	4.	18963.		
			5273.	.122
			5552.	.068
^3G	5.	21444.		
			4663.	1.236
			4880.	.037
			5527.	.682
			5742.	.133
			8597.	.061
	4.	21829.		
			4581.	.192
			4790.	.996
			4943.	.045

			5412.	.04
			5618.	.385
			5791.	.165
			8322.	.084
	3.	22245.		
			4495.	.011
			4696.	.265
			4843.	.987
			5490.	.025
			5655.	.155
			5782.	.117
			8668.	.065
			9155.	.039
b ^3P	2.	24074.6		
			4154.	6.443
			4324.	.532
			4449.	.01
			5125.	.154
			5229.	.019
			5299.	.018
			7841.	.028
	1.	24267.8		
			4289.	.217
			4411.	.673
			7771.	.06
			9085.	.037
			5177.	.08
			5246.	.046
			7724.	.01
	0.	24411.5		
			4383.	.531
			7686.	.01
			8968.	.066
c ^3P	2.	24886.5		
			4018.	1.394
			4178.	.65
			4294.	.151
			7415.	.023
			8602.	.031
			8709.	.034
			8855.	.012
			4920.	.034
			7053.	.019
			7372.	.035
	1.	25489.		
			4075.	7.198
			4186.	1.547
			4869.	.093
			4930.	.062
			7058.	.012

	0.	26055.		
			4089.	10.05
			7816.	.021
^1G	4.	24967.		
			4005.	.035
			4279.	.282
			7371.	.068
			6599.	.318
			7013.	.182
a ^3D	3.	27484.3		
			3638.	3.27
			3769.	.974
			3863.	.097
			4263.	1.058
			4362.	.023
			4438.	.051
			5659.	.213
			5961.	.119
			6187.	.016
			10296.	.092
	2.	28111.9		
			3557.	.042
			3682.	2.964
			3771.	1.358
			5984.	.023
			6734.	.012
			4246.	1.275
			4317.	.108
			4365.	.115
			5746.	.039
			5956.	.041
			9920.	.097
			10232.	.028
	1.	27585.3		
			3754.	.534
			3848.	2.25
			6178.	.141
			6981.	.01
			7052.	.026
			4418.	.903
			4468.	.407
			6149.	.072
^3H	6.	27274.		
			3667.	4.114
	5.	27631.		
			3619.	.193
			3748.	3.749
	4.	28064.		
			3563.	.011
			3688.	.274

			3778.	3.368
			6001.	.024
			5479.	.03
			5761.	.015
^1P	1.	29357.		
			3520.	.034
			3602.	1.988
			5569.	1.02
			6213.	.108
			4097.	.309
			4140.	.142
			5545.	.047
^1H	5.	30794.		
			3351.	.098
			8452.	.062
^1D	2.	30904.		
			3236.	.012
			3338.	.048
			3412.	.085
			5127.	1.629
			5668.	.045
			8375.	.012
			3796.	.025
			4951.	1.023
			5107.	.564
a ^5D	4.	40694.9		
	3.	41313.9		
	2.	41737.8		
	1.	42008.6		
	0.	42252.		
^3F	2.	40601.		
			2463.	.149
			2522.	2.776
			2564.	5.588
			3425.	.012
			3658.	.258
			3677.	1.447
			3703.	1.252
	3.	40744.		
			2454.	2.227
			2513.	4.517
			2554.	1.977
			3408.	.153
			3639.	1.143
			3658.	1.876
			4591.	.013
	4.	40933.		
			2433.	7.186
			2501.	1.705
			2542.	.082

3386.	.157
3614.	3.244

Co III

Desig.	J	E(cm^{-1})	λ(Å)	A(sec^{-1})
a ^4F	4.5	0.		
	3.5	841.		
	2.5	1451.		
	1.5	1867.		
a ^4P	2.5	15202.		
			6963.	.027
			6578.	.011
	1.5	15428.		
			7374.	.011
			7155.	.039
			6855.	.066
	D.5	15811.		
			7171.	.063
			6964.	.048
a ^2G	4.5	16978.		
			6197.	.15
			5890.	.47
	3.5	17766.		
			6129.	.14
			5908.	.18
			5629.	.015
^2P	1.5	20461.		
			5382.	.016
			5268.	.019
	0.5	21242.		
a ^2H	5.5	22720.		
	4.5	23434.		
a ^2D	2.5	22684.		
			4716.	.011
			4587.	.10
	1.5	23869.		
			4548.	.057
			4466.	.11